Biological and dust aerosol as sources of ice nucleating particles in the Eastern Mediterranean: source apportionment, atmospheric processing and parameterization

Kunfeng Gao[1], Franziska Vogel[2,a], Romanos Foskinis[1,3,4,5], Stergios Vratolis[4], Maria I. Gini[4], Konstantinos Granakis[4], Anne-Claire Billault-Roux[6], Paraskevi Georgakaki[1], Olga Zografou[4], Prodromos Fetfatzis[4], Alexis Berne[6], Alexandros Papayannis[1,3], Konstantinos Eleftheridadis[4], Ottmar Möhler[2], Athanasios Nenes[1,5]

[1]Laboratory of Atmospheric Processes and Their Impacts, School of Architecture, Civil and Environmental Engineering, École Polytechnique Fédérale de Lausanne, Lausanne, Switzerland
[2]Institute of Meteorology and Climate Research, Karlsruhe Institute of Technology, Karlsruhe, Germany
[3]Laser Remote Sensing Unit (LRSU), Physics Department, National Technical University of Athens, Zografou, Greece
[4]ENvironmental Radioactivity & Aerosol Technology for atmospheric & Climate ImpacT Lab, INRASTES, NCSR Demokritos, 15310 Ag. Paraskevi, Attica, Greece
[5]Centre for Studies of Air Quality and Climate Change, Institute of Chemical Engineering Sciences, Foundation for Research and Technology Hellas, Patras, Greece
[6]Environmental Remote Sensing Laboratory (LTE), School of Architecture, Civil & Environmental Engineering, Ecole Polytechnique Fédérale de Lausanne, Lausanne, Switzerland
[a]Now at: Institute of Atmospheric Sciences and Climate (ISAC), National Research Council (CNR), Bologna, Italy

Correspondence to: Athanasios Nenes (athanasios.nenes@epfl.ch) and Kunfeng Gao (kunfeng.gao@epfl.ch)

Abstract. Aerosol-cloud interactions in mixed-phase clouds (MPCs) are one of the most uncertain drivers of the hydrological cycle and climate change. A synergy of in-situ, remote sensing and modelling experiments was used to determine the source of ice nucleating particles (INPs) for MPCs at Mount Helmos in the Eastern Mediterranean. The influences of boundary layer turbulence, vertical aerosol distributions and meteorological conditions were also examined. When the observation site is in the free troposphere (FT), approximately 1 in 10^6 aerosol particles serve as INPs around $-25°C$. The INP abundance spans three orders of magnitude and increases following the order of marine aerosols, continental aerosols, and finally, dust plumes. Biological particles are important INPs observed in continental and marine aerosols, whereas they play a secondary yet important role even during Saharan dust events. Air masses in the planetary boundary layer (PBL) show both enriched INP concentrations and higher proportion of INPs in comparison to total aerosol particles, different from cases in the FT. The presence of precipitations/clouds enriches INPs in the FT but decreases INPs in the PBL. Additionally, new INP parameterizations, incorporating the ratio of fluorescent-to-nonfluorescent or coarse-to-fine particles and predicting >90% of the observed INPs within an uncertainty range of a factor of 10, exhibit better performance than current widely-used parameterizations, and allow ice formation in models to respond to variations in dust and biological particles. The improved parameterizations can help MPC formation simulations in regions with various INP sources or different regions with prevailing INP sources.

1 Introduction

Clouds in the atmosphere can be either composed solely of liquid water droplets, ice crystals, or a mixture of the both (mixed-phase clouds; MPCs). Cloud phase regulates the optical properties and microphysical characteristics of the clouds, which further influences their impacts on the hydrological cycle and the climate (Tan et al., 2016; Lohmann and Neubauer, 2018; Zhou et al., 2022). Notably, the modulation of cloud properties from anthropogenic particles is one of the leading sources of uncertainty in anthropogenic climate change (e.g., Seinfeld et al. (2016)). MPCs are ubiquitous (D'alessandro et al., 2019) but have a much more uncertain impact on the climate compared to single-phase clouds (Bjordal et al., 2020). This uncertainty stems from the large number of interactions that can take place between liquid droplets, ice crystals, and water vapor – each of which can cool or warm the climate. Furthermore, MPCs exhibit considerable dynamic variability over time and location because they are thermodynamically unstable. Under supercooled conditions, the saturation vapor pressure with respect to ice (S_i) is higher than that with respect to water (S_w), which favours the mass transfer – through deposition from the vapor phase – of liquid water from particles onto ice existing in MPCs, i.e., the growth of the latter at the expense of the former. This process is known as the Wegener-Bergeron-Findeisen (WBF) process (Wegener, 1912; Bergeron, 1935; Findeisen, 1938; Findeisen et al., 2015). The amount of ice crystals in MPCs is also regulated by the abundance of aerosol particles capable of initiating ice formation, i.e., ice nucleating particles (INPs). INPs can trigger primary ice formation in the MPC regime (Kanji et al., 2017; Burrows et al., 2022; Knopf and Alpert, 2023) with the absence of spontaneous ice formation via the homogeneous freezing of solution droplets which otherwise requires temperatures (T) lower than the homogeneous nucleation temperature (Barahona and Nenes, 2009; Lohmann et al., 2016). Thus, the heterogeneous ice nucleation of INPs can lead to MPC glaciation. An added complexity is ice multiplication processes (or secondary ice processes, SIP) occurring in warmer MPCs, which can multiply ice crystal numbers by orders of magnitude above the primary ice levels generated from INPs (Field et al., 2017; Sullivan et al., 2018; Georgakaki et al., 2022; Pasquier et al., 2022). Constraining therefore the abundance and origin of INPs is critical for understanding MPCs formation and their effects on the hydrological cycle and climate.

MPCs persistently exist in mountainous terrain where local and remote air masses may be present (Pousse-Nottelmann et al., 2015; Lohmann et al., 2016; Henneberg et al., 2017). Different air masses, e.g., continental pollution, dust plumes, and sea spray aerosols from remote marine areas, may contain distinct INP populations with characteristic abundance and ice formation ability (Demott et al., 2010; Tobo et al., 2013; Mccluskey et al., 2018; Brunner et al., 2021). The INP type, which depends on its air mass source, is crucial for determining MPC formations. Different types of INPs nucleate ice in different T regimes. Biological particles as effective INPs are active for T warmer than −15°C whereas dust particles generally form ice for T lower than −15°C (Murray et al., 2012). In addition, the formation and evolution of MPCs over orographic terrains are influenced by the planetary boundary layer height (PBLH) (Miltenberger et al., 2020), which regulates the aerosol sources depending on whether the observation site is inside or outside the planetary boundary layer (PBL) (Conen et al., 2015; Wieder et al., 2022). In-situ observations at high altitudes in mountainous terrains provide the possibility to specifically investigate INP populations

relevant for MPCs under different atmospheric conditions, given that the relative position of mountain top in the atmosphere can vary with changing PBLH (Foskinis et al., 2024, under review).

70 We study the source of INPs and the characteristics of different INP sources relevant for orographic MPCs in the Eastern Mediterranean region. A field campaign, the Cloud-AerosoL InteractionS in the Helmos background TropOsphere (CALISHTO), was conducted at the Helmos Hellenic Atmospheric Aerosol and Climate Change (in short as (HAC)^2 hereafter) station (37.9843° N, 22.1963° E, 2314 m above sea level (a.s.l.)) close to the summit of Mt. Helmos. It is reported that (HAC)^2 is a station among 12 in Europe with the lowest impacts from the PBL (Collaud Coen et al., 2018), suggesting that (HAC)^2 is

75 an appropriate station to study INPs from remote sources and to evaluate the characteristics of INPs under background conditions, e.g., in the free troposphere (FT).

This study presents the observations of INPs and aerosol properties at (HAC)^2 during CALISHTO campaign from a period between October 12 and November 27 in 2021. The objectives of this study are twofold: (i) to identify different INP sources at Mt. Helmos and evaluate the characteristics of these INP sources. To this end, a synergy of in-situ aerosol property

80 measurements, remote sensing measurements and model simulations of air mass trajectories, was used to identify different INP sources. In addition, the influence of precipitation and/or clouds on the INP characteristics was also investigated, considering that precipitations or clouds may serve as sinks or sources of aerosol particles (Isokäänta et al., 2022; Khadir et al., 2023), which therefore influence the INP abundance of the source. (ii) to use the data and analysis carried out to evaluate existing INP parameterizations and propose new ones that capture the INP number concentration (N_{INP}) better for the wide

85 diversity of particle types encountered at Mt. Helmos during CALISHTO. Compared to different parameterizations reported in the literature (Demott et al., 2010; Niemand et al., 2012; Tobo et al., 2013; Demott et al., 2015; Ullrich et al., 2017; Mccluskey et al., 2018), the improvement of new INP parameterizations is based on the advantage of the inclusion of source characteristics, i.e., the partitioning of fluorescent and non-fluorescent (or coarse and fine) particles, yielding important implications for modelling studies aimed at quantifying climate effects of cloud-aerosol interactions in MPCs.

90 **2 Methods**

2.1 Overview of field campaign

(HAC)^2 is an atmospheric monitoring station, contributing data to GAW and ACTRIS since 2016 (Laj et al., 2020), located near the summit of Mt. Helmos at the heart of the Peloponnese in Greece. (HAC)^2 is frequently situated in the FT or at the FT/PBL interface (Foskinis et al., 2024, under review) while it is also frequently covered by clouds in the Fall and springtime,

95 which allows for the in-situ study of aerosol-cloud interactions for warm and MPC clouds. (HAC)^2 is also located at a cross-road of different air masses, including continental pollution, Saharan dust events, long-range transported biomass burning, marine sea spray aerosols, etc, which allows one to explore the effects of different aerosol types on cloud formation, and which are explored here. The experimental setup of the CALISHTO observations is presented in Figure 1, including in-situ ice nucleation (IN) experiments, aerosol properties (size distribution, chemical composition, fluorescent and optical properties) at

3

100 (HAC)^2, remote sensing measurements conducted at Vathia Lakka (VL) a site 500 m lower than (HAC)^2, and back trajectory analysis for calculating the origin of air masses sampled at (HAC)^2. Also, meteorological standard parameters recorded at (HAC)^2 were used to correct the measured INP and aerosol particle number concentrations to values under the equivalent atmospheric standard condition (i.e., per standard volume of sampled air, std).
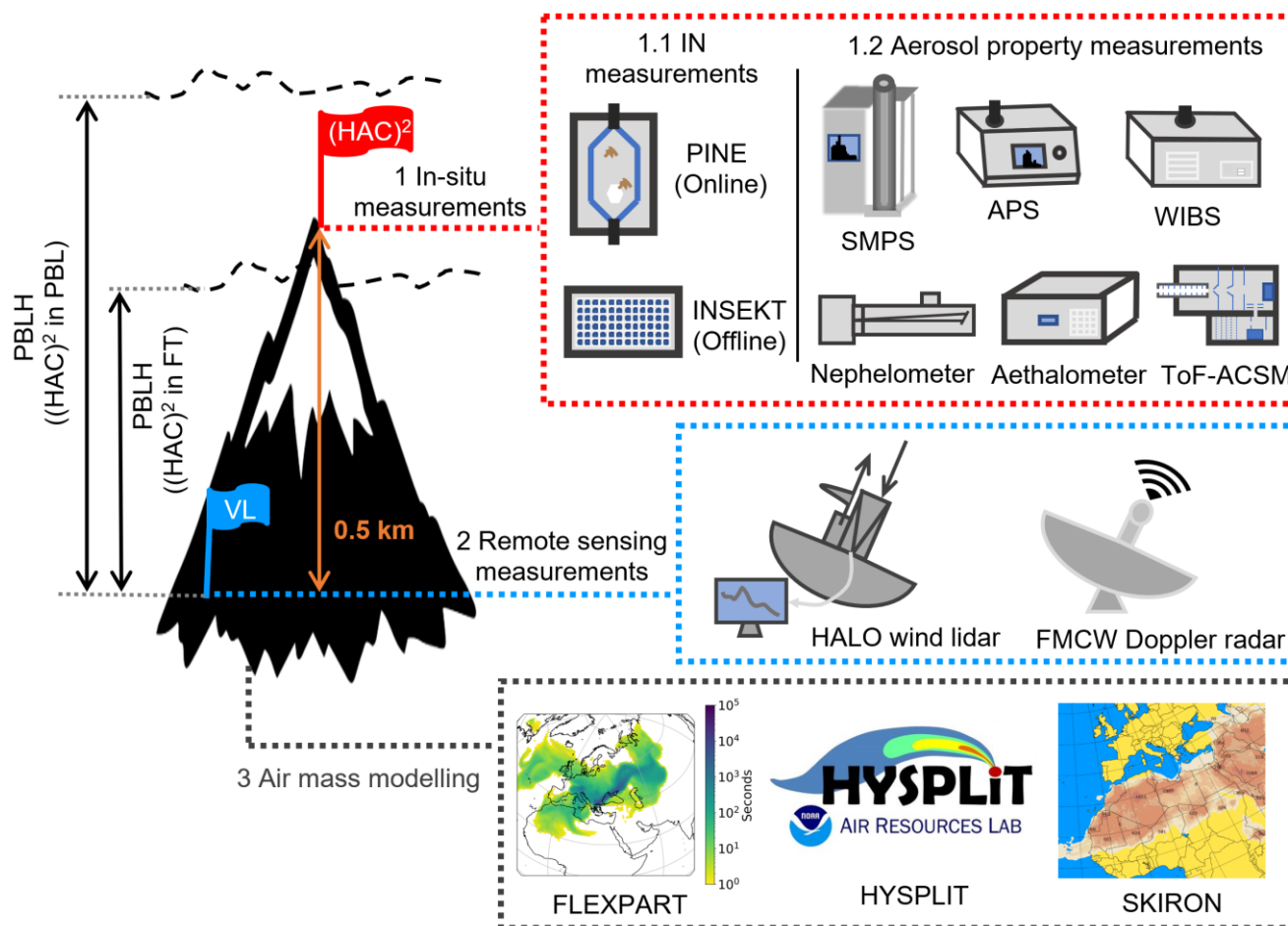
Figure 1. Overview of the instrumentation setup for CALISHTO campaign. 1: (HAC)^2 stands for the mountaintop station where in-situ measurements were performed, including ice nucleation measurements and aerosol property measurements: Portable Ice Nucleation Experiment (PINE), Scanning Mobility Particle Sizer (SMPS), Aerodynamic Particle Sizer (APS), Wideband Integrated Bioaerosol Sensor (WIBS), nephelometer and aethalometer, as well as Time-of-Flight Aerosol Chemical Speciation Monitor (ToF-ACSM). Filters collected for off-line analysis by using Ice Nucleation Spectrometer of the Karlsruhe Institute of Technology (INSEKT). 2: VL represents the Vathia Lakka site at the base of Mt. Helmos, at an altitude of ~1.8 km, at which a HALO wind lidar and a frequency-modulated continuous wave (FMCW) Doppler radar (working at 94 GHz) were placed for remote sensing of wind fields, aerosols and clouds. 3: Modelling products include FLEXible PARTicle dispersion model (FLEXPART) to determine the source regions of aerosol particles reaching the site, Hybrid Single-Particle Lagrangian Integrated Trajectory (HYSPLIT) to acquire airmass atmospheric trajectories, and the SKIRON model to obtain dust forecasts. PBL is the planetary boundary layer and FT is the free troposphere. PBLH stands for PBL height relative to the VL.

2.2 INP observations

2.2.1 Offline INP observation

The Ice Nucleation Spectrometer of the Karlsruhe Institute of Technology (INSEKT) freezing assay (Schiebel, 2017; Schneider et al., 2021) was used to measure the immersion mode INPs from 0 to −25 °C (**Error! Reference source not found.**). INSEKT measures the freezing T of small water volumes (50 μL) that contain aerosol suspended in them. To prepare the freezing aliquots, aerosol particles were first sampled onto filters (0.2 μm Whatman Nuclepore track-etched polycarbonate membranes, 47 mm, with a flowrate of 9 liter per minute) from an omnidirectional total inlet at (HAC)[2] and then extracted in nano-pure water which was beforehand filtered through a 0.1 μm Whatman syringe filter. The aerosol suspension was diluted by 15:1 and 225:1 using two different ratios before pipetting into two 96-well polymerase chain reaction (PCR) plates. In addition to the original solution and the dilutions, some of the wells (~32) are filled with nano pure water for freezing background tests. The PCR plates were then placed in an aluminium block cooled by an ethanol chiller to perform freezing experiments and the frozen fraction of the prepared aliquots was recorded as a function of T. Following the analysis protocol reported in Vali (1971) and Vali (2019), the INP concentration of aerosol samples (in L^{-1}) as a function of T can be calculated using the tested frozen fraction, sampled aerosol volume, suspended liquid volume and the dilution ratio. The sampling time of each filter sample was approximately 24 hours and a few filter samples had a longer sampling time; detailed information for each INSEKT filter will be provided in the overview paper for CALISHTO campaign.

2.2.2 Online INP observations

A portable ice nucleation experiment (PINE) (Möhler et al., 2021) chamber was used for automated real-time observations of INPs at (HAC)[2] (**Error! Reference source not found.**). PINE is designed on the basis of expansion cooling of air parcels (Mohler et al., 2003), where ambient air (10 L) is sampled into a pre-cooled cloud chamber after passing through Nafion dryers to remove excess moisture and avoid chamber frosting. The air is then expanded and cools down until supersaturation is reached, causing the aerosol particles in the sample to form supercooled droplets and/or ice crystals. Both the number concentration and phase of aerosol particles are monitored, so INPs that activate to ice crystals can be differentiated from droplets and counted. PINE can be operated in repeated cycles by refilling the cloud chamber with fresh aerosol at the end of an expansion. In this study, PINE was operated in a T range from −23 to −28 °C and S_w (saturation with respect to water) >1.0 to measure INPs activating as ice in all freezing mechanisms. A single PINE expansion cycle has a time resolution of 6 min and the INP number concentration detection limit for a single experiment is approximately 0.5 L^{-1}; averaging over an hour of samples reduces the detection limit to approximately 0.05 L^{-1} (Möhler et al., 2021). The same sampling inlet was used for both PINE and INSEKT.

2.3 Aerosol property measurements

2.3.1 In-situ aerosol property monitoring

Ambient air was sampled through a total inlet for in-situ aerosol property measurements at (HAC)^2 (**Error! Reference source not found.**). A downstream inlet with an impaction stage supplies PM10 aerosol to a scanning mobility particle sizer (SMPS; Vienna-type differential mobility analyser (DMA), and condensation particle counter (CPC) 3772, TSI Inc., US) and an aerodynamic particle sizer (APS; model 3321, TSI Inc., US) to measure the aerosol particle size distribution range from 10 to 800 nm (electrical mobility diameter) and 0.5 to 20 μm (aerodynamic diameter), respectively. The number concentration of aerosol particles larger than 95 nm (SMPS $N_{>95nm}$) was calculated from the SMPS data and used with a threshold value (100 std cm^{-3}) to determine if (HAC)^2 is inside or outside the PBL (Herrmann et al., 2015; Brunner et al., 2021), given that large-sized aerosol particles are much rarer outside the PBL. This threshold is confirmed by other methods determining the PBLH using the wind lidar and other data (Foskinis et al., 2024, under review). The number concentrations of total, coarse (>1.0 μm, aerodynamic diameter) and fine (<1.0 μm) particles were also calculated based on APS data, termed Total$_{APS}$, Coarse$_{APS}$ and Fine$_{APS}$, respectively. In addition, the combined aerosol particle distribution observed by both SMPS and APS was calculated by using the method reported in Khlystov et al. (2004). Accordingly, the number concentrations of total particles (Total$_{SMPS+APS}$) and total fine particles (Fine$_{SMPS+APS}$ <1.0 μm, aerodynamic diameter) observed by both SMPS and APS were also calculated.

A wideband integrated bioaerosol sensor-New Electronics Option (WIBS-5/NEO, Droplet Measurement Technologies, LLC. US) was used at (HAC)^2, sampling aerosols with a PM10 impactor, to measure the size distribution of aerosol particles with optical sizes larger than 0.5 μm. WIBS also measures the fluorescence of aerosols on a single particle basis using ultraviolet light to trigger the excitation of the particle and then detecting the fluorescence at three fluorescent channels: FL1 (excitation wavelength at 280 nm and emission detection at the waveband 310–400 nm), FL2 and FL3 (emission detection waveband of 420–650 nm probing particles excited at 280 and 370 nm respectively). These three channels target at different biologic fluorophores: tryptophan-containing proteins, NAD(P)H co-enzymes and riboflavin, respectively (Kaye et al., 2005; Savage et al., 2017), which are ubiquitous in microbes (Pöhlker et al., 2012). Particles showing fluorescence exclusively in any one of three channels are attributed to a type of A$_{WIBS}$ (FL1 only), B$_{WIBS}$ (FL2 only) or C$_{WIBS}$ (FL3 only), respectively. Particles carrying two types of fluorophores and simultaneously detected by two channels are termed AB$_{WIBS}$ (FL1 and FL2), AC$_{WIBS}$ (FL1 and FL3) or BC$_{WIBS}$ (FL2 and FL3). Particles showing fluorescence in any one of the three channels are termed Fluo$_{WIBS}$. Particles detected in all three channels are attributed to a type of ABC$_{WIBS}$, which are much more likely to be of biological origin compared to the other types (Hernandez et al., 2016; Savage et al., 2017). Note that non-biological particles may also present in B$_{WIBS}$, C$_{WIBS}$ and BC$_{WIBS}$ channels, behaving as interfering particles such as some black carbon and dust particles associated with fluorescent materials (Toprak and Schnaiter, 2013; Savage et al., 2017). The fluorescence detection limit was determined by subtracting the mean background signal plus 9× standard deviations measured from routinely forced trigger tests. The WIBS data can be resampled to a customized time span because of its 15 μs high time resolution for single particle

detection. The measurement rates of WIBS-5/NEO are up to 9500 cm^{-3} for all particles irrespective of fluorescence and up to 466 cm^{-3} for fluorescent particles.

180   The hourly mean light-scattering coefficient of dry PM10 aerosols at (HAC)^2 was measured by using an integrating nephelometer (Model 3563, TSI Inc., US) at 3 wavelengths (450, 550 and 700 nm, termed Scatt$_{450\ nm}$, Scatt$_{550\ nm}$ and Scatt$_{700\ nm}$) (Laj et al., 2020). Using light scattering coefficients measured at 450 and 700 nm wavelength, the Ångström exponent (α) can be calculated following Eq. (1):

$$\alpha = -\frac{\ln\left[Scatt_{700\ nm}/Scatt_{450\ nm}\right]}{\ln\left(700/450\right)}. \qquad (1)$$

185   The wavelength pair of 450 and 700 nm was used because the larger difference in the measured scattering coefficients gives more accurate α values (Mordas et al., 2015). A lower α value suggests the dominance of coarse particles in the sampled aerosols whereas a larger α value indicates the dominance of fine particles (Pereira et al., 2008), which helps to differentiate continental aerosols mainly containing fine particles from dust plumes dominated by coarse particles. In addition, the mass concentration of refractory and carbonaceous aerosol particles, i.e., elemental black carbon (eBC), sampled through a PM10

190 cut-off inlet was monitored by an aethalometer (AE31, Magee Scientific, US) at 880 nm with a minimum time base of 2 min. The chemical composition of non-refractory species of submicron ambient aerosols, including organics (Org), sulphate (SO$_4^{2+}$), nitrate (NO$_3^-$), ammonium (NH$_4^+$) and chloride (Cl$^-$), was monitored by a time-of-flight aerosol chemical speciation monitor (ToF-ACSM, Aerodyne Research Inc., USA) with a time resolution of 10 min.

2.3.2 Airmass remote sensing measurements

195   **Error! Reference source not found.** shows that remote sensing measurements were performed at VL at an altitude lower than (HAC)^2 by 500 m to measure the PBLH, radar equivalent reflectivity factor (Ze) and mean Doppler velocity (MDV). The PBLH was calculated by using the Doppler velocity of aerosols measured by a pulsed Doppler scanning lidar system (StreamLine Wind Pro model, HALO Photonics, UK). The lidar was operated in the stare vertical azimuth display mode at a wavelength of 1.5 μm with time resolution of 10 min and a vertical spatial resolution of 30 m. The vertical wind speed

200 distribution at a certain distance from the lidar was calculated (Barlow et al., 2011; Schween et al., 2014). The PBL top boundary is defined at a position where the standard deviation of the wind vertical velocity, σ_w, drops below 0.1 m^2 s^{-2} (Foskinis et al., 2024, under review). The vertical distance between VL and the PBL top boundary then is the PBLH. Note that PBLH may be unavailable during cloudy periods because the lidar signal is quickly attenuated in clouds and when too few particles are present because insufficient backscattering signal will inhibit PBLH determination. When PBLH results are unavailable,

205 SMPS $N_{>95nm}$ results were compared to the threshold value (100 std cm^{-3}) to define the (HAC)^2 position with respect to PBL (Herrmann et al., 2015; Brunner et al., 2021). In addition, a frequency-modulated continuous wave (FMCW) Wide-band Doppler spectral zenith profiler (WProf) was deployed to measure the radar reflectivity at a wavelength of 3.2 mm (corresponding to 94 GHz) up to 10 km above the ground level (a.g.l., Küchler et al., 2017; Billault-Roux et al., 2023; Ferrone

and Berne, 2023). The Doppler radar results at $(HAC)^2$ level (500 m above VL) were used to evaluate the presence of precipitation and clouds.

2.3.3 Airmass modelling

As shown in **Error! Reference source not found.**, the footprint and trajectory of airmasses arriving at $(HAC)^2$ were calculated by the FLEXible PARTicle dispersion Model (FLEXPART) (Stohl et al., 2005; Pisso et al., 2019; Vratolis et al., 2023) and the Hybrid Single-Particle Lagrangian Integrated Trajectory (HYSPLIT) (Draxler and Hess, 1998; Stein et al., 2015) models. FLEXPART was used to calculate the residence time of aerosol particles with a geometric mean diameter of 400 nm (10 nm − 10 μm, Fig. S1) and a standard deviation of 3.3 in defined locations in the past 10 days. The spatial resolution of the model corresponds to a grid cell size of 1°×1°. Note that more than 90% of the aerosol particles used in FLEXPART simulations have diameters larger than 100 nm and particles of this size range (> 100 nm) are mainly responsible for the observed INPs. The 24-hour aerosol footprint simulation for each calendar day was run every 3 hours (from 00:00 to 24:00 LTC) by releasing 40000 air parcels from $(HAC)^2$. Local wind and turbulence, as well as mesoscale wind fluctuations were considered in the dispersion and transport calculations. Dry and wet aerosol deposition processes were also included in the model. The residence time of aerosol particles in each location was integrated from a height of 0 to 500 m a.g.l.

The HYSPLIT was run to calculate the 7-day backward trajectories of air masses arriving at $(HAC)^2$. Input meteorological data from the Global Data Assimilation System (GDAS, 1°×1° resolution) (Stein et al., 2015; Kostrykin et al., 2021) were used for the backward trajectory calculations. The source height was set at three height levels of 100, 1000 and 2000 m a.g.l. The model was launched every 6 h backward the start time. The start time of back trajectories on a day was decided depending on the need to differentiate whether there is an aerosol source change during the day.

Finally, the SKIRON model (Kallos et al., 2006; Spyrou et al., 2010) was used to calculate the time series of dust mass concentration at $(HAC)^2$ at different height levels of 1250, 1614, 1881 and 2170 m a.s.l. Together with $Coarse_{APS}$ particle concentration and the aerosol footprints from FLEXPART, dust mass concentrations below $(HAC)^2$ predicted by SKIRON help to determine the occurrence and intensity of dust plumes and their source region.
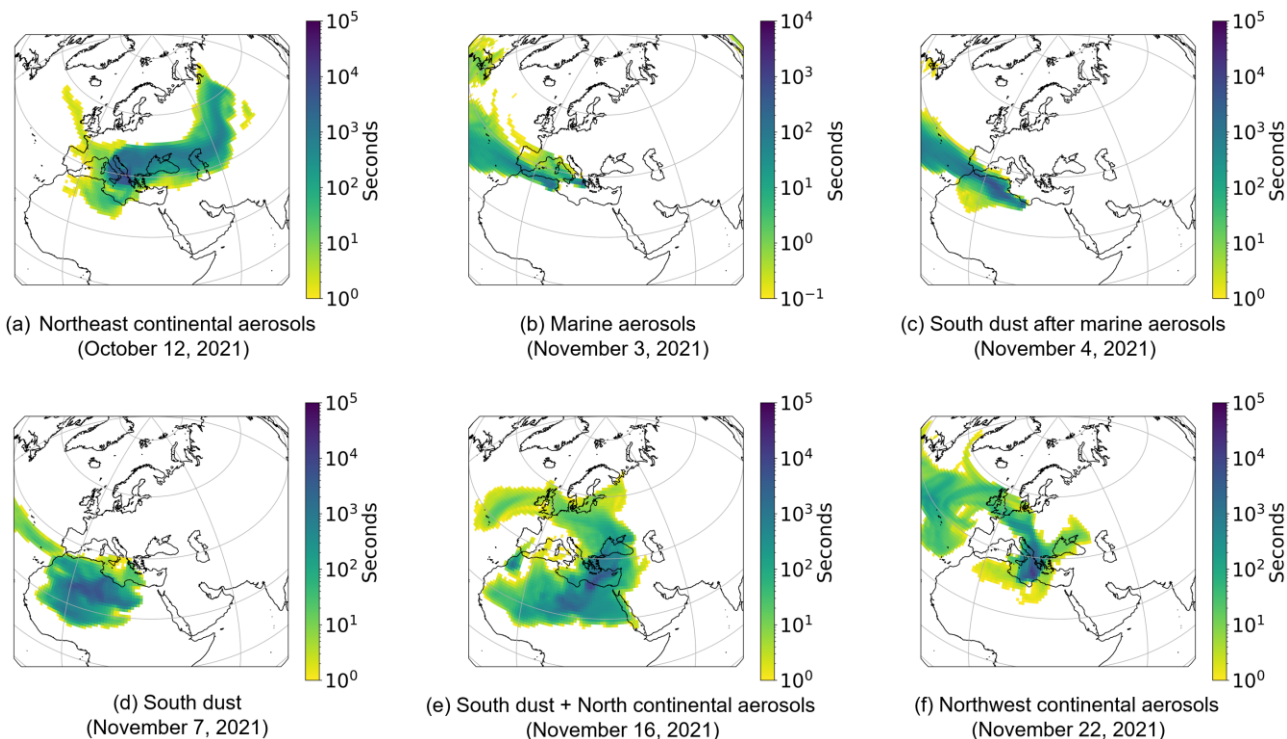
Figure 2. Overview of aerosol sources as seen from exemplary FLEXPART 10 day backward residence time maps. The colour map scales the residence time of the particles from a height between 0 and 500 m a.g.l. in the 10 d back trajectories. (a) Northeast continental air masses on October 12, 2021. (b) Marine air masses on November 3, 2021. (c) South dust after marine air masses on November 4, 2021. (d) South dust on November 7, 2021. (e) South dust + North continental air masses on November 16, 2021. (f) Northwest continental air masses on November 22, 2021.
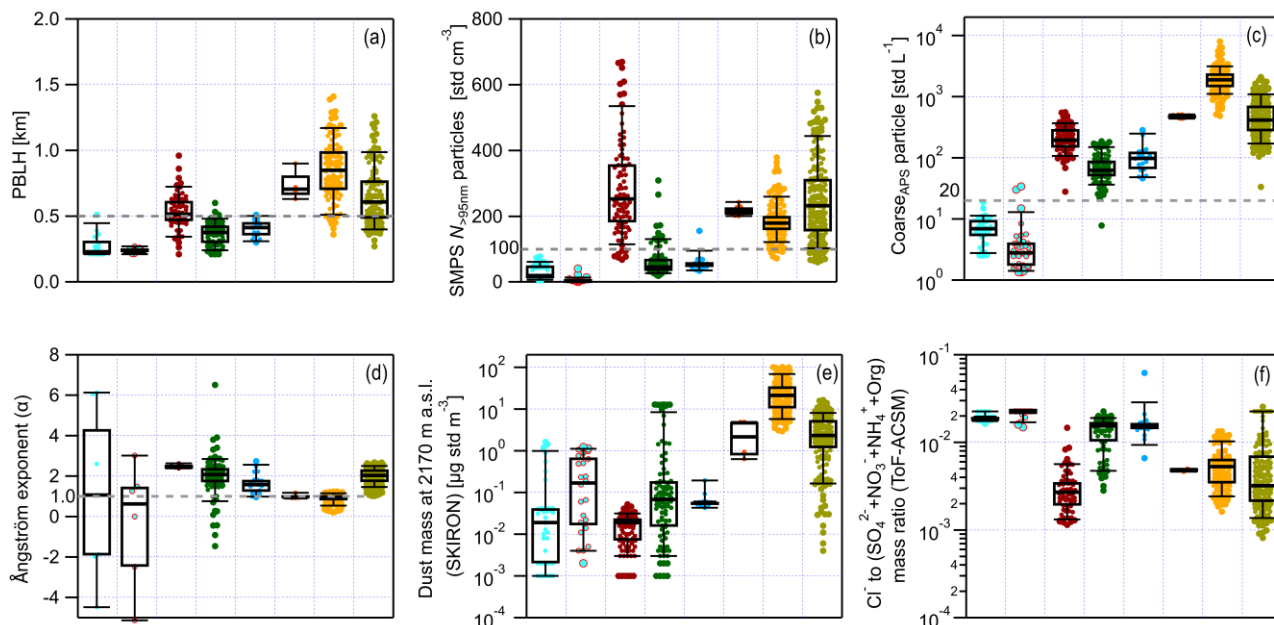
Figure 3. Box plots for the characteristics of identified aerosol sources. (a) PBLH with respect to VL. (b) Number concentration of particles larger than 95 nm measured by SMPS (SMPS $N_{>95nm}$) at (HAC)^2. (c) Coarse particle (>1.0 μm) number concentration measured by APS (Coarse$_{APS}$) at (HAC)^2. (d) Ångström exponent (α) at the wavelength pair of 450 and 700 nm calculated using nephelometer data recorded at (HAC)^2. (e) Dust mass concentration at 2170 m a.s.l. (~140 m below (HAC)^2) calculated by the SKIRON model. (f) The mass ratio of Cl$^-$ to other species measured by ToF-ACSM at (HAC)^2. The box shows the median line and the range between 25th and 75th quartiles. The lower and upper caps of the box indicate the 9th and 91th percentiles, respectively.

2.4 Aerosol source apportionment and type classification

In general, transported aerosol particles from remote regions showed trajectories from the north in earlier October at the beginning of the campaign and changed counter clockwise during the campaign. Figure 2 presents exemplary FLEXPART results throughout the campaign to show major aerosol sources from remote regions. Aerosol particles arriving at (HAC)^2 on October 12 (Figure 2a) came from the north and the northeast, which can be attributed to continental aerosols, while later on November 3, marine aerosols from the Atlantic Ocean and the Mediterranean Sea might make up a large fraction of aerosols transported to (HAC)^2 (Figure 2b). On November 4 and later, dust from the Sahara, possibly mixed with marine aerosols reach the station (Figure 2c and Figure 2d). Notably, the Saharan dust event increases the aerosol content (Figure 2c) by more than one order of magnitude compared to the marine aerosols (Figure 2b). At the beginning of the Saharan dust event, the case in Figure 2c spanned ~3 hours which might be a transition period with a lower mixture of local aerosols. After that, Saharan dust (Figure 2d) persisted for about one week. Later on, dust mixed with continental particles reached the site (Figure 2e), followed by primarily continental aerosols from the North of (HAC)^2, e.g., Balkans (Figure 2f). Note that FLEXPART results provide

an overview of aerosol sources on a daily basis, the further identification of particle sources at $(HAC)^2$ relies on both in-situ and remote sensing results with a time resolution of one hour. For example, the synergy of in-situ and remote sensing results enables to differentiate the distinct characters of the sources in Figure 2b and c.

260 In addition to aerosol footprints, we consider following criteria to specifically classify the sources of air masses at $(HAC)^2$:

- Comparing PBLH (SMPS $N_{>95nm}$) with a threshold value of 0.5 km (100 std cm^{-3}) to examine the relative position of $(HAC)^2$ with respect to the PBL
- Comparing $Coarse_{APS}$ with a threshold value of 20 std L^{-1} to judge the presence of remotely transported air masses in the FT
265
- Comparing Ze (MDV) with a threshold value of 10 dBZ (-0.5 m s^{-1}) to evaluate the presence of precipitation/clouds
- Comparing α with a threshold value of 1.0 to diagnose the occurrence of Saharan dust events

Figure 3 summarizes the classified aerosol sources and presents their characteristics to demonstrate their distinct nature as follows. Hourly-averaged data is presented in Figure 3, however, presented data for the source of South dust in PBL after marine aerosols in Figure 3 and following figures is resampled for every 15 minutes due to a short period of observation (< 3

270 hours). First, a PBLH less than 0.5 km or SMPS $N_{>95nm}$ less than 100 std cm^{-3} (if no PBLH results available) means $(HAC)^2$ is above the PBL (Figure 3a or b). Moreover, if $Coarse_{APS}$ is less than 20 std L^{-1}, the period will be attributed to $(HAC)^2$ in FT (Figure 3c). Furthermore, periods of Ze values larger than 10 dBZ (Hagen and Yuter, 2006) and MDV less than -0.5 m s^{-1} are classified as periods influenced by precipitation. For periods with slightly lower Ze values, $(HAC)^2$ is likely in-cloud or fogs. During the campaign, periods of precipitation frequently alternated with cloudy periods. Therefore, we consider such periods

275 jointly. If there is no influence from remotely transported air masses ($Coarse_{APS}$<20 std L^{-1}), depending on the presence of precipitation/clouds, the condition is classified as $(HAC)^2$ in FT under background condition and $(HAC)^2$ in FT with precipitation/clouds, respectively. For periods of $Coarse_{APS}$>20 std L^{-1}, the influence of remotely transported aerosols was considered. Continental aerosols have α values larger than 2.0 (Figure 3d) when $(HAC)^2$ is in the PBL. The distinct particle properties of continental aerosols also include high SMPS $N_{>95nm}$ (median value >200 std cm^{-3} in Figure 3b), moderate

280 $Coarse_{APS}$ values (median value ~200 std L^{-1} in Figure 3c) and very low dust particle abundance (<0.1 μg std m^{-3} in Figure 3e). Such an aerosol source is termed North continental aerosols in PBL. When continental aerosols are sources of particles at $(HAC)^2$ but the site is above the PBL (Figure 3a and 3b), the 75th quartile for $Coarse_{APS}$ of the aerosols decreases to 91 std L^{-1} (Figure 3c) which becomes lower than the 9th percentile for $Coarse_{APS}$ of North continental aerosols in PBL. Also, the α value of the source termed North continental aerosols above PBL decreases (25th quartile >1.67) but the median value is still higher

285 than 2.0 (Figure 3d). Therefore, North continental aerosols above PBL are distinctly different from the aerosols in the PBL. In addition, the distinction of marine aerosols above PBL is indicated by the highest Cl^- fraction range compared to the other scenarios not under the FT condition (Figure 3f), given that high Cl^- concentration is reported as a character of marine aerosols (Xiao et al., 2018). Khan et al. (2015) reported that the particle number concentration of coarse mode sea spray aerosols is less than that of dust aerosols by approximately 100 times, which is consistent with the observations in this study (Figure 3c).

290 Hence, a scenario of Marine aerosols above PBL can be classified. Followed by marine aerosols, a distinct period of several

11

hours (on November 4) at the beginning of a dust event (from November 4 to 10) was observed for (HAC)^2 in the PBL. It shows high Coarse$_{APS}$ particle concentrations (>450 std L^{-1} in Figure 3c), low α values (close to 1.0 in Figure 3d) and the presence of dust particles (Figure 3e). Thus, such a source is classified as South dust in PBL after marine aerosols. Afterwards, the dust event period is termed South dust in PBL which shows the highest Coarse$_{APS}$ particle concentration (9th percentile

295 >1000 std L^{-1} in Figure 3c), low α values (close to 1.0, Figure 3d) and the largest dust mass concentration (25th quartile >10 µg std m^{-3} in Figure 3e). Lastly, periods of aerosol footprints similar to Figure 2e and showing aerosol properties in Figure 3 between those of South dust and North continental aerosols are classified as South dust with North continental aerosols, i.e., a mixture of both aerosols. Hereafter, we use the remotely transported aerosols identified in Figure 3 to name the aerosol sources at (HAC)^2. However, we note that particles from local sources may also be relevant for aerosol particles reaching (HAC)^2

300 depending on the (HAC)^2 position with respect to the PBL.

Table 1. INP parameterizations from the literature.

INP Parameterization from literature	Region	Included major aerosol types	T range of INP observations	Formulation
DeMott2010	Global observation covering Colorado, Wyoming and Alaska in US, Eastern Canada and Ottawa, Pacific region and Amazon basin	Dust and biological particles	$-35 - -9$ °C ($S_w > 100\%$)	$N_{INP} = a(-T)^b * Total_{APS}^{(-cT+d)}$ (a = 0.0000594, b = 3.33, c = 0.0264, d = 0.0033) (Total$_{APS}$ in std cm^{-3}; T in °C)
Tobo2013FBAP	Rocky Mountain region	Biological particles	$-35 - -9$ °C ($S_w = 103 - 106\%$)	$N_{INP} = Fluo_{WIBS}^{(-aT+b)} * \exp(-cT + d)$ (a = −0.108, b = 3.8, c = 0, d = 4.605) (Fluo$_{WIBS}$[@] in std cm^{-3}; T in °C)
DeMott2015	Pacific Ocean basin and Virgin Islands	Laboratory dust samples and dust particles in the atmosphere	$-35 - -20$ °C ($S_w = 105\%$)	$N_{INP} = cf * Total_{APS}^{(-aT+b)} * \exp(-cT + d)$ (cf = 3, a = 0, b = 1.25, c = 0.46, d = −11.6) (Total$_{APS}$ in std cm^{-3}; T in °C)
Niemand2012	Laboratory experiments	Dust	$-36 - -12$ °C ($S_w > 100\%$)	$N_{INP} = 1000 * S_{SMPS+APS} * \exp(aT + b)$ (a = −0.517, b = 8.934) (S$_{SMPS+APS}$ in std m^2 cm^{-3}; T in °C)
Ullrich2017	Laboratory experiments	Dust	$-30 - -14$ °C ($S_w > 100\%$)	$N_{INP} = 1000 * S_{SMPS+APS} * \exp(a(273.15 + T) + b)$ (a = −0.517, b = 150.577) (S$_{SMPS+APS}$[#] in std m^2 cm^{-3}; T in °C)
McCluskey2018	West coast of Ireland	Sea spray aerosols, marine organics and offshore biological particles	$-27 - -10$ °C ($S_w > 100\%$)	$N_{INP} = 1000 * S_{SMPS+APS} * \exp(aT + b)$ (a = −0.545, b = 1.0125) (S$_{SMPS+APS}$ in std m^2 cm^{-3}; T in °C)

2.5 INP parameterization methods

INP parameterization is critically important for climate models to express cloud-aerosol interactions in both ice clouds and MPCs. As a minor subset of total aerosol particles, N_{INP} exponentially increases with decreasing T, as supported by the theory (Kampe and Weickmann, 1951) and observations (reviewed in Kanji et al., 2017). N_{INP} also shows dependence on the
310   concentration of available aerosol particles (Burrows et al., 2022) and characteristic of their surfaces (e.g., IN active site density), to trigger the activation (Vali et al., 2015; Knopf and Alpert, 2023). Demott et al. (2010) developed a parameterization (termed DeMott2010 in Table 1) to predict N_{INP} using T and the number concentration of aerosol particles larger than 0.5 μm (Total$_{APS}$), based on a suite of INP measurements at various locations globally. Tobo et al. (2013) augmented the DeMott2010 formulation and developed a new parameterization (termed Tobo2013FBAP in Table 1) to calculate N_{INP} using the number
315   concentration of fluorescent aerosol particles monitored by an UV-APS (Ultra-violet APS, n_{FBAPs}), to consider the explicit contributions from biological and dust particles in the coarse mode population. Compared to DeMott2010, Tobo2013FBAP shows increased predictability to calculate N_{INP} from aerosol sources containing biological particles (Tobo et al., 2013). Demott et al. (2015) used Total$_{APS}$ and augmented Tobo2013FBAP by introducing a calibration factor (*cf*) and calculated a new suite of parameters for the formulation by fitting to integrated laboratory and field data (termed DeMott2015 in Table 1). However,
320   the N_{INP} of different aerosol sources may not scale to the total aerosol particle number concentration (e.g., Total$_{APS}$ or n_{FBAPs}) following the same rule as used in the above-mentioned parameterizations. This is because the IN ability of potential INPs from different sources varies and different types of INPs dominate the N_{INP} in different T regimes (Murray et al., 2012; Kanji et al., 2017).

Particle-surface-area based approaches were also reported in the literature, such as approaches termed Niemand2012 (Niemand
325   et al., 2012), Ullrich2017 (Ullrich et al., 2017) and McCluskey2018 (Mccluskey et al., 2018) in Table 1. Given that different types of INPs originate from different sources may have different IN active site densities over the particle surface, the INP concentrations calculated from different particle-surface-area based approaches developed from different aerosol sources can vary by more than three orders of magnitude (Niemand et al., 2012; Mccluskey et al., 2018). Further improvements in INP prediction may require parameterizations to explicitly consider additional characteristics of resolved aerosol properties to point
330   to their sources. Mignani et al. (2021) reported that the ratio of large-sized aerosol particles (>2.0 μm) recorded by APS can be used as an identity to characterize INPs from Saharan dust and the implementation of the ratio into the INP parameterization improves its predictability. We expand upon this and use the detailed INP source apportionment and type classification (Section 2.4) to incorporate INP source characteristics into INP parameterizations developed here. The new parameterizations proposed for INPs at Mt. Helmos are expressed as a function of T, aerosol particle concentration recorded by APS or WIBS, and the

ratio of particle number concentration recorded in different channels of APS or WIBS. We demonstrate the feasibility of predicting INPs from different sources using one suite of parameters for the proposed parameterizations (see Section 3.4), as well as the superior performance of the new parameterizations compared to the approaches reported in the literature (Table 1).

3 Results and Discussions

In this section, we first provide evidence on the distinct characteristics of individual sources (Section 3.1) classified in Section 2.4. An overview of INPs observed at Mt. Helmos is presented as a function of T and the results are contrasted against literature observations, for both global and specifically for the Mediterranean region (Section 3.2). The INP abundance and its correlation with aerosol properties of each INP source are then examined. We also focus on a case study where precipitation effects on INPs in the PBL are explicitly studied (Section 3.3). Finally, the ability of published parameterizations to reproduce observed INPs at Mt. Helmos is examined, followed by the introduction of new parameterizations we develop that explicitly consider characteristics of different INP sources and display superior performance (Section 3.4).

3.1 Properties of identified aerosol sources

3.1.1 The particle size distribution for different aerosol types and airmass classifications

Error! Reference source not found.a shows the combined particle size distribution of different INP sources measured by both SMPS and APS. Scatter plots in **Error! Reference source not found.**b and 4c present the apportionment of fine (<1.0 μm, Fine$_{SMPS+APS}$ in **Error! Reference source not found.**b and Fine$_{APS}$ in **Error! Reference source not found.**c) and coarse (>1.0 μm, Coarse$_{APS}$) particles for different aerosol sources. The results of the concentration of aerosol particles in different size ranges are provided in Fig. S2. Based on all observations, we summarize that aerosols at (HAC)^2 during CALISHTO generally exhibit four size modes: an ultrafine mode (D_a<0.04 μm), an Aitken mode (0.04<D_a<0.1 μm), an accumulation mode (0.1<D_a<1.0 μm), and a coarse mode (D_a>1.0 μm). When (HAC)^2 is in the FT, aerosol particles in the size range D_a>0.1 μm (**Error! Reference source not found.**a), with and without the influence of precipitation/clouds, exhibit a similar size distribution with characteristic decrease of number with increasing size resembling a power-law (Kim et al., 1992). Particles larger than 4.0 μm in the FT show negligible amounts. Precipitation/clouds decrease the amount of particles smaller than 0.4 μm, while the absence of a distinct accumulation mode may suggest inappreciable influences from anthropogenic surface emissions on FT aerosols (Ran et al., 2022).
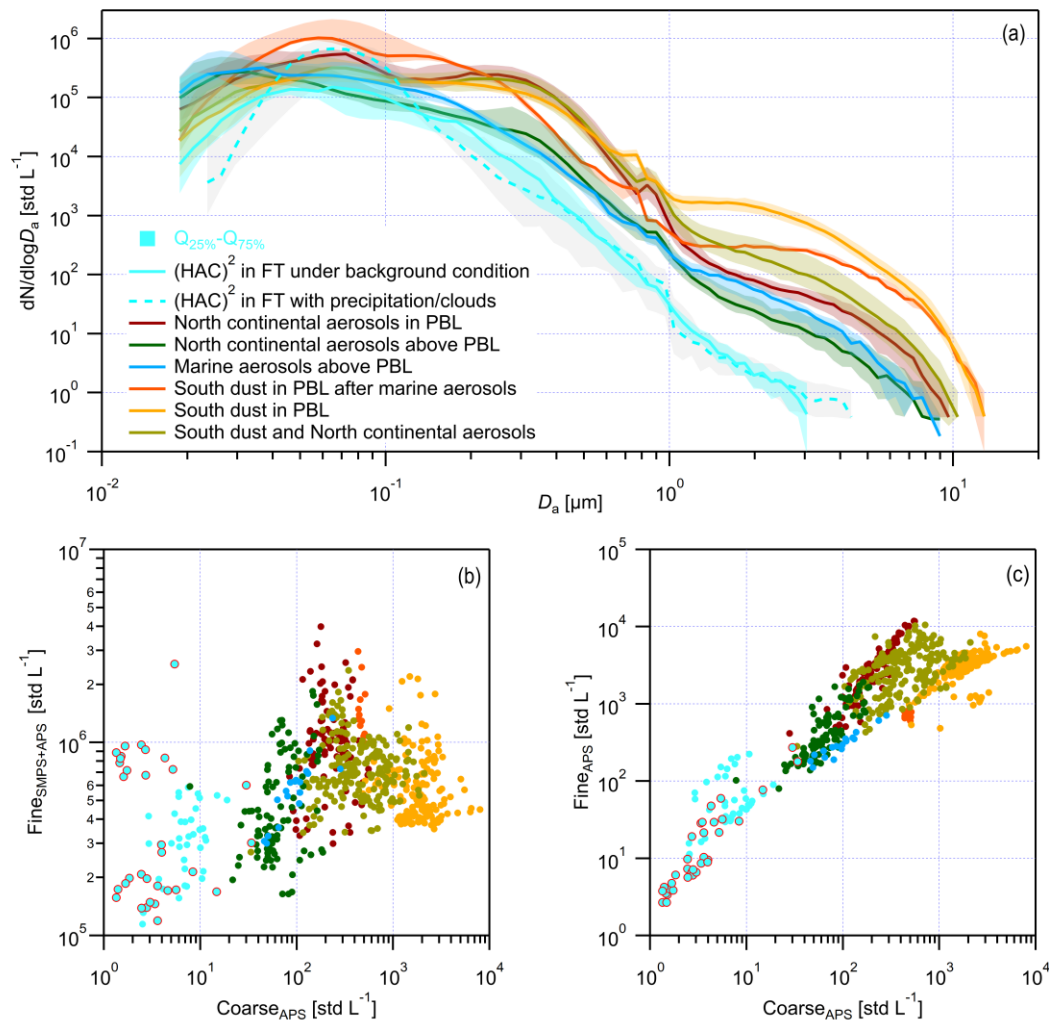
Figure 4. Particle size distribution of different aerosol sources. (a) Combined size distribution of particles measured by SMPS (10–800 nm in mobility diameter) and APS (0.5−20 μm in aerodynamic diameter). The solid line is the median of the particle size distribution. The shading area shows the 25th to 75th percentiles of the particle size distribution of each aerosol source. (b) Scatter plots of Coarse$_{APS}$ particle (>1.0 μm, on the *x*-axis) number concentration and Fine$_{SMPS+APS}$ particle (particles <1.0 μm measured by both SMPS and APS, on the *y*-axis) number concentration. (c) Scatter plots of Coarse$_{APS}$ particle (>1.0 μm, on the *x*-axis) number concentration and Fine$_{APS}$ particle (particles <1.0 μm measured by APS, on the *y*-axis) number concentration. The aerosol sources are indicated in the legend in panel a.

FT aerosols with D_a<0.1 μm under both background and precipitation/clouds conditions show a broad Aitken mode, but the latter condition tends to supress the ultrafine and accumulation modes (**Error! Reference source not found.**a). Such a size growth for Aitken mode particles and a number concentration decrease in ultrafine particles may be facilitated by the larger temperature and relative humidity gradients during precipitation/clouds periods both of which promote particle growth and gas-to-particle conversion processes (Schroder and Strom, 1997; Bates et al., 1998; Kamra et al., 2003; Peter et al., 2010). Such processes are also promoted by particle decreases in the accumulation mode, leading to decreased sinks for ultrafine

15

particles and gas phase materials (Khadir et al., 2023). As shown in **Error! Reference source not found.**b, the increase in
Fine$_{SMPS+APS}$ particles may not always happen in the FT with the presence of precipitation/clouds. Nonetheless, while new
particle formation and particle growth are often reported under PBL conditions, we show that it may also occur under FT
conditions (Kerminen et al., 2018).

Among all aerosol sources, North continental aerosols in PBL shows the largest particle concentration in the accumulation
mode indicating substantial influences from anthropogenic particles (Zaizen et al., 2004). North continental aerosols in PBL
also contains some Aitken and coarse mode particles. Above the PBL, an overall particle number decrease for Aitken,
accumulation and coarse modes can be observed for North continental aerosols while it shows an increase in ultrafine mode
particles, which is in agreement with Ristovski et al. (2010) reporting the size distribution of continental aerosols penetrated
into the FT. Showing an overall overlapped $Q_{25\%}$–$Q_{75\%}$ range (**Error! Reference source not found.**a), marine aerosols have
a similar particle size distribution as North continental aerosols when both are above the PBL. Following marine aerosols, a
dust plume intrusion period in the PBL (South dust in PBL after marine aerosols) shows a particle size distribution with
substantial increases in coarse, accumulation and Aitken modes, which agrees with the aerosol content increase presented in
Figure 2c compared to Figure 2b, but it shows a slight decrease in ultrafine mode particles. The large increase in coarse mode
particles, especially particles larger than 10 μm (**Error! Reference source not found.**a), suggests a concurrent presence of
dust particles (Brunner et al., 2021). The increase in accumulation and Aitken mode particles may be attributed to the diurnal
cycling of (HAC)^2 in and out of the PBL. Gini et al. (2022) noted that Saharan dust events are usually associated with lower
PBLH. The distinct size distribution characteristic of South dust in PBL is its highest concentration of coarse mode particles
among all aerosol sources but the source contains less finer particles (<1.0 μm, **Error! Reference source not found.**b and c).
Lastly, the source of South dust and North continental aerosols shows a size distribution with coarse mode particles between
South dust in PBL and North continental aerosols in PBL, and the mixed source shows slightly less particles in the other modes
compared to North continental aerosol source in PBL.

3.1.2 Fluorescent properties of particles from different aerosol sources

Figure 5 andFigure 6 present the relative fractions and size distributions of different types of fluorescent particles for different
aerosols sources, respectively. Figure 7 provides the results of Fluo$_{WIBS}$ particle number concentration, asphericity factor of
Fluo$_{WIBS}$ particles, the correlation between Fluo$_{WIBS}$ particles and dust (eBC) mass concentration in different aerosol sources.
Figure 5a shows that when (HAC)^2 is in the FT under background condition without the influence of remotely transported
airmasses, fluorescent particles are mainly comprised of B$_{WIBS}$, C$_{WIBS}$ and BC$_{WIBS}$ types, as well as a few A$_{WIBS}$ and ABC$_{WIBS}$
particles. The particles detected in B$_{WIBS}$, C$_{WIBS}$ and BC$_{WIBS}$ channels may be attributed to non-biological fluorescent particles
(Crawford et al., 2016; Ziemba et al., 2016), whereas the signals for A$_{WIBS}$ and ABC$_{WIBS}$ channels are probably from
bioaerosols (Crawford et al., 2015). Despite a low number concentration of fluorescent particles when (HAC)^2 is in the FT
under background condition (Figure 6 and Figure 7a), some of the fluorescent particles with biogenic materials may contribute
to the INPs. With the influence of precipitation/clouds in the FT, the dominance of A$_{WIBS}$ and ABC$_{WIBS}$ particles and the

fraction increase in AB$_{WIBS}$ particles (Figure 5a) may be attributed to bacteria for small-sized particles (<2.0 μm) and fungal spores or plant fragments for large-sized particles (>2.0 μm). This is consistent with the release of biological particles during or after precipitation/clouds events (Prenni et al., 2013; Joung et al., 2017; Iwata et al., 2019; Negron et al., 2020; Khadir et al., 2023). Those biological particles are potentially active INPs at warm temperatures.
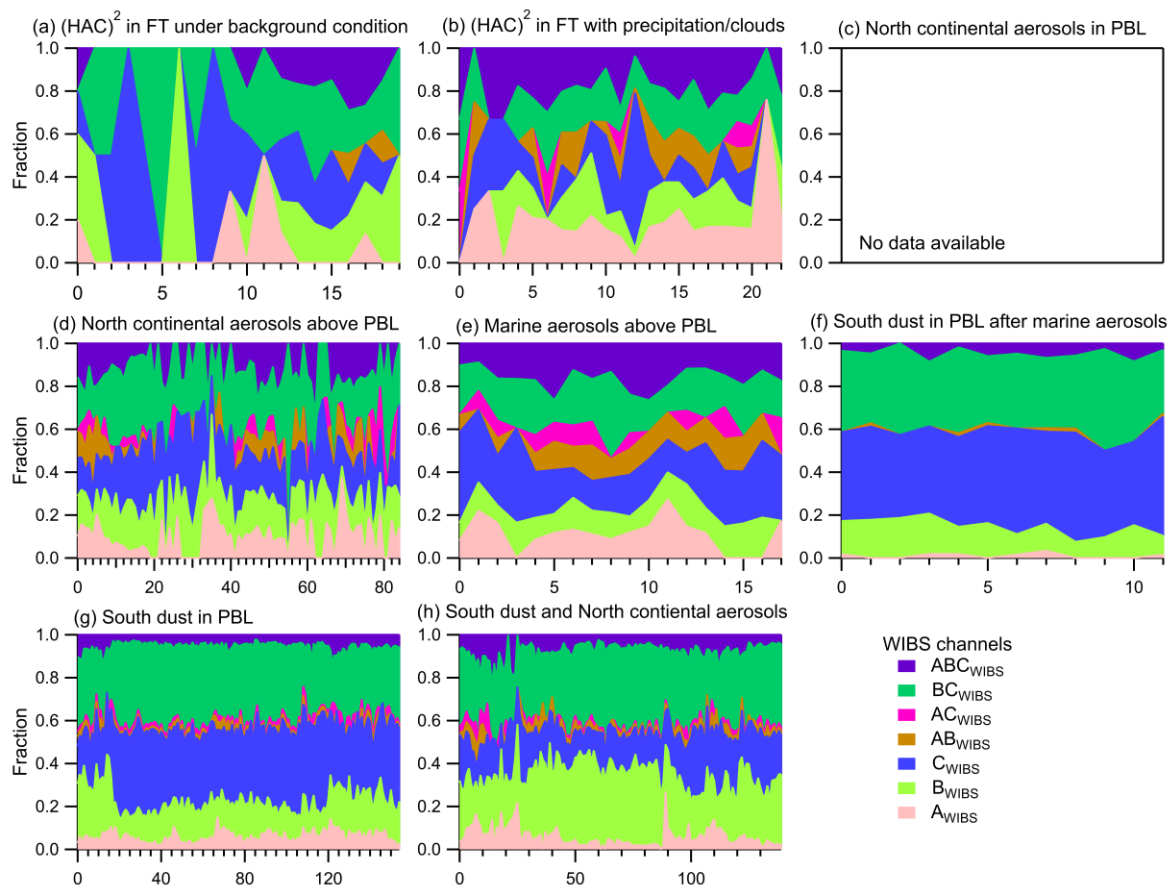
Figure 5. The fraction pattern of different types of fluorescent particles classified by WIBS. Different particle types are indicated in the legend. The *x*-axis indicates the number of observations and the *y*-axis scales the fraction of each type of particle from an identified aerosol source. WIBS data was resampled every 15 minutes for the source of South dust in PBL after marine aerosols due to a short period of observation (< 3 hours), and hourly averaged results were presented for the rest aerosol sources.

For North continental aerosols and marine aerosols above the PBL, both aerosol sources contain particles from all WIBS channels and the only difference is that the former has more observation data (Figure 5d and e). This means both aerosol sources contain similar types of fluorescent particles which might be in a mixed state of biological particles and interfering particles, such as dust particles carrying biological matters. Tang et al. (2022a) reported that biological particles in continental aerosols are majorly observed in A$_{WIBS}$, AB$_{WIBS}$ and ABC$_{WIBS}$ channels. It is also reported that biological particles in marine aerosols may show fluorescence in A$_{WIBS}$, B$_{WIBS}$, AB$_{WIBS}$ and ABC$_{WIBS}$ channels (Kawana et al., 2021; Moallemi et al., 2021).

Some of C_{WIBS} (~20%) and BC_{WIBS} (~20%) particles in marine and continental aerosols above PBL may be attributed to residual particles associated with fluorescent materials but not necessarily to be biological particles (Pöhlker et al., 2012).
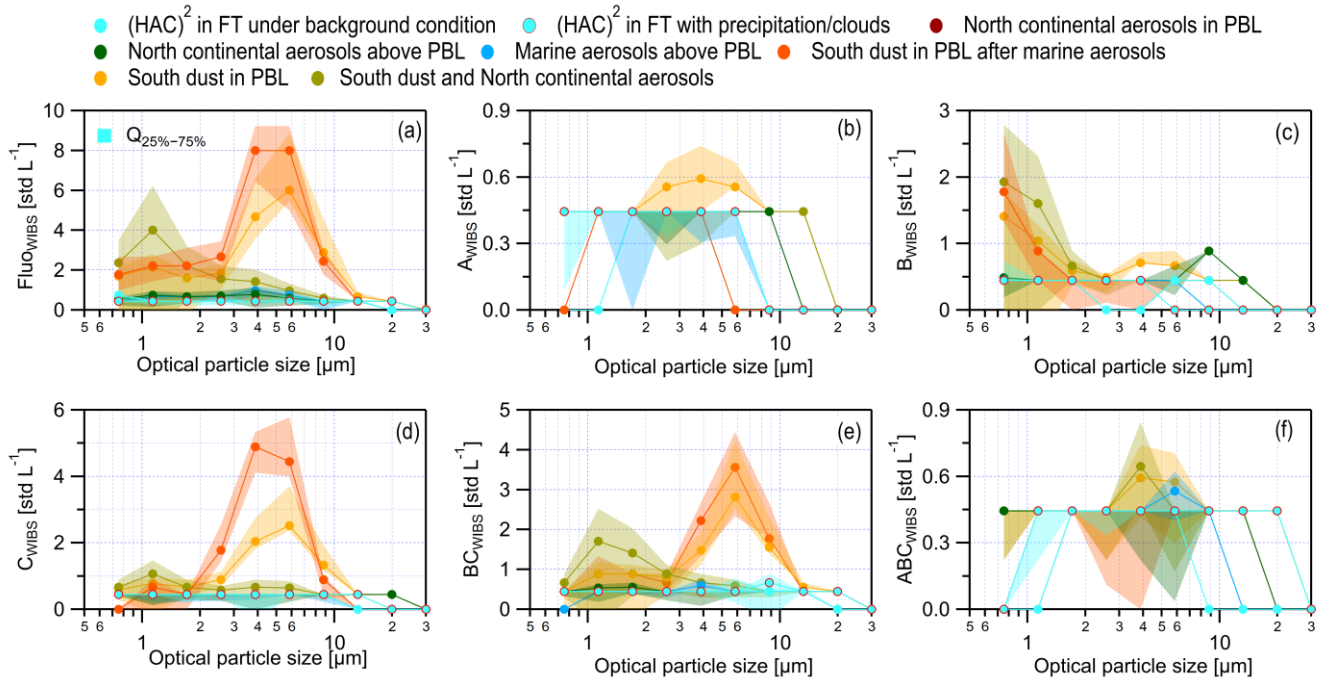
Figure 6. Fluorescent particle number concentration in 10 different size bins, including [0.50 0.75 μm], (0.75 1.13 μm], (1.13 1.71 μm], (1.71 2.57 μm], (2.57 3.87 μm], (3.87 5.83 μm], (5.83 8.78 μm], (8.78 13.22 μm], (13.22 19.92 μm], (19.92 30.00 μm]. Data points stand for median values. The uncertainty is the range between 25th and 75th percentiles, indicated by $Q_{25\%-75\%}$. Different aerosol sources are indicated in the legend. No WIBS data are available for the source of North continental aerosols in PBL. Different types of fluorescent particles are presented in different panels, including (a) $Fluo_{WIBS}$, (b) A_{WIBS}, (c) B_{WIBS}, (d) C_{WIBS}, (e) BC_{WIBS}, (f) ABC_{WIBS}. The results for AB_{WIBS} and AC_{WIBS} are not presented because they are minor in all aerosols sources.

The major types of fluorescent particles for aerosol sources containing dust particles, i.e., South dust in PBL after marine aerosols and South dust in PBL, are B_{WIBS}, C_{WIBS} and BC_{WIBS} (Figure 5). This is consistent with Longo et al. (2014) and Violaki et al. (2021), both of which showed a strong association of bioaerosol with mineral dust plumes. This is also in agreement with Yue et al. (2022) who reported the correlation between dust particles and C_{WIBS} (also BC_{WIBS}) particles. It is also reported that soil dust may be co-emitted with organics (O'sullivan et al., 2014) that may show fluorescent in B_{WIBS} and C_{WIBS} channels (Després et al., 2012; Graber and Rudich, 2012). According to the results shown in Figure 6c, d and e, B_{WIBS} particles in dust-containing aerosols are generally of small sizes (< 2.0 μm) whereas both C_{WIBS} and BC_{WIBS} particles have larger sizes (> 2.0 μm). This suggests that B_{WIBS} particles might be attributed to small-sized soil dust particles, and both C_{WIBS} and BC_{WIBS} particles may be more relevant for large-sized mineral dust particles that show fluorescence. Furthermore, the results in Figure 7c and d indicate that fluorescent particles in dust plumes may not be purely bioaerosols given the weak correlation between ABC_{WIBS} and dust mass concentration estimated by the SKIRON model ($R = 0.14$ and $\rho = 0.35$). We note that C_{WIBS} and BC_{WIBS} particles might be the most relevant types of fluorescent particles for mineral dust from Saharan dust, supported by the

18

strong and significant correlations between the calculated dust mass concentration and C_{WIBS} (or BC_{WIBS}) particles, compared to the other types of fluorescent particles showing insignificant correlations (Fig. S3 in Supplement S3).
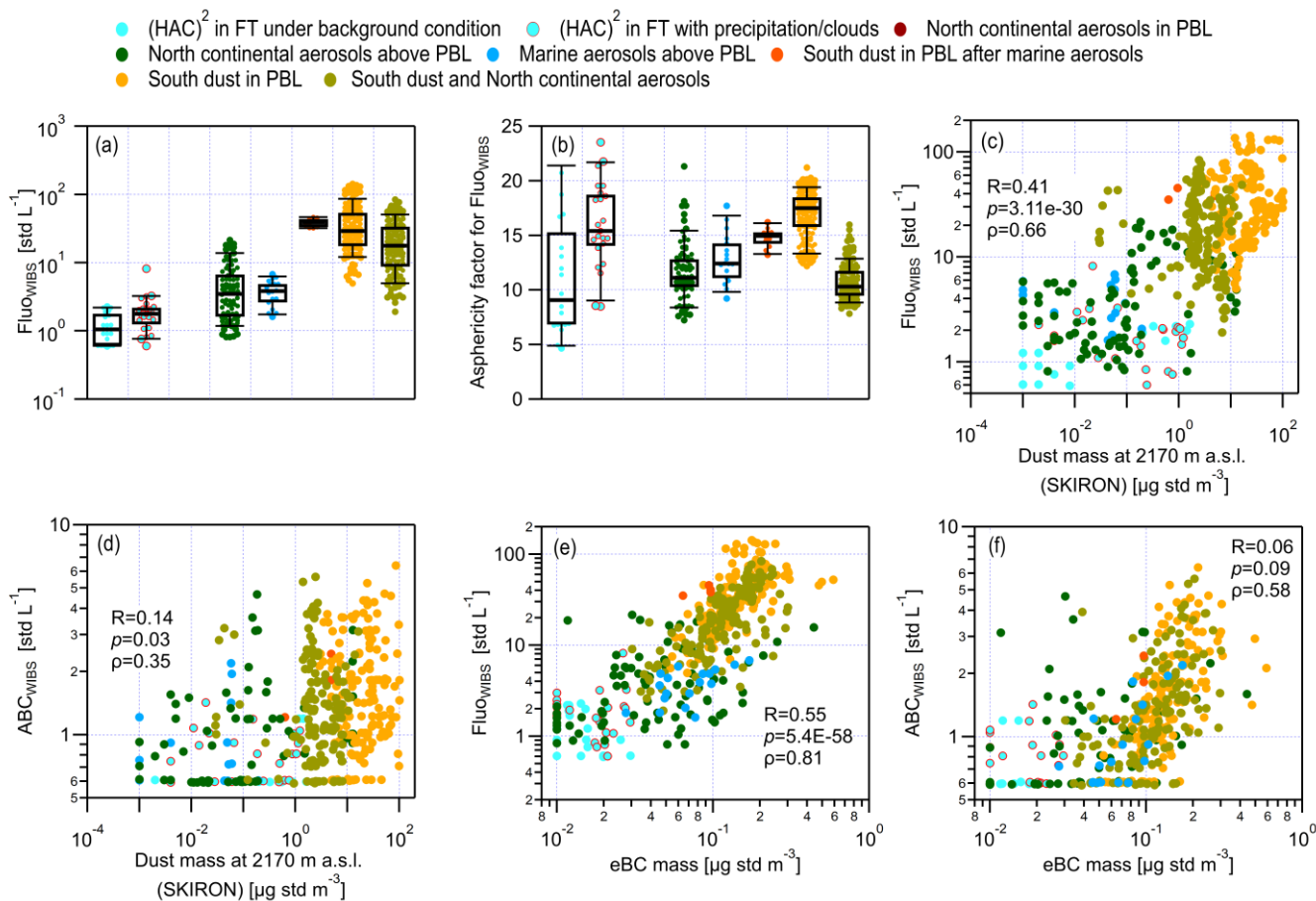

445

Figure 7. Fluorescent properties of aerosol particles from different sources. (a) Number concentration of Fluo$_{WIBS}$ particles. (b) Asphericity factor of Fluo$_{WIBS}$ particles. (c) Scatter plots of Fluo$_{WIBS}$ particle concentration and dust mass concentration estimated by the SKIRON model at 2170 m a.s.l. (~ 140 m lower than (HAC)^2) (d) Scatter plots of ABC$_{WIBS}$ particle concentration and dust mass concentration estimated by SKIRON at 2170 m a.s.l. (e) Scatter plots of Fluo$_{WIBS}$ particle concentration and eBC mass
450 **concentration. (f) Scatter plots of ABC$_{WIBS}$ particle concentration and eBC mass concentration. The Pearson correlation coefficient (R) and corresponding p value calculated from F-test, and Spearman's rank coefficient (ρ), are provided to evaluate the correlation between parameters on the x-axis and y-axis.**

Small-sized carbonaceous (Bond et al., 2013) and combustion-generated particles can carry PAHs or other compounds that fluoresce (Fennelly et al., 2017), and may contribute to the B$_{WIBS}$, C$_{WIBS}$ and BC$_{WIBS}$ populations (Figure 6c, d and e). This is
455 supported by the significant correlation ($p < 0.05$) between Fluo$_{WIBS}$ particles and eBC mass concentration (Figure 7e). ABC$_{WIBS}$ however does not correlate with eBC mass concentration (Figure 7f) suggesting that ABC$_{WIBS}$ is indeed a distinct population – biological particles – and not affected by sources that contribute to eBC. Results in Fig. S4 (Supplement S3) show that eBC particles are generally correlated with B$_{WIBS}$, C$_{WIBS}$ and BC$_{WIBS}$ populations. Compared to the aerosol source of South dust in PBL, the mixed source of South dust and North continental aerosols shows a larger fraction in B$_{WIBS}$ but a smaller

19

fraction in C_{WIBS} particles (Figure 5g and h). The higher content of B_{WIBS} particles may be explained by a larger particle number concentration of small-sized carbonaceous particles (< 2.0 μm), such as soot from anthropogenic emissions in continental sources. Furthermore, the small fraction of A_{WIBS} and ABC_{WIBS} particles in dust (Figure 5g and h) suggests the presence of biological particles from near ground sources in the PBL. This can be explained by the high PBLH conditions (Figure 3a) that exceed the $(HAC)^2$ altitude, meaning that the site is in the PBL and directly influenced by bioaerosols emitted by the surrounding forested area, such as bacteria, fungi and/or fungal spores.

Comparing $Fluo_{WIBS}$ and ABC_{WIBS} particles in different aerosol sources in and above the PBL (Figure 6 and Figure 7), it shows that sources in the PBL contain more fluorescent particles by approximately one order of magnitude than those sources above the PBL. This suggests particles from biogenic sources can be significantly reduced when the atmospheric condition changes from the PBL to FT. In addition, we discuss the impacts of anthropogenic emissions on different aerosol sources by using the observed eBC results. Figure 7e and f show that all identified aerosol sources contain eBC, despite low eBC concentrations under conditions in the FT with and without precipitation/clouds (<0.05 μg std m^{-3}). This means anthropogenic pollution may impact $(HAC)^2$ even when it is in the FT (Collaud Coen et al., 2018). Also, it shows that the occurrence of precipitation/clouds does not completely remove eBC (Figure 7e and f), likely due to its hydrophobic properties (Gao et al., 2022). North continental aerosols show a higher eBC concentration in the PBL than above PBL, also indicating the importance of atmospheric condition in determining anthropogenic emission impacts. The presence of eBC in long range transported marine aerosols above the PBL may suggest the long atmospheric residence time of eBC. The high eBC mass concentration observed in South dust aerosols may be due to the air mass exchange between dust plume and PBL aerosols, given that dust events may suppress PBL air masses and enhance air parcel entrainment (Zhang et al., 2022).

3.2 INPs at Mt. Helmos

3.2.1 Overview

INP concentrations at Mt. Helmos (Figure 8) generally increase with decreasing T; the concentration spans from 10^{-3} to 10^2 std L^{-1}. For $T > -15$ °C, the observed INPs may be attributed to biological particles, especially at the warmest temperatures (Murray et al., 2012; Kanji et al., 2017). These bioaerosols may originate from local and/or transported continental biogenic sources, such as vegetation and living organisms, and also from sea surface microlayer which releases marine diatoms and/or diatom exudates (Després et al., 2012). Soil dust emitted from agricultural lands (local and continental), which are reported to be able to nucleate ice at $T > -10$ °C (Garcia et al., 2012; Harrison et al., 2016; Hill et al., 2016), and organic material emitted by marine organisms, some of which can freeze at T close to -10 °C via the immersion freezing mode (Wilson et al., 2015), may also contribute to INPs observed at warm temperatures. The higher median INP concentrations at $T > -10$ °C observed at Mt. Helmos compared to those of lower temperatures (at -11 °C and -12 °C) are due to the limited observations at such warm temperatures. Also, we note that the INSEKT measurement uncertainty is higher at warmer T. For $T < -15$ °C (> -27 °C), mineral dust and soil dust of arid and agricultural origins, are more important INPs than bioaerosols (Hoose and Möhler, 2012;

Murray et al., 2012; Tobo et al., 2014). Moreover, local and transported ash particles emitted from industrial coal combustion and domestic fuel use, may contribute to the observed INPs for $T < -15$ °C (Umo et al., 2015). Additionally, we note that INPs observed by PINE at $T = -24$ °C show higher concentrations than those measured by INSEKT at the same T. This may partly

495   result from the decreased particle collection efficiency of INSEKT filters due to over loading under high particle concentration conditions. The INP concentration difference is more pronounced at $T = -24$ °C because this temperature was employed for PINE experiments to observe a long period dust event from November 4 to 10. More details about the difference between INPs recorded by PINE and INSEKT are provided in the Supplement S4 (Figs. S5 and S6). Note that PINE, measuring INPs activated by different IN mechanisms (Möhler et al., 2021), is technically different from INSEKT that only detects INPs in the

500   immersion freezing mode. This may also partly explain the higher INP concentrations observed from PINE compared to INSEKT. Moreover, some INPs may not be tested by INSEKT if aerosol particles collected on the filter are not extracted completely. Therefore, PINE reports higher INP concentrations than INSEKT because PINE tests INPs in total aerosols.
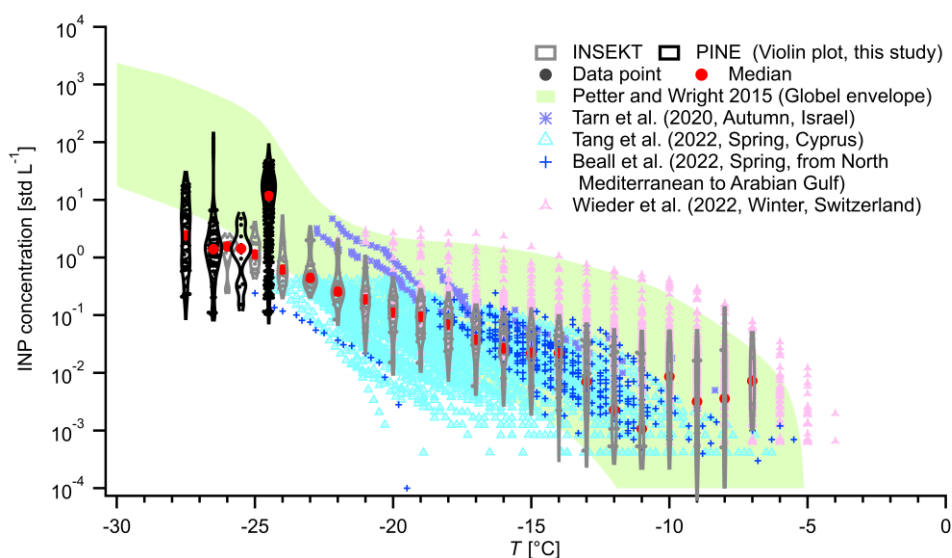

Figure 8. INP concentrations observed at Mt. Helmos as a function of temperature (T) contrasted against INP levels reported in
505   **selected field campaigns in Mediterranean region (Tarn et al., 2020; Beall et al., 2022; Tang et al., 2022b; Wieder et al., 2022) and from an global envelope (Petters and Wright, 2015). INP data measured by offline INSEKT and online PINE in this study are presented as violin plots, indicated by grey and black violin box, respectively. Each violin box presents data points in a T interval of 1 °C. Red round markers in the violin box represent the median value. Symbols for PINE INPs are offset by −0.5 °C for legibility. Higher PINE INP concentrations at −24°C compared to lower temperatures are because PINE was run during the Saharan dust**
510   **event (i.e., the source of South dust in PBL as defined in Figure 3) whereas INPs at lower temperatures originate from other aerosol sources with lower IN abilities.**

Figure 8 also shows that INPs at Mt. Helmos are generally distributed in the global envelope range reported by Petters and Wright (2015), particularly for $T > -25$ °C, and are also consistent with the results reported for other campaigns in Mediterranean region (Tarn et al., 2020; Beall et al., 2022; Tang et al., 2022b). Wieder et al. (2022) observed higher INP

515   concentrations over Alps in wintertime compared to this study for $T > -20$ °C. This may be attributed to a larger vegetation coverage (or differences in species, rainfall or season) in the wintertime Alps, hence larger bioaerosol sources relevant for

INPs, compared to Mt. Helmos. Also notable is that Wieder et al. (2022) report INPs active at T as high as −4 °C, which implies the presence of INPs that are more efficient in the Alps than at Mt. Helmos.
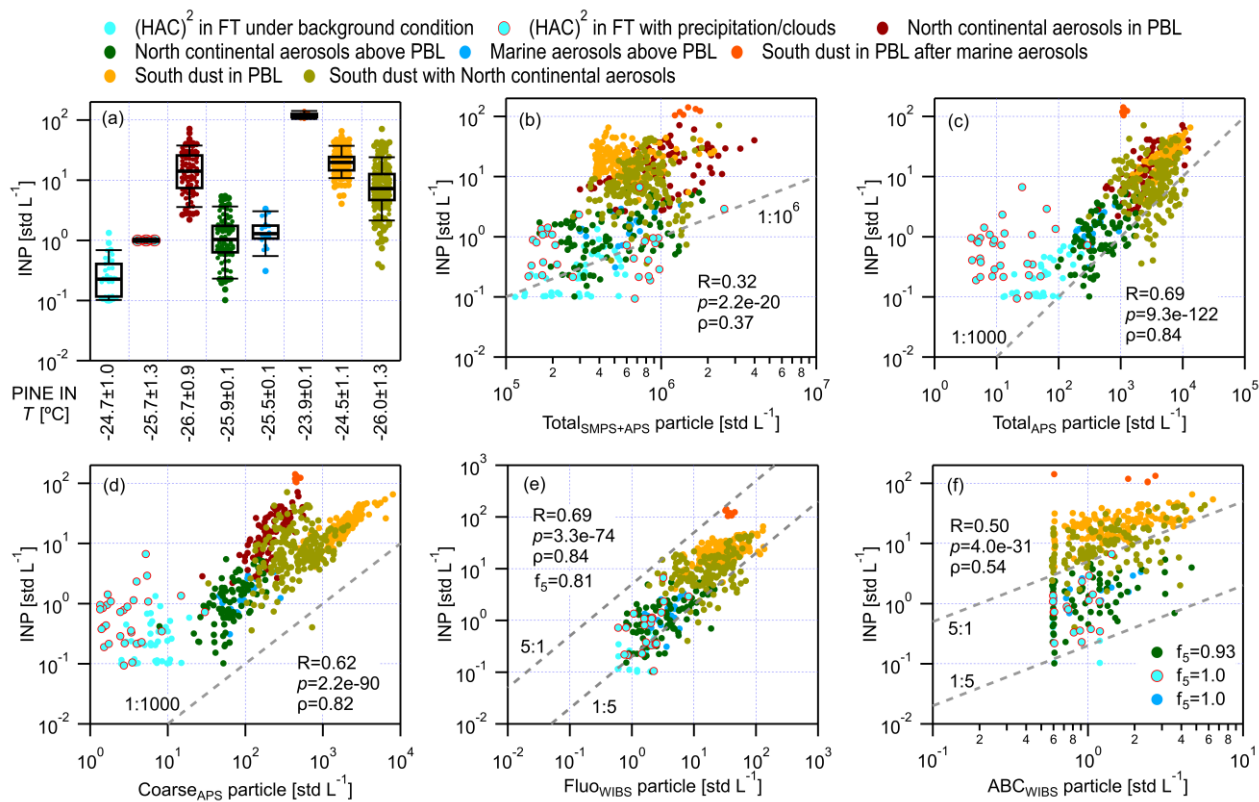
Figure 9. PINE INP concentration in different aerosol sources and the relation between INP and aerosol particle concentrations. (a) Box plots for INP concentration in different aerosol sources. The average T for PINE IN experiments for each source is indicated at the bottom axis and the uncertainty stands for one standard deviation. (b) Scatter plots of INP and Total$_{SMPS+APS}$ concentrations. (c) Scatter plots of INP and Total$_{APS}$ concentrations. (d) Scatter plots of INP and Coarse$_{APS}$ concentrations. (e) Scatter plots of INP and Fluo$_{WIBS}$ concentrations. (f) Scatter plots of INP and ABC$_{WIBS}$ concentrations. The Pearson correlation coefficient (R) and corresponding p value calculated from F-test, and Spearman's rank coefficient (ρ), are provided to evaluate the correlation between INP concentration and different aerosol particle concentrations. The p value is the probability of obtaining an R value no smaller than the true R value if there is no linear correlation between INPs and the given parameter.

3.2.2 INP concentrations for different sources

The high frequency of PINE measurements allows for the calculation of hourly-averaged INP concentrations for different aerosol sources. The small T spread (< 4.0 °C) of PINE measurement conditions throughout the campaign also allows for a thorough comparison of INP abundance from different sources (at similar T). As shown in **Error! Reference source not found.**, INP concentration is less than 1.0 std L^{-1} ($T = -24.7$ °C) when (HAC)^2 is in the FT under background condition without precipitation/clouds. This is in agreement with Lacher et al. (2021) who measured INPs at Jungfraujoch in Switzerland under FT conditions (reported range, 0.01 and 1.0 std L^{-1} at −25 °C in immersion freezing mode). Note that the lower INP

22

concentrations observed at Jungfraujoch compared to (HAC)² can be attributed to the much higher altitude of the former. Also, the results in **Error! Reference source not found.**a, c and d are consistent with Mignani et al. (2021) who reported decreased Total$_{APS}$ and Coarse$_{APS}$ particles but slightly increased INPs after precipitations. With the influence of precipitation/clouds, INPs at (HAC)² in the FT approximately increase to 1.0 std L^{-1} ($T = -25.7$ °C). The enriched INPs may be attributed to cloud-

540 processed particles (Khadir et al., 2023) and the near-ground released bioaerosols (likely A$_{WIBS}$, AB$_{WIBS}$ and ABC$_{WIBS}$ in Figure 5a) produced by the precipitation splash (Prenni et al., 2013; Joung et al., 2017). Cloud-processed particles, being a result of evaporated/sublimated hydrometeors, are originally active INPs and show enhanced IN ability compared to the particles before cloud-processing (Jahl et al., 2021). In addition, during precipitation/clouds periods, PBL airmasses containing bioaerosols close to the cloud base may be entrained into the FT close to the cloud top, such that more INPs are measured at (HAC)² in

545 the FT. We also note that the overall 1.0 °C lower T conditions for PINE experiments for (HAC)² in the FT with precipitation/clouds may also partly contribute to its higher tested INPs.

Table 2. The Pearson correlation coefficient (R) and Spearman's rank coefficient (ρ) for the relationship evaluation between INP and aerosol particle concentration from different sources. A critical p value of 0.05 from F-test for R is used to assess the significance level of the relationship. A p value smaller than 0.05 suggests that the probability of obtaining an R value no smaller than the true R

550 value is less than 5% if there is actually no liner correlation between INPs and the given parameter, thus the calculated R is of statistical significance. Evaluated significant relationship is indicated in bold. Note that the correlation between INPs and Total$_{WIBS}$ particles is not included in Fig. 9 but provided in Fig. S7 in Supplement S5.

INP sources	Totals$_{SMPS+APS}$[a]		Total$_{APS}$[b]		Coarse$_{APS}$[c]		Total$_{WIBS}$[d]		Fluo$_{WIBS}$[e]		ABC$_{WIBS}$[f]	
	R (p)	ρ	R (p)	ρ	R (p)	ρ	R (p)	ρ	R (p)	ρ	R (p)	ρ
(HAC)² in FT under background condition*	**0.41** **0.01**	0.57	**0.76** **<0.001**	0.66	0.13 0.46	0.19	0.41 0.07	0.31	**0.53** **0.03**	0.34	−0.50 0.22	−0.43
(HAC)² in FT with precipitation/clouds	0.28 0.10	0.06	0.09 0.62	0.11	0.04 0.81	0.03	0.17 0.45	0.27	**0.52** **0.01**	0.56	**0.56** **0.01**	0.33
North continental aerosols in PBL	**0.33** **0.003**	0.35	**0.71** **<0.001**	0.78	**0.73** **<0.001**	0.72	NA[g]	NA	NA	NA	NA	NA
North continental aerosols above PBL	**0.53** **<0.001**	0.34	**0.53** **<0.001**	0.48	**0.59** **<0.001**	0.54	**0.53** **<0.001**	0.45	**0.62** **<0.001**	0.58	**0.32** **0.008**	0.30
Marine aerosols above PBL	**0.61** **0.007**	0.48	**0.53** **0.02**	0.69	**0.48** **0.04**	0.69	**0.60** **0.009**	0.67	**0.55** **0.02**	0.47	**0.71** **<0.001**	0.71
South dust in PBL after marine aerosols	0.59 0.21	0.71	0.12 0.82	0.26	0.01 0.99	0.03	−0.17 0.75	−0.26	−0.38 0.46	−0.43	−0.59 0.29	0.36
South dust in PBL	0.05 0.56	0.01	**0.80** **<0.001**	0.80	**0.84** **<0.001**	0.85	**0.84** **<0.001**	0.85	**0.56** **<0.001**	0.52	**0.59** **<0.001**	0.50
South dust with North continental aerosols	**0.29** **<0.001**	0.09	**0.24** **0.001**	0.21	0.13 0.07	0.34	**0.21** **0.01**	0.29	**0.59** **<0.001**	0.38	**0.65** **<0.001**	0.51
All observations	**0.32** **<0.001**	0.37	**0.69** **<0.001**	0.84	**0.62** **<0.001**	0.82	**0.73** **<0.001**	0.89	**0.69** **<0.001**	0.84	**0.50** **<0.001**	0.54

[a] Total particle (0.01 – 20.0 μm) number concentration measured by both SMPS and APS; [b] Coarse particle (0.5 – 20.0 μm) number concentration measured by APS; [c] Coarse particle (> 1.0 μm) number concentration measured by APS; [d] Total particle (0.5 – 30.0 μm in

555 optical size) number concentration measured by WIBS; [e] Number concentration of particles showing fluoresce in any one of WIBS fluorescent channels; [d] Number concentration of particles showing fluoresce in all three WIBS fluorescent channels; [g] Data not available

The concentration of INPs from North continental aerosols in PBL is between 2.2 and 71.6 std L^{-1}, showing a median of 14.1 std L^{-1} ($T = -26.7$ °C). When North continental aerosols serve as INP sources for (HAC)² above PBL, the observed INP

concentration decreases substantially (about tenfold). The results suggest that the INP concentration from a similar continental air mass depends on its relative position in the atmosphere and is consistent with published studies to date (e.g., Gong et al. (2022)). INPs in marine aerosols above the PBL range between 0.3 and 3.4 std L^{-1} (median 1.3 std L^{-1}) at $T = -25.5\,°C$, which is higher than the values reported in Lacher et al. (2021) from a source attributed to marine aerosols from western Mediterranean Sea. It is likely that the lower INPs (even at a lower experiment T) observed by Lacher et al. (2021) at Jungfraujoch in Switzerland are a result of longer transportation of marine aerosols, during which particle deposition and aging-induced deactivation may occur (Schrod et al., 2020). The dust plume after marine aerosols shows the highest INP concentration among all sources, showing an average of 121.3±14.7 std L^{-1} and a median of 121.1 std L^{-1} ($T = -23.9\,°C$, resampled for every 15 min due to short period of observations < 3 hours). Such a high INP concentration in Saharan dust was also observed at Jungfraujoch in Switzerland (>200 std L^{-1} for $T = -30\,°C$) (Brunner et al., 2021). Also, the observed INP concentration is substantially higher than ABC$_{WIBS}$ concentration (<10 std L^{-1} in **Error! Reference source not found.**f), suggesting that dust particles – but not any associated biological particles – make the primary contribution to the observed INPs in the dust plume. The median INP concentration decreases to 19.8 std L^{-1} ($T = -24.5\,°C$) when dust plume is more extensively mixed with local aerosols in the PBL, i.e., the source of South dust in PBL. Furthermore, the median INP concentration decreases further to 7.3 std L^{-1} ($T = -26.0\,°C$) when the dust plume is also mixed with continental aerosols, i.e., the source of South dust with North continental aerosols. It is likely that the source of South dust in PBL after marine aerosols may contain more fresh dust particles than the following sources having more aged and deactivated dust particles (Boose et al., 2019).

Among all sources presented in **Error! Reference source not found.**, INP concentration in the PBL is considerably larger than that in the FT by approximately more than one order of magnitude (median value), although it depends on INP sources. Both continental aerosols from the North and dust from the South are major sources for INPs at Mt. Helmos. Fresh dust plume contains a larger number of INPs than the other sources mixed with local emissions and/or continental aerosols. Such a decrease in INP abundance in the mixed dust containing sources may result from dilution of air masses or aerosol aging induced INP deactivation. Also, we note that the INP concentration range in North continental aerosols ($T = -26.7\,°C$) is analogous to that of South dust ($T = -24.5\,°C$) when both are mixed with local emissions in the PBL.

Error! Reference source not found. and Table 2 also provide the correlation between INP concentration and different concentrations of aerosol particles, including Total$_{SMPS+APS}$, Total$_{APS}$, Coarse$_{APS}$, Fluo$_{WIBS}$ and ABC$_{WIBS}$. The concentration of PINE INPs is approximately higher than 1 per 10^6 of Total$_{SMPS+APS}$, 1 per 10^3 of Total$_{APS}$ and 1 per 500 of Coarse$_{APS}$, respectively, consistent with the established view that INPs in the atmosphere show a size dependence and that larger-sized aerosol particles are of higher probability of behaving as INPs. Overall, a significant and positive correlation between INP concentration and aerosol particle concentrations can be found in **Error! Reference source not found.**. A ρ value larger than 0.80 for the relation between INPs and Total$_{APS}$, or Coarse$_{APS}$, or Fluo$_{WIBS}$ (>0.5 μm, optical size) means that INP concentration increases with those three particle concentrations following a strong monotonic trend. In comparison to Total$_{APS}$, Coarse$_{APS}$, Fluo$_{WIBS}$ (Figure 9) or Total$_{WIBS}$ (Fig. S7), the smaller R and ρ values for the relation between Total$_{SMPS+APS}$ and INPs also

indicates that small-sized aerosol particles in the SMPS size range may play a minor role for serving as INPs compared to larger-sized particles measured in the APS and WIBS size range. The IN dependence on the size of aerosol particles is more pronounced for the sources of North continental aerosols and South dust when both sources supply potential INPs for $(HAC)^2$ in the PBL, as shown that the R value between INPs and $Total_{APS}$ or $Coarse_{APS}$ for South dust in PBL does not show significant difference compared to the R value between INPs and $Total_{SMPS+APS}$ (Table 2). This is because the source of South dust in PBL contains a much smaller proportion of fine particles to the total than for the source of North continental aerosols in PBL (**Error! Reference source not found.**). Also, the ρ value of the relation between INPs and $Coarse_{APS}$ particles for North continental aerosols is larger than that of South dust in PBL, suggesting that INPs in North continental aerosols may be more dependent on coarse mode particles.

In addition to size dependence, we note that the observed INP concentration is close to the concentration of fluorescent particles, as shown that more than 80% of INP data points are within a factor of 5 compared to $Fluo_{WIBS}$ data (**Error! Reference source not found.**e). Also, INPs from most sources show a significant correlation with $Fluo_{WIBS}$ particles (except for the source of South dust in PBL after marine aerosols owing to limited number of observations). This suggests that particles showing fluorescence are of significant relevance for INPs observed at Mt. Helmos. The results are also in agreement with Mason et al. (2015) who reported that INPs observed between −15 and −25 °C at a coastal site are strongly correlated with fluorescent particles, and it is consistent with Pereira Freitas et al. (2023) who found fluorescent biological aerosol particles as dominant sources for INPs activating at T around −15°C. ABC_{WIBS} would constitute a subset of the observed total INPs, as the latter is approximately five times larger (**Error! Reference source not found.**f) and shows a significant correlation with ABC_{WIBS} particles in the source (Table 2). In particular, more than 90% observed INP data from sources of aerosols in the FT influenced by precipitation/clouds, marine aerosols and continental aerosols above the PBL, are within a range less than a factor of 5 compared with ABC_{WIBS} particles in the source (**Error! Reference source not found.**f). Such a close correlation highlights the importance of biological particles in those INP sources when dust particles are absent. Notably, the correlation between INPs and ABC_{WIBS} particles for aerosols in the FT influenced by precipitation/clouds becomes significant compared to the case without precipitation/clouds effects (Table 2), suggesting that precipitation/clouds may lead to an increase in ABC_{WIBS} (Figure 7) and contribute to observed INPs. Lastly, Table 2 shows that of all sources, ABC_{WIBS} particles from marine aerosols show the strongest correlation with INPs. This is consistent with the important role of marine biogenic aerosols in serving as INPs in the MPC regime (Wilson et al. (2015).

3.2.3 The ice nucleation ability of particles in different aerosol sources

Figure 10a uses the ratio of INP concentration to $Total_{SMPS+APS}$ concentration to estimate the INP proportion in total aerosol particles for different sources and uses the ratio as a measure to evaluate the average IN ability of aerosol particles from different sources. To clarify, we note that the ratio statistically refers to the overall ice formation ability of the particle population in the source. However, the ratio is not relevant to the IN ability of single particles which specifically relies on the physiochemical properties of the particle, given that sources containing low concentration of INPs may have effective INPs

activating at warm temperatures. When $(HAC)^2$ is in the FT under background condition without remotely transported air masses and without precipitation/clouds, the observed INP ratio is approximately one per million aerosol particles and the median ratio value is less than that reported in Rogers et al. (1998) who reported ~30 INPs out of a million particles at an altitude of 10.6 km in the upper troposphere and in a T range between −15 and −40 °C. Influenced by precipitation/clouds, the

630 INP ratio in the FT generally increases because of the decrease in total aerosol particles and the increase in INPs (Section 3.1 and 3.2.2). Figure 10a also suggests that $(HAC)^2$ position with respect to (*wrt.*) PBL regulates the average IN ability of particles from the North continental aerosol source, shown a larger INP ratio when the source is in the PBL than above the PBL. This is because active INPs from the source in the PBL may majorly come from Coarse$_{APS}$ particles which otherwise take a smaller proportion when the source is above the PBL (Figure 10b). The INP ratio of marine aerosols above PBL is analogous to that

635 of North continental aerosols above PBL (Figure 10a), suggesting a similar IN ability of particle populations in both aerosol sources. In addition, the INP ratio of aerosol sources containing dust particles decreases if the source is more influenced by the PBL or if it is mixed with North continental aerosols.
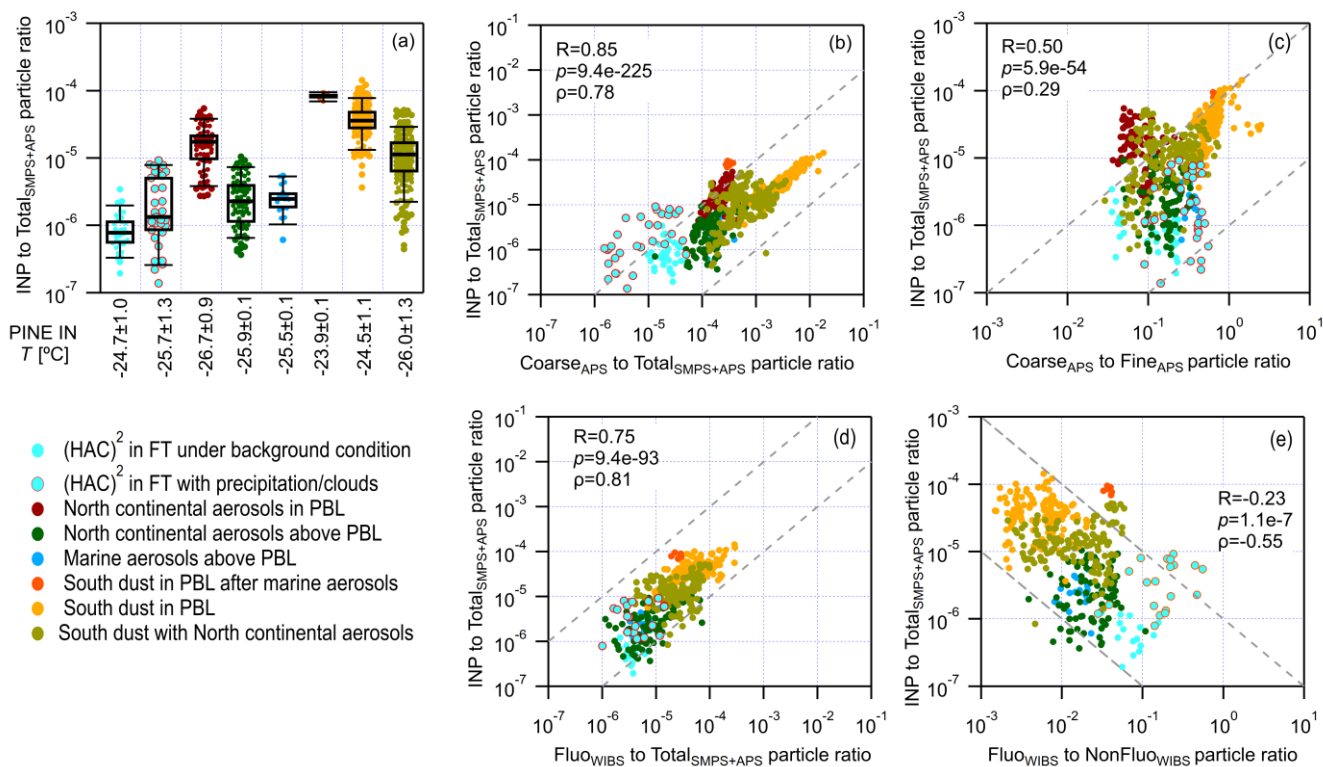

Figure 10. (a) Box plots for the ratio of INP concentration to Total$_{SMPS+APS}$ concentration. The average T for PINE IN experiments
640 for each INP source is indicated at the bottom axis and the uncertainty stands for one standard deviation. **(b)** Scatter plots of the ratio of INPs to Total$_{SMPS+APS}$ particles and the ratio of Coarse$_{APS}$ to Total$_{SMPS+APS}$ particles. **(c)** Scatter plots of the ratio of INPs to Total$_{SMPS+APS}$ particles and the ratio of Coarse$_{APS}$ to Fine$_{APS}$ particles. **(d)** Scatter plots the ratio of INPs to Total$_{SMPS+APS}$ particles and the ratio of Fluo$_{WIBS}$ to Total$_{SMPS+APS}$ particles. **(e)** Scatter plots of the ratio of INPs to Total$_{SMPS+APS}$ particles and the ratio of Fluo$_{WIBS}$ to NonFluo$_{WIBS}$ (the difference between Total$_{WIBS}$ and Fluo$_{WIBS}$) particles. The Pearson correlation coefficient (R) and
645 corresponding p value calculated from F-test, and Spearman's rank coefficient (ρ), are provided to evaluate the correlation between

INP abundance and the particle partitioning. The *P* value is the probability of obtaining an *R* value no smaller than the true *R* value if there is no liner correlation between INPs and the given parameter. The grey dashed lines in the panel confine a range of two magnitude on both *x*–axis and *y*–axis.

The results in Figure 10 also evaluate the dependence of INP ratio on the particle size and fluorescent property portioning condition of the source, including the ratio of $Coarse_{APS}$ to $Total_{SMPS+APS}$, $Coarse_{APS}$ to $Fine_{APS}$, $Fluo_{WIBS}$ to $Total_{SMPS+APS}$ and $Fluo_{WIBS}$ to $NonFluo_{WIBS}$ (the difference between $Total_{WIBS}$ and $Fluo_{WIBS}$). In general, the average INP ratio of a source increases with the increasing proportion of $Coarse_{APS}$ particles (> 1.0 μm, Figure 10b and c) and $Fluo_{WIBS}$ particles (Figure 10d and e) in the source, but such a correlation varies its strength among individual sources. Figure 10b shows that the INP ratio of North continental aerosols (for both above and in the PBL) has a weaker correlation with $Coarse_{APS}$ particles (see *R* and ρ values in Table S1 in Supplement S5) compared to that of South dust in PBL. Again, this is because North continental aerosols contain more fine mode particles, which are less effective INPs, than aerosols from South dust in PBL. A larger slope for North continental aerosols in Figure 10b compared to South dust in PBL suggests that INPs in North continental aerosols are more dependent and sensitive to $Coarse_{APS}$ particles. This may be because individual $Coarse_{APS}$ particles in continental aerosols of biological origin are generally more effective INPs than those in dusty aerosols. This can be true if those coarse mode particles in continental aerosols are of a biologic origin. Moreover, the insignificant correlation between the INP ratio of sources containing North continental aerosols and the ratio of $Coarse_{APS}$ to $Fine_{APS}$ in the source (Figure 10c and also Table S1 in Supplement S5) suggests that some particles smaller than the APS size detection range (~0.5 μm) may contribute to the observed INPs at ~ −26 °C. Figure 10c shows that the correlation between INP ratio and $Coarse_{APS}$ to $Fine_{APS}$ ratio is less significant (see Table S1) for the source of South dust in PBL compared to the correlation between INP ratio and $Coarse_{APS}$ to $Total_{SMPS+APS}$ ratio, also suggesting a contribution of some small-sized particles (<0.5 μm) to observed INPs. This is consistent with a field study in Israel (in the Eastern Mediterranean region) focusing on the IN ability of size-resolved Saharan dust particles and the study reported that 0.3 μm (aerodynamic diameter) dust particles are effective INPs at the *T* range from −20 °C to −30 °C (Reicher et al., 2019). In addition, the increasing $Fluo_{WIBS}$ to $Total_{SMPS+APS}$ ratio can generally predict the increasing INP ratio of an aerosol source (Figure 10d, no data available for the source of North continental aerosols). However, Figure 10e shows that the INP ratio in different aerosol sources overall decreases with increasing $Fluo_{WIBS}$ to $NonFluo_{WIBS}$ ratio. The results on the *x*-axis of Figure 10e show that the $Fluo_{WIBS}$ to $NonFluo_{WIBS}$ ratios in different sources are in reverse order compared to the other ratios presented in Figure 10b, c and d. Such a difference suggests the INPs that are of a biological origin become less important when the overall IN ability and INP abundance of the source is higher, such as dust plumes, indicating a less pronounced role of biological particles in dust-containing sources in serving as INPs.

Overall, the scatter patterns of INP ratio versus different aerosol partitioning index presented in Figure 10 spread over two orders of magnitude (confined by grey dashed lines in Figure 10b, c, d and e). Both $Coarse_{APS}$ to $Fine_{APS}$ ratio and $Fluo_{WIBS}$ to $NonFluo_{WIBS}$ ratio show significant correlations (*p*<0.05 in Table S1) with the ratio of INP to $Total_{SMPS+APS}$ (Figure 10c and e), although the strengths of these two correlations are weaker compared to the results using $Total_{SMPS+APS}$ data in Figure 10b and d. This suggests the proportion of particles with different sizes and fluorescent properties conveys the IN ability of particles

680   from different aerosol sources, which may benefit the prediction of INPs in parameterizations. In Section 3.4, these ratios will be incorporated into INP parameterizations to improve their prediction skill.

3.3 The influence of precipitation/clouds on INPs in PBL

3.3.1 Different scenarios classified during the case study

In addition to the effects of precipitation/clouds on INPs for periods of $(HAC)^2$ in the FT, precipitation/clouds periods were
685   also observed when the site resided in the PBL – with different aerosol sources however, so we treat them separately. For this, we focus on a case study (November 23) where the $(HAC)^2$ is in the PBL and influenced by continental aerosols. The FLEXPART footprints and the HYSPLIT back trajectories (Figs. S9 and S10, respectively) suggest that North continental airmass dominates the aerosol source at $(HAC)^2$ during this time (with a possible minor contribution of South dust). The dominance of North continental aerosols is also supported by nephelometer results, as $\alpha \sim 2.0$ (Mordas et al., 2015). Following
690   the methodology introduced in Section 2.4, the observations during the day are classified based on the presence of precipitation/clouds and the position of $(HAC)^2$ *wrt.* PBL, by using Ze and MDV values from radar measurements presented in Figure 11a and b, respectively. The position of $(HAC)^2$ *wrt.* PBL is evaluated by using SMPS $N_{>95nm}$ time series in Figure 11c since PBLH results from lidar are not always available during the day. Thus, observations on November 23 are classified into five periods ("cases"), including $(HAC)^2$ in FT with precipitation (case 1) from 00:00 to 04:00, $(HAC)^2$ in FT with
695   precipitation (case 2) from 05:00 to 09:00, $(HAC)^2$ around PBL and close to the cloud top (case 3) from 10:00 to 15:00, $(HAC)^2$ in PBL (case 4) from 15:30 to 18:00, and $(HAC)^2$ in PBL with precipitation/clouds (basically precipitation below $(HAC)^2$, case 5) from 19:00 to 24:00. The box plots of INP abundance observed by PINE and the correlation between INPs and aerosol particles of different cases are presented in **Error! Reference source not found.**. Additionally, the aerosol property results, including particle size distribution of different cases (Fig. S11), $Total_{SMPS+APS}$, $Coarse_{APS}$, SMPS $N_{<95\ nm}$, $Fluo_{WIBS}$ and ABC_{WIBS}
700   particle concentration, and eBC mass concentration (Fig. S12), are provided in the Supplement and used to understand the changing INP abundances of different scenarios presented in this section.

3.3.2 Particle properties

The aerosol particle properties for each case are shown in Figure 11c, d and e, and Figs. S11 to S13. Figure 11c shows that PBL boundary generally evolves from a position below $(HAC)^2$ to a position above $(HAC)^2$ throughout the day, as SMPS
705      $N_{>95nm}$ increases. The increasing PBLH is also indicated by size distribution shifts to coarse-sized particles in Fig. S11 during the day. When $(HAC)^2$ is in the FT with precipitation (case 1), $Coarse_{APS}$ particles at $(HAC)^2$ show a median of $\sim$1.5 std L^{-1} (Fig. S12b). The median value is well below the critical value of 20 std L^{-1} (see Section 2.4), suggesting that the site at this time is exposed to clean background conditions with a low probability of influence from remotely-transported aerosols above the PBL. This is also supported by the low eBC mass concentration ($\sim$0.01 µg std m^{-3}) shown in Fig. S12f.

28

710   When $(HAC)^2$ is in the FT with precipitation (case 2), $Coarse_{APS}$ particles at $(HAC)^2$ are occasionally larger than 20 std L^{-1} and show a median of ~16.7 std L^{-1} (Fig. S12b). Likely, it suggests that remotely transported continental aerosols exert an influence on aerosols at $(HAC)^2$, although $(HAC)^2$ is still above PBL with SMPS $N_{>95nm}$ smaller than 100 std cm^{-3}. Also, it is possible that precipitation from higher altitude clouds compared to case 1 results in downdrafts that drive mass entrainment of remotely transported aerosols. Furthermore, compared to case 1, the decreased ABC_{WIBS} particles in case 2 suggests negligible

715   biological particles in downdrafts from high altitudes (Fig. S12e) whereas the increased eBC mass concentration is a result of transportation (Fig. S12f). Additionally, the comparison between case 1 and 2 suggests that $Coarse_{APS}$ particle concentration less than 20 std L^{-1} is a more conservative evaluation standard to diagnose $(HAC)^2$ inside the FT compared to the criterion of SMPS $N_{>95nm}$ less than 100 std cm^{-3} (also see Section 2.4). In addition to the differences between the vertical particle sources for case 1 and case 2, we note that the average wind speed decreases from ~13 m s^{-1} (case 1) to 6 m s^{-1} (case 2) (not shown),

720   which would decrease the emission rate of ABC_{WIBS} particles from the near-ground sources, such as soils and trees.
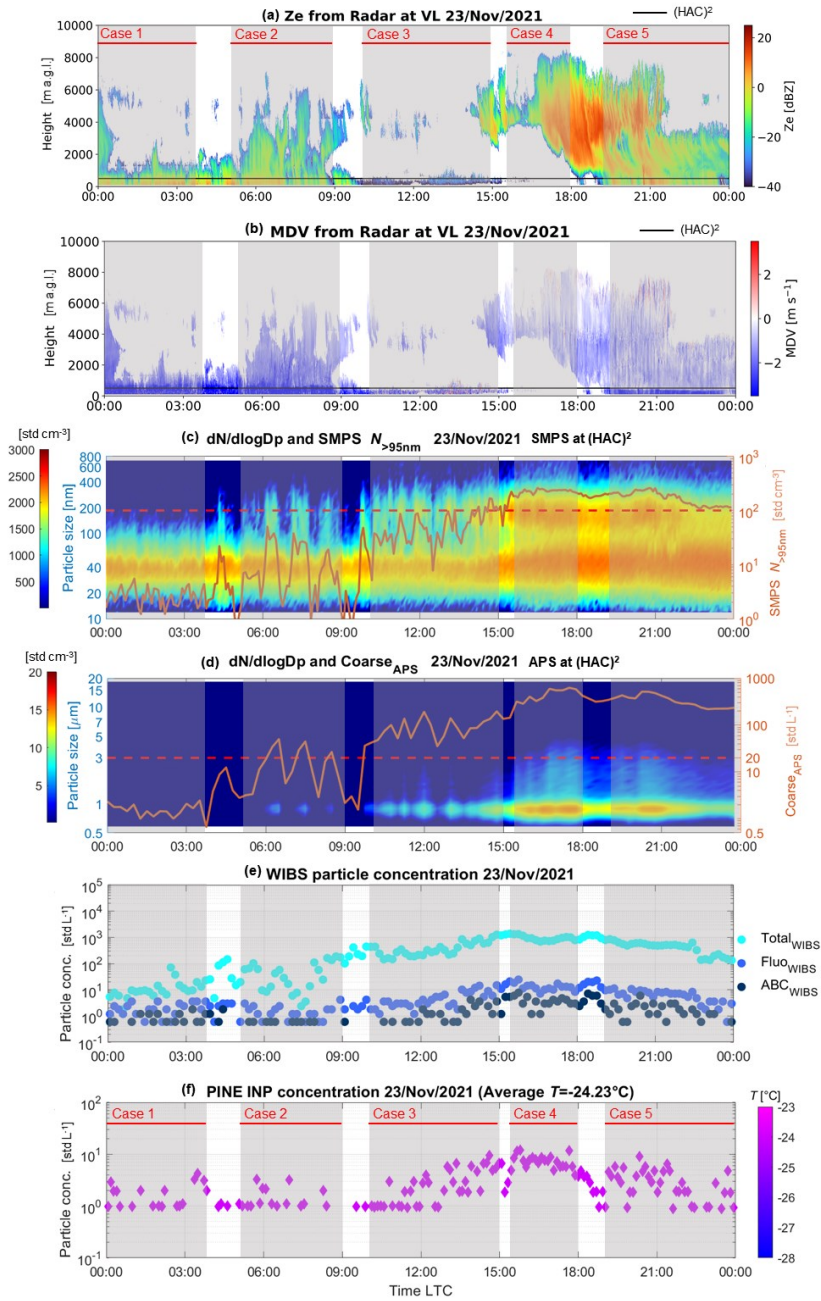
Figure 11. Timeseries of precipitation condition, aerosol particle and INP concentration on November 23, 2021. (a) and (b) Ze and MDV measured by the radar at VL, respectively. The (HAC)^2 level is indicated by the black line in the panel. (c) Particle size distribution measured by SMPS at (HAC)^2 for particles smaller than 800 nm (mobility diameter) and number concentration of SMPS $N_{>95nm}$ particles used to evaluate (HAC)^2 position with respect to PBL. The left axis shows the size for particle size distribution colour map and the right axis scales SMPS $N_{>95nm}$ values. (d) Particle size distribution measured by APS at (HAC)^2 for particles having a size between 0.5 and 20 µm (aerodynamic diameter) and number concentration Coarse$_{APS}$ particles (> 1.0 µm). The left axis shows the size for particle size distribution colour map and the right axis scales Coarse$_{APS}$ values. (e) Total$_{WIBS}$, Fluo$_{WIBS}$ and

ABC$_{WIBS}$ particle number concentrations recorded by WIBS at the (HAC)^2. (f) PINE INP concentration measured at (HAC)^2 with time resolution of ~6 min. The temperature for PINE IN experiments is indicated by the marker colour scaled to the colour bar.

When (HAC)^2 is around PBL and close to the cloud top (case 3), Coarse$_{APS}$ particle concentration increases to a level larger than 20 std L^{-1} (Fig. S12b) because of increased influence from PBL aerosols. The adoption of aerosols from the PBL is supported by the occasional updrafts shown in Figure 11b and by the increasing SMPS $N_{>95nm}$ close to 100 std cm^{-3}. For the two scenarios of (HAC)^2 in PBL with and without precipitation/clouds (case 4 and 5 respectively), Coarse$_{APS}$ particle concentration is well above 20 std L^{-1}. The presence of precipitation/clouds leads to a decrease in Coarse$_{APS}$ particle concentration, showing a decreased median value from 414.1 to 330.2 std L^{-1} (Fig. S12b). This suggests the wet removal effects of precipitation on coarse mode particles in the PBL. However, the presence of precipitation/clouds causes an increase in SMPS $N_{<95nm}$ particles (Figs. S11, Figure 11c and S12c), suggesting that the effect of precipitation/clouds in PBL may also include new particle formation (Khadir et al., 2023).

In general, it can be summarized that Coarse$_{APS}$ particle concentration increases when (HAC)^2 is deeper inside the PBL (indicated by a larger SMPS $N_{>95nm}$; Fig. S12b), suggesting that the PBL is the major source for aerosol particles at (HAC)^2 on November 23. With increased influences from the PBL, the increases in both ABC$_{WIBS}$ and eBC particles (Fig. S12e and f) suggest that ABC$_{WIBS}$ particles are related to biological particles and eBC emissions are mainly from the PBL. However, the occurrence of precipitation/clouds in the PBL leads to decreased ABC$_{WIBS}$ particles, which is opposite to the effect on aerosols in the FT (see Section 3.1.2). This may result from the wet removal effects of precipitation/clouds on ABC$_{WIBS}$ particles which may dominate over any production of ABC$_{WIBS}$ from precipitation splash (Khadir et al., 2023). The occurrence of precipitation/clouds in the PBL results in a small decrease in eBC mass (Fig. S12f), from 0.07 µg std m^{-3} to 0.05 µg std m^{-3} (median), suggesting a slight wet deposition of eBC particles during the precipitation/clouds periods.

3.3.3 INPs observed under different scenarios

INP concentration for (HAC)^2 in FT with precipitation (case 1) in **Error! Reference source not found.**a shows a median value of 1.0 std L^{-1}, consistent with **Error! Reference source not found.**a for the case of (HAC)^2 in FT with precipitation/clouds sampled from the other similar periods during CALISHTO. Compared to case 1 (**Error! Reference source not found.**a), case 2 shows a slightly lower INP concentration (median value 0.6 std L^{-1}), attributed to the decreased availability of Fluo$_{WIBS}$ and ABC$_{WIBS}$ particles (Figure 11e, S12d and S12e). The results also show that Fluo$_{WIBS}$ and ABC$_{WIBS}$ particles are more important sources of potential INPs than Coarse$_{APS}$, given that a tenfold increase in Coarse$_{APS}$ particles does not lead to an increase in INPs for case 2.

When (HAC)^2 is around the PBL and close to cloud top (case 3), it shows an increase in INPs compared to both case 1 and case 2 when (HAC)^2 is in the FT. The increased INPs may be attributed to the increased availability of Fluo$_{WIBS}$ and ABC$_{WIBS}$ particles, probably Coarse$_{APS}$ particles as well. When the (HAC)^2 is in the PBL (case 4), the INP concentration reaches a peak during the day with a median of 7.2 std L^{-1}. A short period of cloudiness around (HAC)^2 after 18:00 and the presence of precipitation/clouds at the (HAC)^2 (in the PBL) around 19:00 lead to a decrease in INPs (Figure 11), likely because of the wet

removal effects on aerosols particles. This is different from the results presented in **Error! Reference source not found.**a showing enriched INPs after a period of precipitation/clouds. The different INP changes caused by precipitation in the FT and in the PBL can be attributed to the corresponding increase and decrease in ABC$_{WIBS}$ particles in the FT (**Error! Reference**

765   **source not found.**f) and in the PBL (Fig. S12e) respectively, highlighting the importance of ABC$_{WIBS}$ particles in regulating INP abundance under different atmospheric conditions. When (HAC)^2 is in the FT (Figure 9a) where background INPs are rare, ABC$_{WIBS}$ particles produced by precipitation may easily play a pronounced role in influencing INP concentrations. In this case, ABC$_{WIBS}$ particles may come from cloud-processed particles released from hydrometeors in the precipitation/clouds (Prenni et al., 2013), biological particles or soil dust containing biological components produced by precipitation upon hitting

770   the vegetated or soil surface (Conen et al., 2011; Conen et al., 2017). Differently, precipitation/clouds enriched INPs take a small proportion in the total INPs when (HAC)^2 is in the PBL (Figure 12). Instead, the wet removal effect of precipitation/clouds for (HAC)^2 in the PBL may play the major role and remove some ABC$_{WIBS}$ particles in coarse mode that might be active INPs. Therefore, the overall effect of precipitation/clouds on INPs observed at (HAC)^2 for temperatures around −24.2°C (Figure 11f) shows a decrease when (HAC)^2 lies within the PBL.
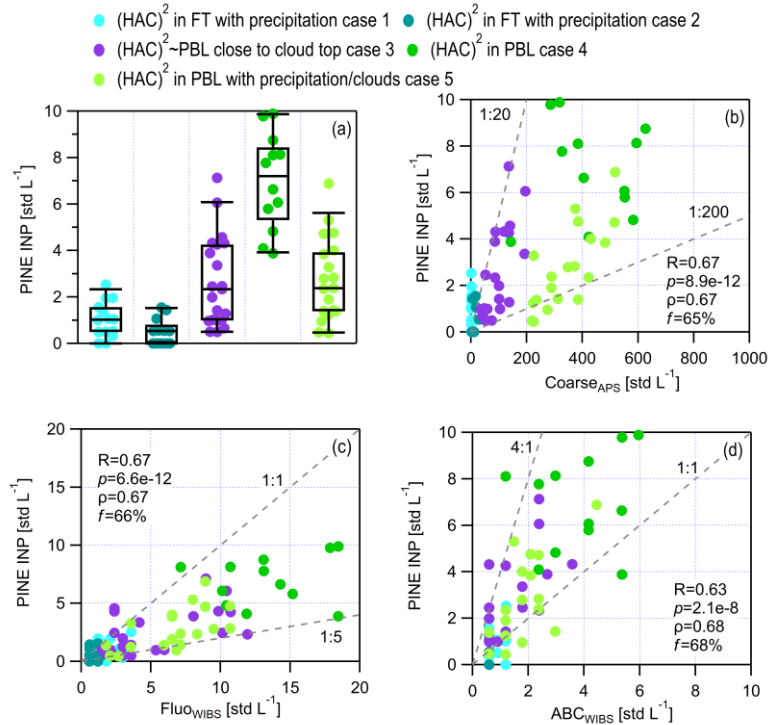

775

Figure 12. INP concentration and the relation between INPs and aerosol particles under different scenarios. (a) Box plots of PINE INP abundance of different scenarios classified on November 23. (b) Scatter plots for PINE INP and Coarse$_{APS}$ particle concentration. (c) Scatter plots for PINE INP and Fluo$_{WIBS}$ particle concentration. (d) Scatter plots for PINE INP and ABC$_{WIBS}$ particle concentration. The Pearson correlation coefficient (R) and corresponding p value calculated from F–test, and Spearman's

780   **rank coefficient (ρ), are provided to evaluate the correlation between INP abundance and the particle partitioning. The P value is the probability of obtaining an R value no smaller than the true R value if there is no liner correlation between INPs and the given parameter. The value of f means the percentage of data points within the range confined by dashed lines in the panel.**

Error! Reference source not found. also shows that the INP concentration observed at $(HAC)^2$ on November 23 generally has a significantly positive correlation with Coarse$_{APS}$, Fluo$_{WIBS}$ and ABC$_{WIBS}$ particle concentration. The concentration of Coarse$_{APS}$ particles is generally higher than that of INPs by > 20 times (> 65% in **Error! Reference source not found.**b). Also, 66% INP concentration values are lower than those of Fluo$_{WIBS}$ (**Error! Reference source not found.**c) whereas 68% INP concentration values are larger than those of ABC$_{WIBS}$ (**Error! Reference source not found.**d). The results mean that INPs are from coarse particles (> 1.0 μm) showing fluorescence whereas ABC$_{WIBS}$ particles are not the only source for INPs.
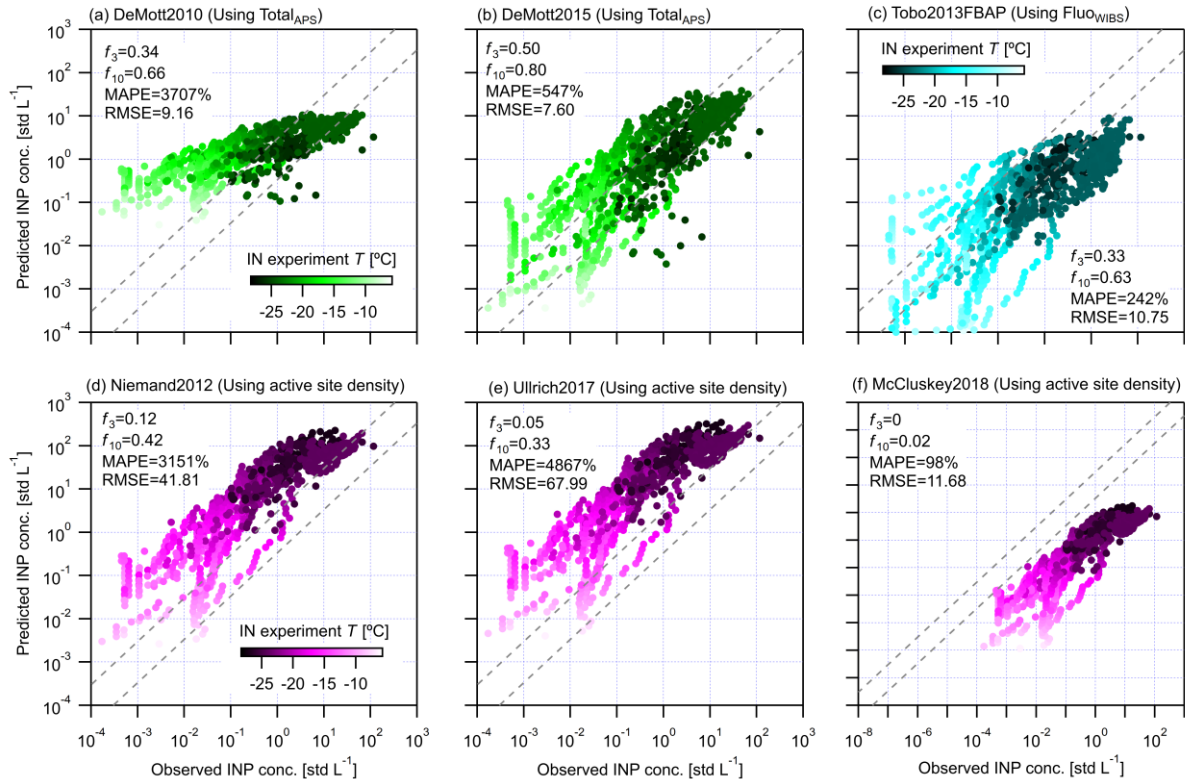
Figure 13. Scatter plots of observed INP concentration and the concentration calculated by parameterizations (in Table 1) from the literature. Parameterizations in panel (g) to (i) are based on the overlapped WIBS, APS and SMPS dataset. (a) DeMott2010. (b) DeMott2015. (c) Tobo2013FBAP. Here, Fluo$_{WIBS}$ is used to substitute n_{FABPS} measured by UV-APS as used in Tobo et al. (2013). (d) Niemand2012. (e) Ullrich2017. (f) McCluskey2018. The temperature condition for INP data is scaled to the colour bar. Parameterizations using the same aerosol properties use the same colour bar. The dashed lines confine the range for observed and predicted data points within a factor of 3. The fractions of observed and predicted data points within a factor of 3 (f_3) and 10 (f_{10}) are provided in each panel, respectively. MAPE stands for Mean absolute percentage error. RMSE is the root-mean-square error used as a measure of the difference between observed and predicted data.

3.4 INP parameterization

3.4.1 Predicting INPs observed at Mt. Helmos using published parameterizations

A variety of parameterizations, summarized in Table 1, have been proposed to estimate N_{INP} using aerosol properties, such as particle number concentration and particle surface area. We evaluate their ability to reproduce the observed N_{INP} at Mt. Helmos.

33

Here, we note that Fluo$_{\text{WIBS}}$ is used to substitute n_{FBAPS} (the number concentration of fluorescent aerosol particles monitored by an UV-APS) used in Tobo et al. (2013). The predictability of those parameterizations is evaluated by comparing N_{INP} observations to the calculated N_{INP} results. The evaluation of the predictability of each INP parameterization (in Table 1) for
805   INPs from different INP sources discussed in Section 2.4 is presented in Figs. S14 to S19. In addition, we note that INSEKT INPs evaluated as lower estimations beyond a factor of 5 by comparing to PINE INPs (see Supplement S3) are excluded from the parameterization dataset. The overall consistent trend between INSEKT and PINE data clusters in Figure 13 and Figure 14 for all INP parameterizations suggests that filtered INSEKT dataset does not show discrepancy compared to PINE dataset and not influence the INP parameterization development.

810   **Table 3. Different parameterizations proposed for predicting INPs at Mt. Helmos.**

INP Parameterizations	Used aerosol property	Formulation
Helmos DeMott2015	Total$_{\text{APS}}$ (std cm^{-3})	$N_{INP} = cf * Total_{APS}^{(-aT+b)} * exp\,(-cT + d)$ ($cf = 3$, a = 0.09, b = −1.05, c = 0.49, d = −12.66; T in °C)
Helmos Total$_{\text{APS}}$		$N_{INP} = a(-T)^b * (Total_{APS}/1000)^{(-cT+d)} * (APS_{ratio} * (eT + f))$ (a = 900, b = −9.56, c = 0.14562, d = −2.769, e = −32000000, f = 860000)
Helmos Tobo2013FBAP	Fluo$_{\text{WIBS}}$ (std cm^{-3})	$N_{INP} = Fluo_{WIBS}^{(-aT+b)} * exp\,(-cT + d)$ (a = 0.096, b = −1.49, c = 0.96, d = −18.9; T in °C)
Helmos Fluo$_{\text{WIBS}}$		$N_{INP} = exp(aT + b) * (Fluo_{WIBS}/1000)^{(cT+d)} * (WIBS_{ratio})^{(eT+f)}$ (a = −0.096725, b = −3.6932, c = −0.16288, d = −3.04 e = 0.024358, f = 0.44052; T in °C)
Helmos Total$_{\text{WIBS}}$_1	Total$_{\text{WIBS}}$ (std L^{-1})	$N_{INP} = exp(aT + b) * Total_{WIBS}^{(cT+d)} * (WIBS_{ratio} * e + f)$ (a = 0.45678, b = −3.456, c = −0.15, d = −2.7989, e = 220000, f = 18400; T in °C)
Helmos Total$_{\text{WIBS}}$_2		$N_{INP} = a(-T)^b * Total_{WIBS}^{(cT+d)} * (\dfrac{1}{WIBS_{ratio} * e + f})$ (a = −4244444.44, b = −5.5, c = −0.119, d = −1.69, e = 641.55, f = −154.31; T in °C)
Helmos Total$_{\text{SMPS+APS}}$_1	Total$_{\text{SMPS+APS}}$ (std cm^{-3})	$N_{INP} = cf * Total_{SMPS+APS}^{(-aT+b)} * exp\,(-cT + d)$ (cf = 1e−5, a = 0.04, b = −0.19, c = 0.2, d = 2; T in °C)
Helmos Total$_{\text{SMPS+APS}}$_2		$N_{INP} = a(-T)^b * Total_{APS}^{(-cT+d)} * (SMPS\_APS_{ratio} * (eT + f))$ (a = 9000000, b = −10.3, c = 0.16, d = −2.769, e = −3200000, f = 800; T in °C)
Helmos S$_{\text{SMPS+APS}}$	S$_{\text{SMPS+APS}}$ (std m^2 cm^{-3})	$N_{INP} = 1000 * S_{SMPS+APS} * exp\,(aT + b)$ (a = −0.5, b = 6.6; T in °C)

Note. APS$_{\text{ratio}}$ means the ratio of Coarse$_{\text{APS}}$ to Fine$_{\text{APS}}$ particle concentration. WIBS$_{\text{ratio}}$ means the ratio of Fluo$_{\text{WIBS}}$ to NonFluo$_{\text{WIBS}}$ particle concentration. SMPS_APS$_{\text{ratio}}$ means the ratio of Coarse$_{\text{APS}}$ to Fine$_{\text{SMPS+APS}}$ particle concentration

DeMott2015 can predict 80% data points within a factor of 10 compared to observations (Figure 13b), which is better than DeMott2010 (66%, in Figure 13a). Generally, overestimated INP data points by DeMott2015 are more than those
815   underestimated (Figure 13b). For Tobo2013FBAP, we first note that Fluo$_{\text{WIBS}}$ particle concentration used in this study is larger than the fluorescent particle concentration measured by UV-APS as used in Tobo et al. (2013). Such an input difference would have led to an overprediction in INPs, if data from the Mt. Helmos were similar to those observed in Tobo et al. (2013). We find however, that Tobo2013FBAP generally underestimates INPs at Mt. Helmos, especially for temperatures lower than −20

°C when dust particles dominate the INP sources (Fig. S16h and i). This discrepancy may be explained when considering that Tobo2013FBAP is developed based on an INP population of biological particles that activate as ice at warm temperatures (> −15 °C). Given that the abundance of biological particles is lower than that of dust particles, thus, Tobo2013FBAP underestimates INPs originated from dust particles activating ice at lower temperatures. Nevertheless, Tobo2013FBAP is able to agree with 63% of INP observations in Mt. Helmos within two orders of magnitude (Figure 13c).

The results in Figure 13d to 13f are based on the subset of data when both SMPS and APS data (hereafter $INP_{SMPS+APS}$ data) are available. Both Niemand2012 and Ullrich2017 systematically overestimate $INP_{SMPS+APS}$ (Figure 13d and 13e), which may be attributed to the data base used for the development of both parameterizations (dust samples tested in laboratory studies), which may have exhibited a larger active site density compared to the atmospheric particles investigated in this study. On the contrary, McCluskey2018 systematically underestimates the observed $INP_{SMPS+APS}$ data (Figure 13f), likely because it is based on sea spray aerosol, which may have a lower active site density compared to INPs observed in this study.

Of all literature parameterizations tested, DeMott2015 is the best to predict INPs at Mt. Helmos. Its comparatively good performance can be attributed to its larger and more inclusive data base from both laboratory and field experiments. DeMott2015 will therefore be adapted in Section 3.4.2 to optimize its applicability for Mt. Helmos by proposing new parameters.

3.4.2 Parameterizations for INPs using the CALISHTO data

Nine parameterizations using different aerosol properties are developed (**Error! Reference source not found.**), including parameterizations adapted from the literature and proposed ones depending on the observed relations between INPs and aerosol properties. We first adapt the DeMott2015, named "Helmos DeMott2015", with a new set of parameters calculated by fitting the formula to the relevant data collected at Mt. Helmos. Considering that the IN ability of aerosol sources show a significant correlation with $Coarse_{APS}$ to $Fine_{APS}$ ratio (Figure 10c), thus the ratio, termed APS_{ratio} hereafter, is included in a new INP parameterization termed "Helmos $Total_{APS}$". We also adapt Tobo2013FBAP with new parameters and it will be compared to a new parameterization we develop, termed "Helmos $Fluo_{WIBS}$" that predicts INP as a function of $Fluo_{WIBS}$, $WIBS_{ratio}$ ($Fluo_{WIBS}$ to $NonFluo_{WIBS}$) and T. Compared to Tobo2013FBAP, the new factor "$(WIBS_{ratio})^{(eT+f)}$" in "Helmos $Fluo_{WIBS}$" is used to capture the contribution of fluorescent particles to the observed INPs at different temperatures. Given that $Fluo_{WIBS}$ may not include all potential INPs (especially for $T < -20$ °C where nonbiological particles dominate), we propose two parameterizations ("Helmos $Total_{WIBS}$_1" and "Helmos $Total_{WIBS}$_2") using $Total_{WIBS}$ to represent aerosol particles that may serve sources for INPs. Both parameterizations depend on $Total_{WIBS}$, $WIBS_{ratio}$ and T but with different formula forms. Compared to DeMott2015 and DeMott2010, "Helmos $Total_{WIBS}$_1" and "Helmos $Total_{WIBS}$_2" also consider the effect of fluorescent particle portioning in different INP sources by using the corresponding factor including "$WIBS_{ratio}$". Moreover, $Total_{SMPS+APS}$ is used as the input for INP source particles to calculate N_{INP} to include potentials in a larger size range, given that particles smaller than 0.5 μm may also be relevant for INPs (Kanji et al., 2017). With and without including the ratio of $Coarse_{APS}$ to $Fine_{SMPS+APS}$ particles ($SMPS\_APS_{Ratio}$), two parameterizations ("Helmos $Total_{SMPS+APS}$_1" and "Helmos

Total$_{\text{SMPS+APS}}$_2" using a similar formula to that of DeMott2015 and DeMott2010 respectively) are proposed to calculate N_{INP} based on Total$_{\text{SMPS+APS}}$ and T. We also provide parameters for a surface-area based parameterization ("Helmos S$_{\text{SMPS+APS}}$") using the concept of surface-active sites. In the following, we discuss the performance of INP parameterizations introduced above (Figure 14) and evaluate the predictability of each INP parameterization (Figs. S20 to S35) for INPs from different INP sources discussed in Section 2.4.

INP parameterizations using Total$_{APS}$ particle concentration. The results in Figure 14a and b compare the predictability of Helmos DeMott2015 and Helmos Total$_{APS}$. After adaption, the percentage of N_{INP} data points within two orders of magnitude
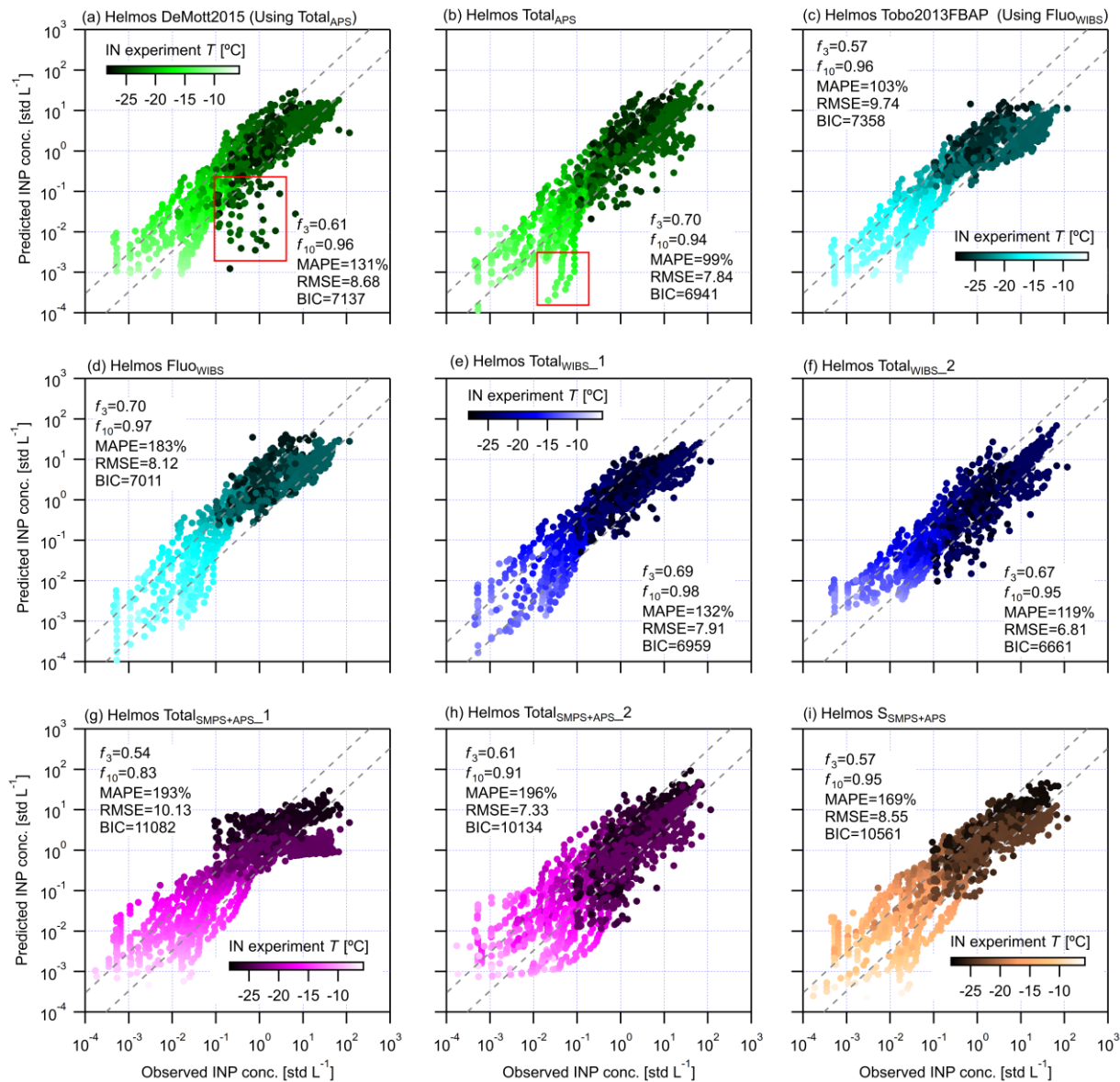
Figure 14. Different parameterizations for predicting INPs at (HAC)². Parameterizations in panel (a) to (f) are based on the dataset when both APS and WIBS are available. Parameterizations in panel (g) to (i) are based on the overlapped APS and WIBS dataset. (a) Helmos DeMott2015. (b) Helmos Total_APS. (c) Helmos Tobo2013FBAP. (d) Helmos Fluo_WIBS. (e) Helmos Total_WIBS_1. (f) Helmos Total_WIBS_2. (g) Helmos Total_SMPS+APS_1. (h) Helmos Total_SMPS+APS_2. (i) Helmos S_SMPS+APS. The temperature condition for INP data is scaled to the colour bar. Note that parameterizations using the same aerosol properties use the same colour bar. The dashed lines confine the range for observed and predicted data points within a factor of 3. The fraction of observed and predicted data points within a factor of 3 (f_3) and 10 (f_{10}) is provided in each panel, respectively. MAPE stands for mean absolute percentage error. RMSE is the root-mean-square error used as a measure of the difference between observed and predicted data. BIC is a value calculated by applying the Bayesian information criteria to evaluate the goodness of parameterizations based on the same dataset (Schwarz, 1978).

37

in Figure 14a). Also, ~11% of the 16% comes from the predictions on N_{INP} values within a factor of 3 compared to the observation. However, Helmos DeMott2015 does not show improvements in predicting INPs for aerosol sources in the FT, as indicated by the underestimated values in the red square in Figure 14a (also Fig. S20b and c). In particular, as shown in Fig. S20c, only 41% predictions from Helmos DeMott2015 are within a factor of 10 compared to the observations when $(HAC)^2$ is in the FT with influences of precipitation/clouds. Figure 14b shows that the consideration of APS_{ratio} into Helmos $Total_{APS}$ parameterization can improve its predictability by increasing the f_3 from 0.61 to 0.70, compared to Helmos DeMott2015. Also, the lower mean absolute percentage error (MAPE), root-mean-square error (RMSE) and Bayesian information criteria (BIC) values of Helmos $Total_{APS}$ suggest its slightly better performance than Helmos DeMott2015, by showing a smaller deviation, a smaller overall error and a larger formula fitting goodness, respectively. However, Helmos $Total_{APS}$ cannot predict INPs within the f_{10} range at warm temperatures (> -20 °C) probably for biological particles from continental aerosols (Garcia et al., 2012; Pummer et al., 2015), as marked by the red square in Figure 14b. Those data points are from two INSEKT filter samples collected on October 28 and 29 when $(HAC)^2$ is affected by continental aerosols (Fig. S21i).

INP parameterizations using Fluo$_{WIBS}$ particle concentration. With a new set of parameters, Helmos Tobo2013FABP in Figure 14c shows improved predictability for N_{INP}, showing increased f_3 and f_{10} by 0.24 and 0.33 respectively, in comparison to Tobo2013FABP in Figure 13c. This suggests INP populations observed at Mt. Helmos might have different IN abilities from those observed in Tobo et al. (2013). After incorporating $WIBS_{ratio}$ into Helmos Fluo$_{WIBS}$, the parameterization can further increase the f_3 predictability to 0.70 (Figure 14d) compared to Helmos Tobo2013FABP. Also, Helmos Fluo$_{WIBS}$ shows lower RMSE and BIC values, suggesting a slightly better fitting goodness. On the other hand, Helmos Fluo$_{WIBS}$ shows a larger MAPE value, which is due to its more scattered predictions on INPs at warm temperatures (> -20 °C).

INP parameterizations using Total$_{WIBS}$ particle concentration. Helmos Total$_{WIBS}$_1 and Total$_{WIBS}$_2 show comparable f_3 and f_{10} predictions larger than 0.67 and 0.95 respectively (Figure 14e and f). Compared to Helmos Total$_{WIBS}$_1, Helmos Total$_{WIBS}$_2 shows smaller values of MAPE and RMSE, suggesting an overall slightly smaller deviation of N_{INP} predictions. Except for INPs from the source of South dust in PBL after marine aerosols, Helmos Total$_{WIBS}$_1 can predict N_{INP} from the other sources with a f_{10} larger than 97% (Fig. S24). The exceptional performance for the source of South dust in PBL after marine aerosols may be due to the limited observations, for which other parameterizations show similar results (see results in Supplement S9). Compared to Helmos Total$_{WIBS}$_1, the slightly overall lower f_3 and f_{10} predictability of Helmos Total$_{WIBS}$_2 is because of its relatively poor predictions for INPs from the source of aerosols in the FT with precipitation/clouds (Fig. S25c).

INP parameterizations using Total$_{SMPS+APS}$ particle concentration. Figure 14g shows a f_3 and f_{10} prediction of 0.54 and 0.83 respectively for Helmos Total$_{SMPS+APS}$_1. Its N_{INP} prediction skill is the lowest amongst parameterizations shown in Figure 14, possibly due to its poor ability to predict dust INPs (Fig. S26h). Compared to Helmos Total$_{SMPS+APS}$_1, the inclusion of $SMPS\_APS_{Ratio}$ into Helmos Total$_{SMPS+APS}$_2 helps the parameterization to capture INPs from different particle populations and increases the f_{10} prediction by 7% (Figure 14h). Predictions from Helmos Total$_{SMPS+APS}$_2 also show a more symmetric distribution around the 1:1 line. However, Helmos Total$_{SMPS+APS}$_2 shows a decreased predictability for INPs from the source

of aerosols in the FT with precipitation/clouds (f_3=0.10 and f_{10}=0.48 in Fig. S27c) compared to Helmos Total$_{SMPS+APS}$_1 (f_3=0.86 and f_{10}=1.0 in Fig. S26c).

INP parameterizations using $S_{SMPS+APS}$ total particle surface area. The parameterization, based on active site density (Young, 1974; Demott, 1994; Connolly et al., 2009), is expressed as a function of T and the particle surface area ($S_{SMPS+APS}$). Compared to Niemand2012, Ullrich2017 and McCluskey2018 (Table 1), the parameter b for Helmos $S_{SMPS+APS}$ (**Error! Reference source not found.**) is adjusted to obtain a better prediction, which enables Helmos $S_{SMPS+APS}$ to predict more than 90% data points within a factor of 10 compared to observations (Figure 14). Helmos $S_{SMPS+APS}$ can also predict INPs from different aerosol sources with a f_{10} larger than 93% (Fig. S28), except INPs sourced from South dust in PBL after marine aerosols.

Summary of parameterizations and recommendations. All parameterizations presented in Figure 14 can predict >80% of the measured INP concentrations at Mt. Helmos within a factor of 10 of all observations of the corresponding dataset (see the caption). Comparing all parameterizations with the same sub-dataset in Figure 14, four newly proposed parameterizations, including Helmos Total$_{APS}$, Helmos Fluo$_{WIBS}$, Helmos Total$_{WIBS}$_1 and Helmos Total$_{WIBS}$_2, show f_3 and f_{10} predictions approximately 70% and 95% respectively. The superior performance of these four parameterizations is likely because the incorporation of aerosol particle ratios which implicitly are linked to specific particle types with distinct INP characteristics, hence leading to better predictions of IN activity of particles. Helmos Total$_{WIBS}$_2 has the smallest BIC value, suggesting it may have the highest overall optimality in terms of the model dimension and the maximum likelihood of the prediction (Schwarz, 1978). Notably, only Helmos Total$_{WIBS}$_1 can predict INPs from all different sources with a f_{10} prediction larger than 95%, which suggests its broad applicability for INPs from various sources. In addition, we further evaluate and compare parameterizations in Figure 14a to f by using them to predict a larger dataset than the sub-dataset used for their developments (Figs. S29 to S35 in supplement S12). The results suggest that Helmos Total$_{WIBS}$_1 outperforms the others by showing a f_{10} INP prediction larger than 95% for all aerosol sources (except INPs sourced from South dust in PBL after marine aerosols) also for the larger testing dataset (Fig. S34), and hence, it is the parameterization of choice for models that can constrain all the required input. Without including aerosol fluorescent properties, the results in both **Error! Reference source not found.**d (for Helmos DeMott2015) and Fig. **Error! Reference source not found.**d (Helmos Total$_{APS}$) suggest that INP parameterizations considering only APS data cannot predict INPs from continental aerosols at warm temperatures, which are likely of biological origin. If considering only the aerosol particle number concentration for INP prediction, Helmos Tobo2013FBAP outstands Helmos DeMott2015 and Helmos Total$_{SMPS+APS}$_1 (Fig. S22) in predicting more than 90% INPs from different sources, except showing a f_{10} of 0.5 for the dust case.

4 Summary and conclusions

Here we study the characteristics of different aerosol sources and their INP abundances in mixed-phased clouds at the high altitude Helmos Hellenic Atmospheric Aerosol and Climate Change station ((HAC)[2]) at Mount Helmos, Greece, during the Cloud-AerosoL InteractionS in the Helmos background TropOsphere (CALISTHO) campaign from a period between October

and November 2021. INPs were measured for $T > -27$ °C with online (PINE, in all IN mechanisms) and offline (INSEKT, in the immersion freezing mode) techniques. The relationship between INPs and different aerosol particle types was unravelled to understand the ice formation ability of particles from different aerosol sources. Specific INP source apportionment was carried out using a synergy of in-situ aerosol property characterization measurements, remote sensing and modelling experiments. The relative position of $(HAC)^2$ in the atmosphere with respect to planetary boundary layer (PBL) was determined by using both PBL height results from a pulsed Doppler scanning lidar system (HALO) and the number concentration of particles larger than 95 nm measured by a scanning mobility particle sizer (SMPS $N_{>95nm}$), so as to differentiate the airmass sampled from the PBL to free troposphere (FT). The presence of precipitation/clouds at $(HAC)^2$ was also monitored by a Wide-band Doppler spectral zenith profiler (WProf) radar by using equivalent radar reflectivity factor (Ze) and mean Doppler velocity (MDV). The size distribution (SMPS and APS, aerodynamic particle sizer), optical properties (nephelometer) and chemical composition (ToF-ACSM, time-of-flight aerosol chemical speciation monitor) of different aerosol particle populations were characterized when analysing the footprints and back trajectories of aerosol particles using FLEXPART and HYSPLIT results. Such a comprehensive synthesis study on INP source apportionment is not often reported in the literature. We conclude the following key findings:

- Specific and detailed INP source apportionment was achieved, demonstrated by the distinct characteristics of different sources, including continental, marine and dust aerosols, as well as a mixture of continental and dust aerosols. Fine particles (<1.0 μm) dominate continental aerosols and lead to an Ångström exponent (α) larger than 2.0 whereas coarse particles (>1.0 μm) take a substantial proportion in dust aerosols showing a fairly constant α of approximately 1.0. Marine aerosols show the highest content of Cl^-. The distinction of different aerosols is also indicated by their different particle portioning conditions, such as fine-to-coarse particle ratio and fluorescent-to-nonfluorescent particle ratio.

- In addition to PBLH and SMPS $N_{>95nm}$ used to diagnose the PBL condition of the observation site, we note that a threshold value of 20 std L^{-1} for $Coarse_{APS}$ particle concentration can be used as a more conservative standard to qualitatively examine the observation site condition with respect to the PBL. A higher (lower, compared to 20 std L^{-1}) value than the threshold indicates the observation site is inside (outside) the PBL. Under strictly defined FT conditions without influences of local and remote aerosols, i.e., background condition, only 1 in 10^6 of all aerosol particles acts as INPs for $T = -25 \pm 1.0$ °C. Additionally, we note that the INP abundance is also regulated by the property of relevant aerosol source and meteorological conditions, e.g., precipitation (Testa et al., 2021), in addition to temperatures and FT/PBL scenarios.

- Notably, the particle property and INP abundance of different aerosol sources also depend on the atmospheric condition, i.e., the relative position with respect to the PBL. Compared to the condition in the PBL, continental aerosols in the FT contain less particles. In particular, the decrease in coarse particles (>1.0 μm) for continental aerosols in the FT is more significant than that decrease in fine particles (<1.0 μm), which is responsible for its reduced INP abundance compared to the condition in the PBL. The INP abundance in North continental aerosols is

970 higher than that of background condition in the FT by more than one order of magnitude when the air mass is in the PBL. Marine aerosols above PBL show a similar INP abundance to that of North continental aerosols above PBL. Dust containing aerosols present the highest INP abundance among all sources. When dust is mixed with continental aerosol, the INP abundance decreases because of dilution, deposition and deactivation by atmospheric aging.

- The effects of precipitation/clouds lead to a slightly decrease in coarse-sized aerosol particles when the observation
975 site is in the FT, however, it results in a small increase in the INP abundance. Such an enrichment in INPs is attributed to the release of cloud-processed particles and/or near ground particle production caused by precipitation splash, both of which supply active INPs. On the other hand, the presence of precipitation/clouds results in decreased INP abundance when the observation site is in the PBL because of the wet removal of aerosol particles.

- The INP attribution results suggest that biological particles from the PBL air masses may be important INP sources
980 for continental and marine aerosols whereas coarse-sized dust particles play the primary role in the observed INPs in dust aerosols. The concentrations of INPs from marine and continental aerosols above the PBL are within a range of a factor of 5 compared to ABC_{WIBS} particles for more than 93% of the PINE observed INPs, suggesting that biological particles likely make an important contribution to the activated INPs. For dust-containing sources, biological particles may play a secondary role in the observed INPs after dust particles. We highlight that fluorescent particle
985 concentration recorded by WIBS (including biological particles and non-biological particles showing fluorescence) is able to describe all PINE observed INP concentration (for $T = -24 - -27$ °C) within a factor of 5 for more than 80% observed data points. Additionally, we note that mineral dust and carbonaceous particles may fluoresce because of some association with biological material or PAHs from combustion. Both eBC and dust particles can be transported by a long distance in the FT.

990 - The IN ability of different aerosol sources shows distinguishable characteristics and presents correlations with $Coarse_{APS}$ and fluorescent particle proportions. The above new findings were used to improve the predictability of INP parameterizations, which predict observed INPs for more than 90% data points for all identified INP sources and outperform existing INP parameterizations in the literature. The APS based INP parameterizations (Helmos $Total_{APS}$ in Table 3) show a less satisfactory INP predictability for warm temperatures (> −20 °C) compared to their
995 predictability for cold temperatures (< −20 °C), suggesting their inadequate capability of capturing biological INPs. Using particle fluorescence characteristics can improve INP parameterization predictability at warm temperatures. The parameterization developed from a sub-dataset (~80% of observations) was evaluated by predicting the whole observations with both WIBS and INP data. Considering biological particles that fluoresce and the proportion of those particles, our INP parameterization (Helmos $Total_{WIBS}\_1$ in Table 3) is able to predict the INP abundance in different
1000 sources within a factor of 10 for more than 95% data points, thus outperforms the existing parametrizations in the literature and the others proposed in this study.

- Existing INP parameterizations in the literature may be improved by including the ratio of fluorescent-to-nonfluorescent or coarse-to-fine particles if available. Firstly, regional models, like mesoscale Weather Research and

41

Forecasting (WRF) model, can use the improved INP parameterizations to calculate the ice formation processes for MPCs which ultimately helps to predict the local weather condition changes, such as storm formation and evolution (Georgakaki et al., 2024). Moreover, published dataset from existing field studies can be reorganized to a large and inclusive data base for the development of more general INP parameterizations for MPCs in global scales. In doing so, the predictability and applicability of the developed INP parameterizations for climate models can be improved. In particular, MPC simulations for regions with different INP sources, such as a cross-road of different air masses like (HAC)[2], or for different regions with different prevailing INP sources, such as continental or marine regions, can be better achieved. Ultimately, the regional and global simulations of aerosol-cloud interactions, as well as climate modelling, can be benefited from the improved INP parameterization.

The underestimation of INPs from INSEKT experiments, because of insufficient aerosol particle collection during aerosol sampling and/or filter washing, may partly influence the INP parameterizations. In this regard, INSEKT data, that are analysed as lower estimations by more than a factor of 5 compared to PINE INPs (Section 3.4.1 and Supplement S3), was filtered before using for parameterization. We note that underestimated INPs caused by insufficient sampling of aerosol particles for offline INP analysis may also result in lower estimation of aerosol-cloud interactions for warm temperatures in the MPC regime (e.g., $>-15°C$) which could carry important implications for inducing biases in the microphysical evolution of clouds in models. Therefore, the particle collection efficiency should be evaluated for existing INP data and INP parameterizations in the literature before using for climate models. Filter sampling (Conen et al., 2015; Schneider et al., 2021) and liquid impinger (Wieder et al., 2022) are commonly used in existing studies to collect INP samples for offline analysis. Standard sampling protocols for both methods are required to ensure sampling efficiency inter-comparison. For future studies, we suggest more flexible aerosol sampling strategies for offline INP measurements other than that used in this study (~1 day for INSEKT), like by employing automated filter samplers that allow sampling periods adjustable according to the changing aerosol particle concentrations, or by using wet cyclones to collect aerosol particles in liquids. The optimized sampling strategies for offline INP measurements should avoid filter over loading during dust events. To further test and validate the predictability of WIBS data based INP parametrizations, it necessitates a larger dataset that spans different seasons and based on observations at different sites in different regions. The further development of WIBS data based INP parameterizations will be addressed in our following work.

Competing interests. The authors declare that they have no conflict of interest.

Data availability. The data presented in this publication will be made available at https://www.envidat.ch. The DOI link will be activated for public access upon acceptance of publication.

References

Barahona, D. and Nenes, A.: Parameterizing the competition between homogeneous and heterogeneous freezing in ice cloud formation – polydisperse ice nuclei, Atmos. Chem. Phys., 9, 5933–5948, https://doi.org/10.5194/acp-9-5933-2009, 2009.

Barlow, J. F., Dunbar, T. M., Nemitz, E. G., Wood, C. R., Gallagher, M. W., Davies, F., O'Connor, E., and Harrison, R. M.: Boundary layer dynamics over London, UK, as observed using Doppler lidar during REPARTEE-II, Atmos. Chem. Phys., 11, 2111-2125, https://doi.org/10.5194/acp-11-2111-2011, 2011.

Bates, T. S., Kapustin, V. N., Quinn, P. K., Covert, D. S., Coffman, D. J., Mari, C., Durkee, P. A., De Bruyn, W. J., and Saltzman, E. S.: Processes controlling the distribution of aerosol particles in the lower marine boundary layer during the First Aerosol Characterization Experiment (ACE 1), J. Geophys. Res. Atmos., 103, 16369-16383, https://doi.org/10.1029/97jd03720, 1998.

Beall, C. M., Hill, T. C. J., DeMott, P. J., Köneman, T., Pikridas, M., Drewnick, F., Harder, H., Pöhlker, C., Lelieveld, J., Weber, B., Iakovides, M., Prokeš, R., Sciare, J., Andreae, M. O., Stokes, M. D., and Prather, K. A.: Ice-nucleating particles near two major dust source regions, Atmos. Chem. Phys., 22, 12607-12627, https://doi.org/10.5194/acp-22-12607-2022, 2022.

Bergeron, T.: On the physics of clouds and precipitation, In Proces Verbaux de l'Association de Météorologie, International Union of Geodesy and Geophysics, 156-178, 1935.

Billault-Roux, A.-C., Grazioli, J., Delanoë, J., Jorquera, S., Pauwels, N., Viltard, N., Martini, A., Mariage, V., Le Gac, C., Caudoux, C., Aubry, C., Bertrand, F., Schwarzenboeck, A., Jaffeux, L., Coutris, P., Febvre, G., Pichon, J. M., Dezitter, F., Gehring, J., Untersee, A., Calas, C., Figueras i Ventura, J., Vie, B., Peyrat, A., Curat, V., Rebouissoux, S., and Berne, A.: ICE

GENESIS: Synergetic Aircraft and Ground-Based Remote Sensing and In Situ Measurements of Snowfall Microphysical Properties, Bull. Am. Meteorol. Soc., 104, E367-E388, https://doi.org/10.1175/bams-d-21-0184.1, 2023.

Bjordal, J., Storelvmo, T., Alterskjær, K., and Carlsen, T.: Equilibrium climate sensitivity above 5 °C plausible due to state-dependent cloud feedback, Nat. Geosci., 13, 718-721, https://doi.org/10.1038/s41561-020-00649-1, 2020.

Bond, T. C., Doherty, S. J., Fahey, D. W., Forster, P. M., Berntsen, T., DeAngelo, B. J., Flanner, M. G., Ghan, S., Kärcher, B., Koch, D., Kinne, S., Kondo, Y., Quinn, P. K., Sarofim, M. C., Schultz, M. G., Schulz, M., Venkataraman, C., Zhang, H., Zhang, S., Bellouin, N., Guttikunda, S. K., Hopke, P. K., Jacobson, M. Z., Kaiser, J. W., Klimont, Z., Lohmann, U., Schwarz, J. P., Shindell, D., Storelvmo, T., Warren, S. G., and Zender, C. S.: Bounding the role of black carbon in the climate system: A scientific assessment, J. Geophys. Res. Atmos., 118, 5380-5552, https://doi.org/10.1002/jgrd.50171, 2013.

Boose, Y., Baloh, P., Plötze, M., Ofner, J., Grothe, H., Sierau, B., Lohmann, U., and Kanji, Z. A.: Heterogeneous ice nucleation on dust particles sourced from nine deserts worldwide – Part 2: Deposition nucleation and condensation freezing, Atmos. Chem. Phys., 19, 1059-1076, https://doi.org/10.5194/acp-19-1059-2019, 2019.

Brunner, C., Brem, B. T., Collaud Coen, M., Conen, F., Hervo, M., Henne, S., Steinbacher, M., Gysel-Beer, M., and Kanji, Z. A.: The contribution of Saharan dust to the ice-nucleating particle concentrations at the High Altitude Station Jungfraujoch (3580 m a.s.l.), Switzerland, Atmos. Chem. Phys., 21, 18029-18053, https://doi.org/10.5194/acp-21-18029-2021, 2021.

Burrows, S. M., McCluskey, C. S., Cornwell, G., Steinke, I., Zhang, K., Zhao, B., Zawadowicz, M., Raman, A., Kulkarni, G., China, S., Zelenyuk, A., and DeMott, P. J.: Ice-Nucleating Particles That Impact Clouds and Climate: Observational and Modeling Research Needs, Rev. Geophys., 60, https://doi.org/10.1029/2021rg000745, 2022.

Collaud Coen, M., Andrews, E., Aliaga, D., Andrade, M., Angelov, H., Bukowiecki, N., Ealo, M., Fialho, P., Flentje, H., Hallar, A. G., Hooda, R., Kalapov, I., Krejci, R., Lin, N.-H., Marinoni, A., Ming, J., Nguyen, N. A., Pandolfi, M., Pont, V., Ries, L., Rodríguez, S., Schauer, G., Sellegri, K., Sharma, S., Sun, J., Tunved, P., Velasquez, P., and Ruffieux, D.: Identification of topographic features influencing aerosol observations at high altitude stations, Atmos. Chem. Phys., 18, 12289-12313, https://doi.org/10.5194/acp-18-12289-2018, 2018.

Conen, F., Eckhardt, S., Gundersen, H., Stohl, A., and Yttri, K. E.: Rainfall drives atmospheric ice-nucleating particles in the coastal climate of southern Norway, Atmos. Chem. Phys., 17, 11065-11073, https://doi.org/10.5194/acp-17-11065-2017, 2017.

Conen, F., Morris, C. E., Leifeld, J., Yakutin, M. V., and Alewell, C.: Biological residues define the ice nucleation properties of soil dust, Atmos. Chem. Phys., 11, 9643-9648, https://10.5194/acp-11-9643-2011, 2011.

Conen, F., Rodríguez, S., Glin, C. H., Henne, S., Herrmann, E., Bukowiecki, N., and Alewell, C.: Atmospheric ice nuclei at the high-altitude observatory Jungfraujoch, Switzerland, Tellus B Chem. Phys. Meteorol., 67, https://doi.org/10.3402/tellusb.v67.25014, 2015.

Connolly, P. J., Mohler, O., Field, P. R., Saathoff, H., Burgess, R., Choularton, T., and Gallagher, M.: Studies of heterogeneous freezing by three different desert dust samples, Atmos. Chem. Phys., 9, 2805–2824, https://doi.org/10.5194/acp-9-2805-2009, 2009.

Crawford, I., Ruske, S., Topping, D. O., and Gallagher, M. W.: Evaluation of hierarchical agglomerative cluster analysis methods for discrimination of primary biological aerosol, Atmos. Meas. Tech., 8, 4979-4991, https://doi.org/10.5194/amt-8-4979-2015, 2015.

Crawford, I., Lloyd, G., Herrmann, E., Hoyle, C. R., Bower, K. N., Connolly, P. J., Flynn, M. J., Kaye, P. H., Choularton, T. W., and Gallagher, M. W.: Observations of fluorescent aerosol–cloud interactions in the free troposphere at the High-Altitude Research Station Jungfraujoch, Atmos. Chem. Phys., 16, 2273-2284, https://10.5194/acp-16-2273-2016, 2016.

D'Alessandro, J. J., Diao, M., Wu, C., Liu, X., Jensen, J. B., and Stephens, B. B.: Cloud Phase and Relative Humidity Distributions over the Southern Ocean in Austral Summer Based on In Situ Observations and CAM5 Simulations, J. Clim., 32, 2781-2805, https://doi.org/10.1175/jcli-d-18-0232.1, 2019.

DeMott, P. J.: Quantitative descriptions of ice formation mechanisms of silver iodide-type aerosols, Atmos. Res., 38, 63-99, https://doi.org/10.1016/0169-8095(94)00088-U, 1994.

DeMott, P. J., Prenni, A. J., Liu, X., Kreidenweis, S. M., Petters, M. D., Twohy, C. H., Richardson, M. S., Eidhammer, T., and Rogers, D. C.: Predicting global atmospheric ice nuclei distributions and their impacts on climate, Proc. Natl. Acad. Sci. U.S.A., 107, 11217-11222, https://doi.org/10.1073/pnas.0910818107, 2010.

DeMott, P. J., Prenni, A. J., McMeeking, G. R., Sullivan, R. C., Petters, M. D., Tobo, Y., Niemand, M., Möhler, O., Snider, J. R., Wang, Z., and Kreidenweis, S. M.: Integrating laboratory and field data to quantify the immersion freezing ice nucleation activity of mineral dust particles, Atmos. Chem. Phys., 15, 393-409, https://doi.org/10.5194/acp-15-393-2015, 2015.

Després, V. R., Huffman, J. A., Burrows, S. M., Hoose, C., Safatov, A. S., Buryak, G., Fröhlich-Nowoisky, J., Elbert, W., Andreae, M. O., Pöschl, U., and Jaenicke, R.: Primary biological aerosol particles in the atmosphere: a review, Tellus B Chem. Phys. Meteorol., 64, https://doi.org/10.3402/tellusb.v64i0.15598, 2012.

Draxler, R. R. and Hess, G. D.: An Overview of the HYSPLIT_4 Modelling System for Trajectories, Dispersion, and Deposition, Aust. Meteorol. Mag., 47, 295-308, 1998.

Fennelly, M., Sewell, G., Prentice, M., O'Connor, D., and Sodeau, J.: Review: The Use of Real-Time Fluorescence Instrumentation to Monitor Ambient Primary Biological Aerosol Particles (PBAP), Atmos., 9, https://doi.org/10.3390/atmos9010001, 2017.

Ferrone, A. and Berne, A.: Radar and ground-level measurements of clouds and precipitation collected during the POPE 2020 campaign at Princess Elisabeth Antarctica, Earth System Science Data, 15, 1115-1132, https://doi.org/10.5194/essd-15-1115-2023, 2023.

Field, P. R., Lawson, R. P., Brown, P. R. A., Lloyd, G., Westbrook, C., Moisseev, D., Miltenberger, A., Nenes, A., Blyth, A., Choularton, T., Connolly, P., Buehl, J., Crosier, J., Cui, Z., Dearden, C., DeMott, P., Flossmann, A., Heymsfield, A., Huang, Y., Kalesse, H., Kanji, Z. A., Korolev, A., Kirchgaessner, A., Lasher-Trapp, S., Leisner, T., McFarquhar, G., Phillips, V., Stith, J., and Sullivan, S.: Chapter 7. Secondary Ice Production - current state of the science and recommendations for the future, Meteorological Monographs, 58, 7.1–7.20, https://doi.org/10.1175/amsmonographs-d-16-0014.1, 2017.

Findeisen, W.: Die kolloidmeteorologischen Vorgänge bei der Niederschlagsbildung, Meteorologische Zeitschrift, 55, 121-133, 1938.

Findeisen, W., Volken, E., Giesche, A. M., and Brönnimann, S.: Colloidal meteorological processes in the formation of precipitation, Meteorologische Zeitschrift, 24, 443-454, https://doi.org/10.1127/metz/2015/0675, 2015.

1140   Foskinis, R., Gao, K., Gini, M. I., Diapouli, E., Vratolis, S., Granakis, K., Zografou, O., Kokkalis, P., Kommpula, M., Vakkari, V., Eleftheriadis, K., Nenes, A., and Papayannis, A.: The influence of the planetary boundary layer on the atmospheric state and cloud formation at an orographic site at the Eastern Mediterranean Tellus B Chem. Phys. Meteorol., 76, https://10.16993/tellusb.1876, 2024.

Gao, K., Koch, H.-C., Zhou, C.-W., and Kanji, Z. A.: The dependence of soot particle ice nucleation ability on its volatile
1145   content, Environmental Science: Processes & Impacts, 24, 2043-2069, https://doi.org/10.1039/D2EM00158F, 2022.

Garcia, E., Hill, T. C. J., Prenni, A. J., DeMott, P. J., Franc, G. D., and Kreidenweis, S. M.: Biogenic ice nuclei in boundary layer air over two U.S. High Plains agricultural regions, J. Geophys. Res. Atmos., 117, https://10.1029/2012jd018343, 2012.

Georgakaki, P., Sotiropoulou, G., Vignon, É., Billault-Roux, A.-C., Berne, A., and Nenes, A.: Secondary ice production processes in wintertime alpine mixed-phase clouds, Atmos. Chem. Phys., 22, 1965-1988, https://doi.org/10.5194/acp-22-1965-
1150   2022, 2022.

Georgakaki, P., Billault-Roux, A.-C., Foskinis, R., Gao, K., Sotiropoulou, G., Gini, M., Takahama, S., Eleftheriadis, K., Papayannis, A., Berne, A., and Nenes, A.: Unraveling secondary ice production in winter orographic clouds through a synergy of in-situ observations, remote sensing and modeling, npj Clim. Atmos. Sci., https://10.21203/rs.3.rs-3502790/v1, 2024.

Gini, M., Manousakas, M., Karydas, A. G., and Eleftheriadis, K.: Mass size distributions, composition and dose estimates of
1155   particulate matter in Saharan dust outbreaks, Environ. Pollut., 298, 118768, https://doi.org/10.1016/j.envpol.2021.118768, 2022.

Gong, X., Radenz, M., Wex, H., Seifert, P., Ataei, F., Henning, S., Baars, H., Barja, B., Ansmann, A., and Stratmann, F.: Significant continental source of ice-nucleating particles at the tip of Chile's southernmost Patagonia region, Atmos. Chem. Phys., 22, 10505-10525, https://10.5194/acp-22-10505-2022, 2022.

1160   Graber, E. R. and Rudich, Y.: Atmospheric HULIS: How humic-like are they? A comprehensive and critical review, Atmos. Chem. Phys., 6, 729-753, https://doi.org/10.5194/acp-6-729-2006, 2012.

Hagen, M. and Yuter, S. E.: Relations between radar reflectivity, liquid-water content, and rainfall rate during the MAP SOP, Q. J. R. Meteorol. Soc., 129, 477-493, https://doi.org/10.1256/qj.02.23, 2006.

Harrison, A. D., Whale, T. F., Carpenter, M. A., Holden, M. A., Neve, L., O'Sullivan, D., Vergara Temprado, J., and Murray,
1165   B. J.: Not all feldspars are equal: a survey of ice nucleating properties across the feldspar group of minerals, Atmos. Chem. Phys., 16, 10927-10940, https://10.5194/acp-16-10927-2016, 2016.

Henneberg, O., Lohmann, U., and Henneberger, J.: Formation and Development of Orographic Mixed-Phase Clouds, J. Atmos. Sci., 74, 3703-3724, https://doi.org/10.1175/jas-d-16-0348.1, 2017.

Hernandez, M., Perring, A. E., McCabe, K., Kok, G., Granger, G., and Baumgardner, D.: Chamber catalogues of optical and fluorescent signatures distinguish bioaerosol classes, Atmos. Meas. Tech., 9, 3283-3292, https://doi.org/10.5194/amt-9-3283-2016, 2016.

Herrmann, E., Weingartner, E., Henne, S., Vuilleumier, L., Bukowiecki, N., Steinbacher, M., Conen, F., Collaud Coen, M., Hammer, E., Jurányi, Z., Baltensperger, U., and Gysel, M.: Analysis of long-term aerosol size distribution data from Jungfraujoch with emphasis on free tropospheric conditions, cloud influence, and air mass transport, J. Geophys. Res. Atmos., 120, 9459-9480, https://doi.org/10.1002/2015jd023660, 2015.

Hill, T. C. J., DeMott, P. J., Tobo, Y., Fröhlich-Nowoisky, J., Moffett, B. F., Franc, G. D., and Kreidenweis, S. M.: Sources of organic ice nucleating particles in soils, Atmos. Chem. Phys., 16, 7195-7211, https://doi.org/10.5194/acp-16-7195-2016, 2016.

Hoose, C. and Möhler, O.: Heterogeneous Ice Nucleation on Atmospheric Aerosols: A Review of Results from Laboratory Experiments, Atmos. Chem. Phys., 12, 9817-9854, https://doi.org/10.5194/acp-12-9817-2012, 2012.

Isokääntä, S., Kim, P., Mikkonen, S., Kühn, T., Kokkola, H., Yli-Juuti, T., Heikkinen, L., Luoma, K., Petäjä, T., Kipling, Z., Partridge, D., and Virtanen, A.: The effect of clouds and precipitation on the aerosol concentrations and composition in a boreal forest environment, Atmos. Chem. Phys., 22, 11823-11843, https://doi.org/10.5194/acp-22-11823-2022, 2022.

Iwata, A., Imura, M., Hama, M., Maki, T., Tsuchiya, N., Kunihisa, R., and Matsuki, A.: Release of Highly Active Ice Nucleating Biological Particles Associated with Rain, Atmos., 10, https://doi.org/10.3390/atmos10100605, 2019.

Jahl, L. G., Brubaker, T. A., Polen, M. J., Jahn, L. G., Cain, K. P., Bowers, B. B., Fahy, W. D., Graves, S., and Sullivan, R. C.: Atmospheric aging enhances the ice nucleation ability of biomass-burning aerosol, Sci. Adv., 7, https://doi.org/10.1126/sciadv.abd3440, 2021.

Joung, Y. S., Ge, Z., and Buie, C. R.: Bioaerosol generation by raindrops on soil, Nat. Commun., 8, 14668, https://doi.org/10.1038/ncomms14668, 2017.

Kallos, G., Papadopoulos, A., Katsafados, P., and Nickovic, S.: Transatlantic Saharan dust transport: Model simulation and results, J. Geophys. Res. Atmos., 111, https://doi.org/10.1029/2005jd006207, 2006.

Kampe, H. J. a. and Weickmann, H. K.: The effectiveness of natural and artificial aerosols as freezing nuclei, J. Atmos. Sci., 8, 283-288, https://doi.org/10.1175/1520-0469(1951)008<0283:TEONAA>2.0.CO;2, 1951.

Kamra, A. K., Murugavel, P., and Pawar, S. D.: Measured size distributions of aerosols over the Indian Ocean during INDOEX, J. Geophys. Res. Atmos., 108, https://doi.org/10.1029/2002jd002200, 2003.

Kanji, Z. A., Ladino, L. A., Wex, H., Boose, Y., Burkert-Kohn, M., Cziczo, D. J., and Krämer, M.: Overview of ice nucleating particles, in: Meteorological Monographs, 1.1-1.33, https://doi.org/10.1175/amsmonographs-d-16-0006.1, 2017.

Kawana, K., Matsumoto, K., Taketani, F., Miyakawa, T., and Kanaya, Y.: Fluorescent biological aerosol particles over the central Pacific Ocean: covariation with ocean surface biological activity indicators, Atmos. Chem. Phys., 21, 15969-15983, https://doi.org/10.5194/acp-21-15969-2021, 2021.

Kaye, P. H., Stanley, W. R., and Hirst, E.: Single particle multichannel bio-aerosol fluorescence sensor, Opt. Express, 13, 3583-3593, https://doi.org/10.1364/OPEX.13.003583, 2005.

Kerminen, V.-M., Chen, X., Vakkari, V., Petäjä, T., Kulmala, M., and Bianchi, F.: Atmospheric new particle formation and growth: review of field observations, Environ. Res. Lett., 13, https://doi.org/10.1088/1748-9326/aadf3c, 2018.

Khadir, T., Riipinen, I., Talvinen, S., Heslin-Rees, D., Pöhlker, C., Rizzo, L., Machado, L. A. T., Franco, M. A., Kremper, L. A., Artaxo, P., Petäjä, T., Kulmala, M., Tunved, P., Ekman, A. M. L., Krejci, R., and Virtanen, A.: Sink, Source or Something In-Between? Net Effects of Precipitation on Aerosol Particle Populations, Geophys. Res. Lett., 50, https://doi.org/10.1029/2023GL104325, 2023.

Khan, B., Stenchikov, G., Weinzierl, B., Kalenderski, S., and Osipov, S.: Dust plume formation in the free troposphere and aerosol size distribution during the Saharan Mineral Dust Experiment in North Africa, Tellus B Chem. Phys. Meteorol., 67, https://doi.org/10.3402/tellusb.v67.27170, 2015.

Khlystov, A., Stanier, C., and Pandis, S. N.: An Algorithm for Combining Electrical Mobility and Aerodynamic Size Distributions Data when Measuring Ambient Aerosol Special Issue ofAerosol Science and Technologyon Findings from the Fine Particulate Matter Supersites Program, Aerosol Sci. Technol., 38, 229-238, https://doi.org/10.1080/02786820390229543, 2004.

Kim, Y. J., Boatman, J. F., Gunter, R. L., Wellman, D. L., and Wilkison, S. W.: Vertical distribution of atmospheric aerosol size distribution over south-central New Mexico, Atmos. Environ., 27, 1351-1362, https://doi.org/10.1016/0960-1686(93)90261-V, 1992.

Knopf, D. A. and Alpert, P. A.: Atmospheric ice nucleation, Nat. Rev. Phys., https://doi.org/10.1038/s42254-023-00570-7, 2023.

Kostrykin, S., Revokatova, A., Chernenkov, A., Ginzburg, V., Polumieva, P., and Zelenova, M.: Black Carbon Emissions from the Siberian Fires 2019: Modelling of the Atmospheric Transport and Possible Impact on the Radiation Balance in the Arctic Region, Atmos., 12, https://doi.org/10.3390/atmos12070814, 2021.

Küchler, N., Kneifel, S., Löhnert, U., Kollias, P., Czekala, H., and Rose, T.: A W-Band Radar–Radiometer System for Accurate and Continuous Monitoring of Clouds and Precipitation, J. Atmos. Ocean Technol., 34, 2375-2392, https://doi.org/10.1175/jtech-d-17-0019.1, 2017.

Lacher, L., Clemen, H.-C., Shen, X., Mertes, S., Gysel-Beer, M., Moallemi, A., Steinbacher, M., Henne, S., Saathoff, H., Möhler, O., Höhler, K., Schiebel, T., Weber, D., Schrod, J., Schneider, J., and Kanji, Z. A.: Sources and nature of ice-nucleating particles in the free troposphere at Jungfraujoch in winter 2017, Atmos. Chem. Phys., https://doi.org/10.5194/acp-21-16925-2021, 2021.

Laj, P., Bigi, A., Rose, C., Andrews, E., Lund Myhre, C., Collaud Coen, M., Lin, Y., Wiedensohler, A., Schulz, M., Ogren, J. A., Fiebig, M., Gliß, J., Mortier, A., Pandolfi, M., Petäja, T., Kim, S.-W., Aas, W., Putaud, J.-P., Mayol-Bracero, O., Keywood, M., Labrador, L., Aalto, P., Ahlberg, E., Alados Arboledas, L., Alastuey, A., Andrade, M., Artíñano, B., Ausmeel, S., Arsov, T., Asmi, E., Backman, J., Baltensperger, U., Bastian, S., Bath, O., Beukes, J. P., Brem, B. T., Bukowiecki, N., Conil, S.,

Couret, C., Day, D., Dayantolis, W., Degorska, A., Eleftheriadis, K., Fetfatzis, P., Favez, O., Flentje, H., Gini, M. I., Gregorič, A., Gysel-Beer, M., Hallar, A. G., Hand, J., Hoffer, A., Hueglin, C., Hooda, R. K., Hyvärinen, A., Kalapov, I., Kalivitis, N., Kasper-Giebl, A., Kim, J. E., Kouvarakis, G., Kranjc, I., Krejci, R., Kulmala, M., Labuschagne, C., Lee, H.-J., Lihavainen, H., Lin, N.-H., Löschau, G., Luoma, K., Marinoni, A., Martins Dos Santos, S., Meinhardt, F., Merkel, M., Metzger, J.-M.,

1240   Mihalopoulos, N., Nguyen, N. A., Ondracek, J., Pérez, N., Perrone, M. R., Petit, J.-E., Picard, D., Pichon, J.-M., Pont, V., Prats, N., Prenni, A., Reisen, F., Romano, S., Sellegri, K., Sharma, S., Schauer, G., Sheridan, P., Sherman, J. P., Schütze, M., Schwerin, A., Sohmer, R., Sorribas, M., Steinbacher, M., Sun, J., Titos, G., Toczko, B., Tuch, T., Tulet, P., Tunved, P., Vakkari, V., Velarde, F., Velasquez, P., Villani, P., Vratolis, S., Wang, S.-H., Weinhold, K., Weller, R., Yela, M., Yus-Diez, J., Zdimal, V., Zieger, P., and Zikova, N.: A global analysis of climate-relevant aerosol properties retrieved from the network of Global

1245   Atmosphere Watch (GAW) near-surface observatories, Atmos. Meas. Tech., 13, 4353-4392, https://doi.org/10.5194/amt-13-4353-2020, 2020.

Lohmann, U. and Neubauer, D.: The importance of mixed-phase and ice clouds for climate sensitivity in the global aerosol–climate model ECHAM6-HAM2, Atmos. Chem. Phys., 18, 8807-8828, https://doi.org/10.5194/acp-18-8807-2018, 2018.

Lohmann, U., Henneberger, J., Henneberg, O., Fugal, J. P., Bühl, J., and Kanji, Z. A.: Persistence of orographic mixed-phase

1250   clouds, Geophys. Res. Lett., 43, https://doi.org/10.1002/2016gl071036, 2016.

Longo, A. F., Ingall, E. D., Diaz, J. M., Oakes, M., King, L. E., Nenes, A., Mihalopoulos, N., Violaki, K., Avila, A., Benitez-Nelson, C. R., Brandes, J., McNulty, I., and Vine, D. J.: P-NEXFS analysis of aerosol phosphorus delivered to the Mediterranean Sea, Geophys. Res. Lett., 41, 4043-4049, https://doi.org/10.1002/2014gl060555, 2014.

Mason, R. H., Si, M., Li, J., Chou, C., Dickie, R., Toom-Sauntry, D., Pöhlker, C., Yakobi-Hancock, J. D., Ladino, L. A., Jones,

1255   K., Leaitch, W. R., Schiller, C. L., Abbatt, J. P. D., Huffman, J. A., and Bertram, A. K.: Ice nucleating particles at a coastal marine boundary layer site: correlations with aerosol type and meteorological conditions, Atmos. Chem. Phys., 15, 12547-12566, https://doi.org/10.5194/acp-15-12547-2015, 2015.

McCluskey, C. S., Ovadnevaite, J., Rinaldi, M., Atkinson, J., Belosi, F., Ceburnis, D., Marullo, S., Hill, T. C. J., Lohmann, U., Kanji, Z. A., O'Dowd, C., Kreidenweis, S. M., and DeMott, P. J.: Marine and Terrestrial Organic Ice-Nucleating Particles in

1260   Pristine Marine to Continentally Influenced Northeast Atlantic Air Masses, J. Geophys. Res. Atmos., 123, 6196-6212, https://doi.org/10.1029/2017jd028033, 2018.

Mignani, C., Wieder, J., Sprenger, M. A., Kanji, Z. A., Henneberger, J., Alewell, C., and Conen, F.: Towards parameterising atmospheric concentrations of ice-nucleating particles active at moderate supercooling, Atmos. Chem. Phys., 21, 657-664, https://doi.org/10.5194/acp-21-657-2021, 2021.

1265   Miltenberger, A. K., Field, P. R., Hill, A. H., and Heymsfield, A. J.: Vertical redistribution of moisture and aerosol in orographic mixed-phase clouds, Atmos. Chem. Phys., 20, 7979-8001, https://doi.org/10.5194/acp-20-7979-2020, 2020.

Moallemi, A., Landwehr, S., Robinson, C., Simo, R., Zamanillo, M., Chen, G., Baccarini, A., Schnaiter, M., Henning, S., Modini, R. L., Gysel-Beer, M., and Schmale, J.: Sources, Occurrence and Characteristics of Fluorescent Biological Aerosol

Particles Measured Over the Pristine Southern Ocean, J. Geophys. Res. Atmos., 126, e2021JD034811, https://doi.org/10.1029/2021JD034811, 2021.

Mohler, O., Stetzer, O., Schaefers, S., Linke, C., Schnaiter, M., Tiede, R., Saathoff, H., Kramer, M., Mangold, A., Budz, P., Zink, P., Schreiner, J., Mauersberger, K., Haag, W., Karcher, B., and Schurath, U.: Experimental Investigation of Homogeneous Freezing of Sulphuric Acid Particles in the Aerosol Chamber AIDA, Atmos. Chem. Phys., 3, 211-223, https://doi.org/10.5194/acp-3-211-2003, 2003.

Möhler, O., Adams, M., Lacher, L., Vogel, F., Nadolny, J., Ullrich, R., Boffo, C., Pfeuffer, T., Hobl, A., Weiß, M., Vepuri, H. S. K., Hiranuma, N., and Murray, B. J.: The Portable Ice Nucleation Experiment (PINE): A New Online Instrument for Laboratory Studies and Automated Long-Term Field Observations of Ice-Nucleating Particles, Atmos. Meas. Tech., 14, 1143-1166, https://doi.org/10.5194/amt-14-1143-2021, 2021.

Mordas, G., Prokopciuk, N., Byčenkienė, S., Andriejauskienė, J., and Ulevicius, V.: Optical Properties of the Urban Aerosol Particles Obtained from Ground Based Measurements and Satellite-Based Modelling Studies, Adv. Meteorol., 2015, 1-12, https://doi.org/10.1155/2015/898376, 2015.

Murray, B. J., O'Sullivan, D., Atkinson, J. D., and Webb, M. E.: Ice Nucleation by Particles Immersed in Supercooled Cloud Droplets, Chem. Soc. Rev., 41, 6519-6554, https://doi.org/10.1039/c2cs35200a, 2012.

Negron, A., DeLeon-Rodriguez, N., Waters, S. M., Ziemba, L. D., Anderson, B., Bergin, M., Konstantinidis, K. T., and Nenes, A.: Using flow cytometry and light-induced fluorescence to characterize the variability and characteristics of bioaerosols in springtime in Metro Atlanta, Georgia, Atmos. Chem. Phys., 20, 1817-1838, https://doi.org/10.5194/acp-20-1817-2020, 2020.

Niemand, M., Möhler, O., Vogel, B., Vogel, H., Hoose, C., Connolly, P., Klein, H., Bingemer, H., DeMott, P., Skrotzki, J., and Leisner, T.: A Particle-Surface-Area-Based Parameterization of Immersion Freezing on Desert Dust Particles, J. Atmos. Sci., 69, 3077-3092, https://doi.org/10.1175/jas-d-11-0249.1, 2012.

O'Sullivan, D., Murray, B. J., Malkin, T. L., Whale, T. F., Umo, N. S., Atkinson, J. D., Price, H. C., Baustian, K. J., Browse, J., and Webb, M. E.: Ice nucleation by fertile soil dusts: relative importance of mineral and biogenic components, Atmos. Chem. Phys., 14, 1853-1867, https://doi.org/10.5194/acp-14-1853-2014, 2014.

Pasquier, J. T., Henneberger, J., Ramelli, F., Lauber, A., David, R. O., Wieder, J., Carlsen, T., Gierens, R., Maturilli, M., and Lohmann, U.: Conditions favorable for secondary ice production in Arctic mixed-phase clouds, Atmos. Chem. Phys., 22, 15579-15601, https://doi.org/10.5194/acp-22-15579-2022, 2022.

Pereira Freitas, G., Adachi, K., Conen, F., Heslin-Rees, D., Krejci, R., Tobo, Y., Yttri, K. E., and Zieger, P.: Regionally sourced bioaerosols drive high-temperature ice nucleating particles in the Arctic, Nat. Commun., 14, 5997, https://doi.org/10.1038/s41467-023-41696-7, 2023.

Pereira, S., Wagner, F., and Silva, A. M.: Scattering properties and mass concentration of local and long-range transported aerosols over the South Western Iberia Peninsula, Atmos. Environ., 42, 7623-7631, https://doi.org/10.1016/j.atmosenv.2008.06.008, 2008.

Peter, J. R., Siems, S. T., Jensen, J. B., Gras, J. L., Ishizaka, Y., and Hacker, J. M.: Airborne observations of the effect of a cold front on the aerosol particle size distribution and new particle formation, Q. J. R. Meteorol. Soc., 136, 944-961, https://doi.org/10.1002/qj.515, 2010.

1305 Petters, M. D. and Wright, T. P.: Revisiting ice nucleation from precipitation samples, Geophys. Res. Lett., 42, 8758-8766, https://doi.org/10.1002/2015gl065733, 2015.

Pisso, I., Sollum, E., Grythe, H., Kristiansen, N. I., Cassiani, M., Eckhardt, S., Arnold, D., Morton, D., Thompson, R. L., Groot Zwaaftink, C. D., Evangeliou, N., Sodemann, H., Haimberger, L., Henne, S., Brunner, D., Burkhart, J. F., Fouilloux, A., Brioude, J., Philipp, A., Seibert, P., and Stohl, A.: The Lagrangian particle dispersion model FLEXPART version 10.4, Geosci.

1310 Model. Dev., 12, 4955-4997, https://doi.org/10.5194/gmd-12-4955-2019, 2019.

Pöhlker, C., Huffman, J. A., and Pöschl, U.: Autofluorescence of atmospheric bioaerosols – fluorescent biomolecules and potential interferences, Atmos. Meas. Tech., 5, 37-71, https://doi.org/10.5194/amt-5-37-2012, 2012.

Pousse-Nottelmann, S., Zubler, E. M., and Lohmann, U.: Microphysical processing of aerosol particles in orographic clouds, Atmos. Chem. Phys., 15, 9217-9236, https://doi.org/10.5194/acp-15-9217-2015, 2015.

1315 Prenni, A. J., Tobo, Y., Garcia, E., DeMott, P. J., Huffman, J. A., McCluskey, C. S., Kreidenweis, S. M., Prenni, J. E., Pöhlker, C., and Pöschl, U.: The impact of rain on ice nuclei populations at a forested site in Colorado, Geophys. Res. Lett., 40, 227-231, https://doi.org/10.1029/2012gl053953, 2013.

Pummer, B. G., Budke, C., Augustin-Bauditz, S., Niedermeier, D., Felgitsch, L., Kampf, C. J., Huber, R. G., Liedl, K. R., Loerting, T., Moschen, T., Schauperl, M., Tollinger, M., Morris, C. E., Wex, H., Grothe, H., Pöschl, U., Koop, T., and Fröhlich-

1320 Nowoisky, J.: Ice nucleation by water-soluble macromolecules, Atmos. Chem. Phys., 15, 4077-4091, https://doi.org/10.5194/acp-15-4077-2015, 2015.

Ran, L., Deng, Z., Wu, Y., Li, J., Bai, Z., Lu, Y., Zhuoga, D., and Bian, J.: Measurement report: Vertical profiling of particle size distributions over Lhasa, Tibet – tethered balloon-based in situ measurements and source apportionment, Atmos. Chem. Phys., 22, 6217-6229, https://doi.org/10.5194/acp-22-6217-2022, 2022.

1325 Reicher, N., Budke, C., Eickhoff, L., Raveh-Rubin, S., Kaplan-Ashiri, I., Koop, T., and Rudich, Y.: Size-dependent ice nucleation by airborne particles during dust events in the eastern Mediterranean, Atmos. Chem. Phys., 19, 11143-11158, https://doi.org/10.5194/acp-19-11143-2019, 2019.

Ristovski, Z. D., Wardoyo, A. Y. P., Morawska, L., Jamriska, M., Carr, S., and Johnson, G.: Biomass burning influenced particle characteristics in Northern Territory Australia based on airborne measurements, Atmos. Res., 96, 103-109,

1330 https://doi.org/10.1016/j.atmosres.2009.12.002, 2010.

Rogers, D. C., DeMott, P. J., Kreidenweis, S. M., and Chen, Y.: Measurements of ice nucleating aerosols during SUCCESS, Geophys. Res. Lett., 25, 1383-1386, https://doi.org/10.1029/97gl03478, 1998.

Savage, N. J., Krentz, C. E., Könemann, T., Han, T. T., Mainelis, G., Pöhlker, C., and Huffman, J. A.: Systematic characterization and fluorescence threshold strategies for the wideband integrated bioaerosol sensor (WIBS) using size-

1335   resolved biological and interfering particles, Atmos. Meas. Tech., 10, 4279-4302, https://doi.org/10.5194/amt-10-4279-2017, 2017.

Schiebel, T.: Ice Nucleation Activity of Soil Dust Aerosols, Karlsruhe Institute of Technology, Karlsruhe, Germany, 2017.

Schneider, J., Höhler, K., Heikkilä, P., Keskinen, J., Bertozzi, B., Bogert, P., Schorr, T., Umo, N. S., Vogel, F., Brasseur, Z., Wu, Y., Hakala, S., Duplissy, J., Moisseev, D., Kulmala, M., Adams, M. P., Murray, B. J., Korhonen, K., Hao, L., Thomson,

1340   E. S., Castarède, D., Leisner, T., Petäjä, T., and Möhler, O.: The seasonal cycle of ice-nucleating particles linked to the abundance of biogenic aerosol in boreal forests, Atmos. Chem. Phys., 21, 3899-3918, https://doi.org/10.5194/acp-21-3899-2021, 2021.

Schrod, J., Thomson, E. S., Weber, D., Kossmann, J., Pöhlker, C., Saturno, J., Ditas, F., Artaxo, P., Clouard, V., Saurel, J.-M., Ebert, M., Curtius, J., and Bingemer, H. G.: Long-term deposition and condensation ice-nucleating particle measurements

1345   from four stations across the globe, Atmos. Chem. Phys., 20, 15983-16006, https://doi.org/10.5194/acp-20-15983-2020, 2020.

Schroder, F. and Strom, J.: Aircraft measurements of sub micrometer aerosol particles (>7 nm) in the midlatitude free troposphere and tropopause region, Atmos. Res., 44, 333-356, https://doi.org/10.1016/S0169-8095(96)00034-8, 1997.

Schwarz, G.: Estimating the Dimension of a Model, The Annals of Statistics, 6, 461-461, https://doi.org/10.1214/aos/1176344136, 1978.

1350   Schween, J. H., Hirsikko, A., Löhnert, U., and Crewell, S.: Mixing-layer height retrieval with ceilometer and Doppler lidar: from case studies to long-term assessment, Atmos. Meas. Tech., 7, 3685-3704, https://doi.org/10.5194/amt-7-3685-2014, 2014.

Seinfeld, J. H., Bretherton, C., Carslaw, K. S., Coe, H., DeMott, P. J., Dunlea, E. J., Feingold, G., Ghan, S., Guenther, A. B., Kahn, R., Kraucunas, I., Kreidenweis, S. M., Molina, M. J., Nenes, A., Penner, J. E., Prather, K. A., Ramanathan, V.,

1355   Ramaswamy, V., Rasch, P. J., Ravishankara, A. R., Rosenfeld, D., Stephens, G., and Wood, R.: Improving our fundamental understanding of the role of aerosol-cloud interactions in the climate system, Proc. Natl. Acad. Sci. U.S.A., 113, 5781-5790, https://doi.org/10.1073/pnas.1514043113, 2016.

Spyrou, C., Mitsakou, C., Kallos, G., Louka, P., and Vlastou, G.: An improved limited area model for describing the dust cycle in the atmosphere, J. Geophys. Res., 115, https://doi.org/10.1029/2009jd013682, 2010.

1360   Stein, A. F., Draxler, R. R., Rolph, G. D., Stunder, B. J. B., Cohen, M. D., and Ngan, F.: NOAA's HYSPLIT Atmospheric Transport and Dispersion Modeling System, Bull. Am. Meteorol. Soc., 96, 2059-2077, https://doi.org/10.1175/bams-d-14-00110.1, 2015.

Stohl, A., Forster, C., Frank, A., Seibert, P., and Wotawa, G.: Technical note: The Lagrangian particle dispersion model FLEXPART version 6.2, Atmos. Chem. Phys., 5, 2461-2474, https://doi.org/10.5194/acp-5-2461-2005, 2005.

1365   Sullivan, S. C., Hoose, C., Kiselev, A., Leisner, T., and Nenes, A.: Initiation of secondary ice production in clouds, Atmos. Chem. Phys., 18, 1593-1610, https://doi.org/10.5194/acp-18-1593-2018, 2018.

Tan, I., Storelvmo, T., and Zelinka, M. D.: Observational constraints on mixed-phase clouds imply higher climate sensitivity, Science, 352, 224-227, https://doi.org.10.1126/science.aad5300, 2016.

Tang, D., Wei, T., Yuan, J., Xia, H., and Dou, X.: Observation of bioaerosol transport using wideband integrated bioaerosol sensor and coherent Doppler lidar, Atmos. Meas. Tech., 15, 2819-2838, https://doi.org/10.5194/amt-15-2819-2022, 2022a.

Tang, K., Sánchez-Parra, B., Yordanova, P., Wehking, J., Backes, A. T., Pickersgill, D. A., Maier, S., Sciare, J., Pöschl, U., Weber, B., and Fröhlich-Nowoisky, J.: Bioaerosols and atmospheric ice nuclei in a Mediterranean dryland: community changes related to rainfall, Biogeosciences, 19, 71-91, https://doi.org/10.5194/bg-19-71-2022, 2022b.

Tarn, M. D., Sikora, S. N. F., Porter, G. C. E., Wyld, B. V., Alayof, M., Reicher, N., Harrison, A. D., Rudich, Y., Shim, J. U., and Murray, B. J.: On-chip analysis of atmospheric ice-nucleating particles in continuous flow, Lab Chip, 20, 2889-2910, https://doi.org/10.1039/d0lc00251h, 2020.

Testa, B., Hill, T. C. J., Marsden, N. A., Barry, K. R., Hume, C. C., Bian, Q., Uetake, J., Hare, H., Perkins, R. J., Möhler, O., Kreidenweis, S. M., and DeMott, P. J.: Ice Nucleating Particle Connections to Regional Argentinian Land Surface Emissions and Weather During the Cloud, Aerosol, and Complex Terrain Interactions Experiment, J. Geophys. Res. Atmos., 126, https://doi.org/10.1029/2021jd035186, 2021.

Tobo, Y., DeMott, P. J., Hill, T. C. J., Prenni, A. J., Swoboda-Colberg, N. G., Franc, G. D., and Kreidenweis, S. M.: Organic matter matters for ice nuclei of agricultural soil origin, Atmos. Chem. Phys., 14, 8521-8531, https://doi.org/10.5194/acp-14-8521-2014, 2014.

Tobo, Y., Prenni, A. J., DeMott, P. J., Huffman, J. A., McCluskey, C. S., Tian, G., Pöhlker, C., Pöschl, U., and Kreidenweis, S. M.: Biological aerosol particles as a key determinant of ice nuclei populations in a forest ecosystem, J. Geophys. Res. Atmos., 118, 10,100-110,110, https://doi.org/10.1002/jgrd.50801, 2013.

Toprak, E. and Schnaiter, M.: Fluorescent biological aerosol particles measured with the Waveband Integrated Bioaerosol Sensor WIBS-4: laboratory tests combined with a one year field study, Atmos. Chem. Phys., 13, 225-243, https://doi.org/10.5194/acp-13-225-2013, 2013.

Ullrich, R., Hoose, C., Möhler, O., Niemand, M., Wagner, R., Höhler, K., Hiranuma, N., Saathoff, H., and Leisner, T.: A New Ice Nucleation Active Site Parameterization for Desert Dust and Soot, J. Atmos. Sci., 74, 699-717, https://doi.org/10.1175/jas-d-16-0074.1, 2017.

Umo, N. S., Murray, B. J., Baeza-Romero, M. T., Jones, J. M., Lea-Langton, A. R., Malkin, T. L., O'Sullivan, D., Neve, L., Plane, J. M. C., and Williams, A.: Ice nucleation by combustion ash particles at conditions relevant to mixed-phase clouds, Atmos. Chem. Phys., 15, 5195-5210, https://doi.org/10.5194/acp-15-5195-2015, 2015.

Vali, G.: Quantitative Evaluation of Experimental Results an the Heterogeneous Freezing Nucleation of Supercooled Liquids, J. Atmos. Sci., 28, 402-409, https://doi.org/10.1175/1520-0469(1971)028<0402:QEOERA>2.0.CO;2, 1971.

Vali, G.: Revisiting the differential freezing nucleus spectra derived from drop-freezing experiments: methods of calculation, applications, and confidence limits, Atmos. Meas. Tech., 12, 1219-1231, https://doi.org/10.5194/amt-12-1219-2019, 2019.

Vali, G., DeMott, P. J., Möhler, O., and Whale, T. F.: Technical Note: A Proposal for Ice Nucleation Terminology, Atmos. Chem. Phys., 15, 10263-10270, https://doi.org/10.5194/acp-15-10263-2015, 2015.

Violaki, K., Nenes, A., Tsagkaraki, M., Paglione, M., Jacquet, S., Sempéré, R., and Panagiotopoulos, C.: Bioaerosols and dust are the dominant sources of organic P in atmospheric particles, npj Clim. Atmos. Sci., 4, https://doi.org/10.1038/s41612-021-00215-5, 2021.

1405 Vratolis, S., Diapouli, E., Manousakas, M. I., Almeida, S. M., Beslic, I., Kertesz, Z., Samek, L., and Eleftheriadis, K.: A new method for the quantification of ambient particulate-matter emission fluxes, Atmos. Chem. Phys., 23, 6941-6961, https://doi.org/10.5194/acp-23-6941-2023, 2023.

Wegener, A.: Thermodynamik der atmosphäre, Nature, 90, 31, https://doi.org/10.1038/090031a0, 1912.

Wieder, J., Mignani, C., Schär, M., Roth, L., Sprenger, M., Henneberger, J., Lohmann, U., Brunner, C., and Kanji, Z. A.:
1410 Unveiling atmospheric transport and mixing mechanisms of ice-nucleating particles over the Alps, Atmos. Chem. Phys., 22, 3111-3130, https://doi.org/10.5194/acp-22-3111-2022, 2022.

Wilson, T. W., Ladino, L. A., Alpert, P. A., Breckels, M. N., Brooks, I. M., Browse, J., Burrows, S. M., Carslaw, K. S., Huffman, J. A., Judd, C., Kilthau, W. P., Mason, R. H., McFiggans, G., Miller, L. A., Najera, J. J., Polishchuk, E., Rae, S., Schiller, C. L., Si, M., Temprado, J. V., Whale, T. F., Wong, J. P., Wurl, O., Yakobi-Hancock, J. D., Abbatt, J. P., Aller, J. Y.,
1415 Bertram, A. K., Knopf, D. A., and Murray, B. J.: A marine biogenic source of atmospheric ice-nucleating particles, Nature, 525, 234-238, https://doi.org/10.1038/nature14986, 2015.

Xiao, H.-W., Xiao, H.-Y., Shen, C.-Y., Zhang, Z.-Y., and Long, A.-M.: Chemical Composition and Sources of Marine Aerosol over the Western North Pacific Ocean in Winter, Atmos., 9, https://doi.org/10.3390/atmos9080298, 2018.

Young, K. C.: A numerical simulation of wintertime, orographic precipitation: Part I. Description ofmodelmicrophysics and
1420 numerical techniques, J. Atmos. Sci., 31, 1735-1748, https://doi.org/10.1175/1520-0469(1974)031<1735:ANSOWO>2.0.CO;2, 1974.

Yue, S., Li, L., Xu, W., Zhao, J., Ren, H., Ji, D., Li, P., Zhang, Q., Wei, L., Xie, Q., Pan, X., Wang, Z., Sun, Y., and Fu, P.: Biological and Nonbiological Sources of Fluorescent Aerosol Particles in the Urban Atmosphere, Environ. Sci. Technol., 56, 7588-7597, https://doi.org/10.1021/acs.est.1c07966, 2022.

1425 Zaizen, Y., Okada, K., Ikegami, M., Sawa, Y., and Makino, Y.: Number-size Distributions of Aerosol Particles in the Free Troposphere over the Northwestern Pacific Ocean-Influence of Asian Outflow and Tropical Air Transport, Journal of the Meteorological Society of Japan, 82, 1147-1160, https://doi.org/10.2151/jmsj.2004.1147, 2004.

Zhang, X., Xu, X., Chen, H., Hu, X.-M., and Gao, L.: Dust-planetary boundary layer interactions amplified by entrainment and advections, Atmos. Res., 278, https://doi.org/10.1016/j.atmosres.2022.106359, 2022.

1430 Zhou, C., Liu, Y., and Wang, Q.: Calculating the Climatology and Anomalies of Surface Cloud Radiative Effect Using Cloud Property Histograms and Cloud Radiative Kernels, Adv. Atmos. Sci., 39, 2124-2136, https://doi.org/10.1007/s00376-021-1166-z, 2022.

Ziemba, L. D., Beyersdorf, A. J., Chen, G., Corr, C. A., Crumeyrolle, S. N., Diskin, G., Hudgins, C., Martin, R., Mikoviny, T., Moore, R., Shook, M., Thornhill, K. L., Winstead, E. L., Wisthaler, A., and Anderson, B. E.: Airborne observations of

1435   bioaerosol over the Southeast United States using a Wideband Integrated Bioaerosol Sensor, J. Geophys. Res. Atmos., 121, 8506-8524, https://doi.org/10.1002/2015jd024669, 2016.